

Master Thesis

Study of improving the stability and uniformity of the energy scale of the Super-Kamiokande detector with a calibration method using spallation neutron captures by gadolinium

(ガドリニウムによる核破碎中性子捕獲事象を用いた較正手法によるスーパーカミオカンデ検出器のエネルギースケールの安定性及び一様性向上の研究)

2025

Department of Physics, Graduate School of Science The University of  
Tokyo

(東京大学大学院理学系研究科物理学専攻)

Tomoki Muro  
室 朝喜

## Abstract

In the Super-Kamiokande experiment, gadolinium (Gd) was introduced to improve neutron capture efficiency, with a Gd concentration of 0.01 % in 2020 - 2022 (the SK-VI phase) and 0.03 % after 2022 (the SK-VII and SK-VIII phases). To achieve a systematic uncertainty of 0.5 % for precise solar neutrino measurements in these phases, a new calibration method was developed using spallation neutron captures on Gd. This approach enables detailed monitoring of the detector's energy scale position dependence and time stability due to the high event rate (about 100,000/day) and uniform distribution of events throughout the detector.

The position dependence of the energy scale was evaluated in both the radial ( $r^2$ ) and vertical ( $z$ ) directions. Using this method, we found that the  $z$ -dependence was about 0.49 %, and the  $r^2$ -dependence was about 0.88 %. While the  $z$ -dependence met the goal, the  $r^2$ -dependence exceeded it. Time stability of the energy scale, excluding Gd-loading periods, was about 0.35 % and 0.38 % for SK-VI and SK-VII, meeting the goal. However, the absolute energy scales of these two phases differed by about 1.9 %. These results revealed the current accuracy of the energy reconstruction in the Gd-loaded Super-Kamiokande and highlighted that the area needs further improvements. It also provided calibration points to understand water transparency variation better.

# Contents

<b>1</b>	<b>Physics motivation</b>	<b>1</b>
1.1	Neutrino . . . . .	1
1.1.1	Neutrino oscillation . . . . .	1
1.2	Solar neutrino . . . . .	5
1.2.1	Solar neutrino production . . . . .	5
1.2.2	Solar neutrino problem . . . . .	7
1.2.3	MSW effect of solar neutrino . . . . .	8
1.2.4	Up-turn effect of solar neutrino . . . . .	11
1.2.5	Day/night effect of solar neutrino . . . . .	11
1.2.6	Oscillation parameter determination with solar neutrinos . . . . .	12
1.3	Diffuse Supernova Neutrino Background (DSNB) . . . . .	13
1.3.1	Supernova explosion . . . . .	13
1.3.2	Supernova neutrino . . . . .	14
1.3.3	Diffuse Supernova Neutrino Background (DSNB) . . . . .	16
<b>2</b>	<b>Super-Kamiokande experiment</b>	<b>18</b>
2.1	Super-Kamiokande detector . . . . .	18
2.1.1	Inner detector . . . . .	18
2.1.2	Outer detector . . . . .	22
2.1.3	Geomagnetic field compensation coil . . . . .	22
2.1.4	Data acquisition phase of Super-Kamiokande . . . . .	23
2.2	Principle of detection . . . . .	25
2.2.1	Cherenkov light . . . . .	25
2.3	Data acquisition system . . . . .	27
2.3.1	QTC Based Electronics with Ethernet (QBEE) . . . . .	27
2.3.2	DAQ . . . . .	29
2.3.3	Software trigger . . . . .	29
2.4	Super-Kamiokande with gadolinium . . . . .	30
2.4.1	Gadolinium . . . . .	30
2.4.2	Ultrapure water purification system . . . . .	30
2.4.3	Radon-free air production system . . . . .	33
2.4.4	Gadolinium sulfate solution system . . . . .	34
<b>3</b>	<b>Energy calibration and reconstruction</b>	<b>38</b>
3.1	Inner detector related calibration . . . . .	38
3.1.1	Measurement of relative gain . . . . .	38

3.1.2	Measurement of absolute gain . . . . .	39
3.1.3	Measurement of relative quantum efficiency . . . . .	41
3.1.4	Measurement of hit collection efficiency . . . . .	41
3.1.5	Calibration of time response . . . . .	42
3.2	Water related calibration . . . . .	44
3.2.1	Measurement of the water transparency with a laser . . . . .	44
3.2.2	Measurement of water transparency with decay electrons . . . . .	47
3.2.3	Top-bottom asymmetry . . . . .	49
3.3	Event reconstruction . . . . .	50
3.3.1	Vertex reconstruction . . . . .	50
3.3.2	Direction reconstruction . . . . .	52
3.3.3	Effective hits of the PMT $N_{\text{eff}}$ . . . . .	53
3.3.4	Energy reconstruction . . . . .	55
3.4	Energy calibration . . . . .	56
3.4.1	LINAC . . . . .	56
3.4.2	DT . . . . .	58
3.5	Energy scale monitoring . . . . .	60
3.5.1	$^{16}\text{N}$ analysis . . . . .	62
3.5.2	Decay electron analysis . . . . .	62
<b>4</b>	<b>Spallation neutron capture on gadolinium</b>	<b>65</b>
4.1	Spallation neutron by cosmic ray muon . . . . .	65
4.1.1	Muon generation by cosmic ray . . . . .	65
4.1.2	Spallation neutron by cosmic ray muons . . . . .	66
4.2	Spallation neutron captures on gadolinium . . . . .	68
4.2.1	Feature of spallation neutron capture events . . . . .	68
4.2.2	Advantages and disadvantages of calibration using spallation neutron capture events . . . . .	68
4.3	Event selection of spallation neutron capture events . . . . .	69
4.3.1	Cosmic ray muon selection . . . . .	69
4.3.2	Spallation neutron capture events selection . . . . .	71
4.3.3	Summary of event selection . . . . .	80
4.4	Evaluation of mean $N_{\text{eff}}$ and energy . . . . .	80
<b>5</b>	<b>Monte Carlo simulation</b>	<b>82</b>
5.1	Software for Monte Carlo simulation . . . . .	82
5.2	Production of the simulated events . . . . .	82
5.3	Event selection for MC . . . . .	83
5.3.1	Event selection conditions . . . . .	83
5.3.2	Summary of event selection . . . . .	85
<b>6</b>	<b>Energy scale calibration with spallation neutron capture signal</b>	<b>86</b>
6.1	Evaluation of position dependence of the SK detector . . . . .	86
6.1.1	Position dependence of energy in SK-VI and SK-VII periods . . . . .	87
6.1.2	Comparison of the neutron and electron simulation . . . . .	90
6.2	Difference of tuning sources in the Monte Carlo simulation . . . . .	95
6.3	Evaluation of time dependence of the SK detector . . . . .	95

6.3.1	Time variation of energy in SK-VI and SK-VII periods . . . . .	97
<b>7</b>	<b>Discussion</b>	<b>100</b>
<b>8</b>	<b>Conclusion</b>	<b>102</b>
<b>A</b>	<b>Ratio of the neutron captures on Hydrogen</b>	<b>105</b>

# List of Figures

1.1	Energy spectrum of the solar neutrino . . . . .	7
1.2	The measurement result in SNO experiment [30]. The red belt is 68 % C.L. of $\phi_{CC}$ , the blue belt is that of $\phi_{NC}$ , the green belt is that of $\phi_{ES}$ , and the ellipses drawn with dotted lines are 68 %, 95 %, and 99 % C.L. from the inside. The belt between two dotted line is the 68 % C.L. of the SSM predicted value $\phi_{SSM}$ . . . . .	8
1.3	weak interaction of neutrinos . . . . .	9
1.4	Electron density dependence of neutrino masses in the sun [32]. The vertical axis represents neutrino mass squared, the horizontal axis represents electron density. . . . .	11
1.5	The electron neutrino survival probability as a function of neutrino energy and solar neutrino measurements [33]. The red area is theoretically predicted using the SK+SNO spectrum data. . . . .	12
1.6	The allowable range of $\theta_{12}$ and $\Delta m_{21}^2$ which were measured by solar neutrino measurement and reactor neutrino measurement in KamLAND [33]. The blue area represents the result of solar neutrino measurement, and the green one represents the result of reactor measurement in KamLAND. The red area represents the combined result. . . . .	13
1.7	Time distribution of supernova neutrino energy and luminosity [34]. . . . .	16
1.8	DSNB $\bar{\nu}_e$ flux prediction from various theoretical models [35] . . . . .	17
2.1	The overview of the detector [37] . . . . .	19
2.2	The cross-section of SK detector [36]. . . . .	19
2.3	The super module [36]. . . . .	20
2.4	Schematic view of Hamamatsu R3600 [36]. . . . .	21
2.5	The wavelength dependence of quantum efficiency of the PMT [36]. . . . .	21
2.6	The coordinate of the SK detector. . . . .	22
2.7	The positional relationship between the ID PMTs and the OD PMTs [38].	23
2.8	The overview of the compensation coil [40]. . . . .	23
2.9	Outline drawing of Cherenkov light . . . . .	26
2.10	QBEE system [42]. . . . .	27
2.11	The timing chart inside the QTC [42]. . . . .	28
2.12	The diagram of the DAQ [43]. . . . .	29
2.13	The fraction of thermal neutrons captured by gadolinium. . . . .	31
2.14	The overview of the ultrapure water purification system [41]. . . . .	32
2.15	The schematic drawing of the radon-free air dissolving system [36]. . . . .	34
2.16	Schematic diagram of SK-Gd water system [45]. . . . .	37

3.1	The distribution of the relative gain of each PMT (left) and projection onto the vertical axis for all data sets (right) in SK-V. In the right figure, each colored line represents the measurement period. . . . .	39
3.2	The diagram of Ni-Cf source and the emission of $\gamma$ ray. . . . .	40
3.3	The charge distribution using Ni-Cf source in SK-III [39]. . . . .	41
3.4	The distribution of relative QE [46]. Each colored histogram represents the year of manufacture of each PMT as in the figure. . . . .	42
3.5	The relative CE of each PMT [47]. . . . .	43
3.6	The diagram of TQ calibration (left) and the cross-section of the diffuser ball (right) [39]. . . . .	43
3.7	The relationship between the charge and hit time in one PMT [39]. . . . .	44
3.8	The scattering effect [57]. . . . .	45
3.9	The diagram of the measurement of the water transparency [39]. The PMTs are divided into 6 areas, the top of the detector, B1, B2, B3, B4, and B5. . . . .	46
3.10	The hit time distribution of data and MC using the 405 nm wavelength laser [39]. From the top, each histogram represents the top of the tank, B1, B2, B3, B4, and B5 in Figure 3.9. The black line represents the data and the red line represents the MC. . . . .	46
3.11	The charge vs distance $r$ plot. . . . .	48
3.12	The time variation of the water transparency. . . . .	48
3.13	The correlation plot between $C_{\text{abs}}$ and the $\text{WT}_{\text{decay-e}}$ . . . . .	49
3.14	Top: The time variation of the top-bottom asymmetry (TBA) throughout SK-IV. [36]. The red dots represent the Xe light source data and the blue dots represent the Ni-Cf source data. Bottom: The difference between two TBA measurements. . . . .	50
3.15	The probability density function of $t_{\text{res},i}$ [46]. The second and third peaks around 40 ns and 110 ns are due to the after pulse of PMT. . . . .	51
3.16	The energy dependence of the vertex resolution in SK-IV [36]. . . . .	51
3.17	The definition of the incident angle of the photon on the PMT [48]. . . . .	52
3.18	The diagram of the estimated number of photons. . . . .	53
3.19	The definition of the incident angle of the photon. . . . .	54
3.20	The correction function $S(\theta, \phi)$ which corrects the coverage area of photocathode of the PMT. The left one is for the barrel PMTs and the right one is for the top and bottom PMTs. . . . .	54
3.21	The relation between $C_{\text{sca}}$ and the position dependence of $N_{\text{eff}}$ . . . . .	55
3.22	The $E(N_{\text{eff}})$ function and the values from $p_0$ to $p_6$ in SK-VI. Black dots show MC simulation results and blue line represents the function derived by fitting. "G4" written in the figure is the name of the simulation package. . . . .	56
3.23	The schematic diagram of LINAC. The points from A to I represent the injection position of electrons [49]. . . . .	57
3.24	The $N_{\text{eff}}$ difference of the LINAC data and MC in SK-IV [33]. Each marker represents each injection position. The red dot lines represent $\pm 0.5$ % difference. . . . .	59
3.25	The schematic diagram of the DT measurement [50]. . . . .	60

3.26	The position dependence (left) and directional dependence (right) of $N_{\text{eff}}$ from DT calibration data in SK-IV [33]. . . . .	61
3.27	The time variation of $N_{\text{eff}}$ from DT calibration data in SK-IV [33]. . . . .	61
3.28	Energy scale evaluation of $^{16}\text{N}$ and DT calibration [51]. The black dots represent the $^{16}\text{N}$ data and the red dots represent the DT data. . . . .	62
3.29	The position dependence of $^{16}\text{N}$ and DT calibration [51]. The left one is the $z$ -dependence and the right one is the $r^2$ -dependence. The black dots represent the $^{16}\text{N}$ data and the red dots represent the DT data. . . . .	63
3.30	The directional dependence of $^{16}\text{N}$ and DT calibration [51]. The left one is zenith angle $\cos\theta$ dependence and the right one is azimuth $\phi$ dependence. The black dots represent the $^{16}\text{N}$ data and the red dots represent the DT data. . . . .	63
3.31	The energy spectrum of the reconstructed decay electrons [52]. . . . .	63
4.1	Production of cosmic ray muon above the SK detector. . . . .	66
4.2	Spallation by a muon. . . . .	66
4.3	Comparison of the calibration with spallation neutron captures on gadolinium with other energy calibration methods. . . . .	69
4.4	The $Q_\mu$ distribution. $Q_\mu$ is the total integrated charge detected by the ID PMTs in the SHE trigger. The red line indicates the position of $Q_\mu \approx 10,000$ p.e. The events to the right of the red line are selected. . . . .	70
4.5	The diagram of SHE and AFT triggers and sub-events. When cosmic ray muon enters the SK detector, that time is set to 0 and SHE and AFT triggers are issued. Signals that exceed the sub-trigger ( $N_{200} = 20$ ) are stored as sub-events with $1.3 \mu\text{s}$ time window. . . . .	70
4.6	The schematic diagram of the $dt$ distribution of the spallation neutron capture on gadolinium. . . . .	71
4.7	The $dt$ distribution of the spallation neutron captures on gadolinium in SK-VI and SK-VII period. . . . .	72
4.8	(a) The $g_{\text{vtx}}$ distribution in the signal region and background region. The blue line represents the signal region ( $[35, 235] \mu\text{s}$ ) and the red line represents the background region ( $[335, 535] \mu\text{s}$ ). (b) The $g_{\text{vtx}}$ distribution of subtracting the background region from the signal region. The right side of the red line ( $g_{\text{vtx}} > 0.4$ ) is selected. . . . .	73
4.9	(a) The $g_{\text{dir}}$ distribution in the signal region and background region. The blue line represents the signal region ( $[35, 235] \mu\text{s}$ ) and the red line represents the background region ( $[335, 535] \mu\text{s}$ ). (b) The $g_{\text{dir}}$ distribution of subtracting the background region from the signal region. The left side of the red line ( $g_{\text{dir}} < 0.4$ ) is selected. . . . .	73
4.10	Distance between muon track and reconstructed point of neutron capture event. . . . .	74
4.11	(a) The $L_t$ distribution in the signal region and background region. The blue line represents the signal region ( $[35, 235] \mu\text{s}$ ) and the red line represents the background region ( $[335, 535] \mu\text{s}$ ). (b) The $L_t$ distribution of subtracting the background region from the signal region. The left side of the red line ( $L_t < 300$ cm) is selected. . . . .	74

4.12	(a) The reconstructed time $t_0$ distribution in the signal region and background region. The blue line represents the signal region ( $[35, 235] \mu\text{s}$ ) and the red line represents the background region ( $[335, 535] \mu\text{s}$ ). (b) The $t_0$ distribution of subtracting the background region from the signal region. The region between the red lines ( $[0.7, 1.0] \mu\text{s}$ ) is selected. . . . .	75
4.13	The $N_{50}$ distribution using the fiducial volume cut, reconstruction quality cut, $L_t$ cut, reconstructed time cut, and background signal reduction. . . .	76
4.14	The distribution of the number of spallation neutrons produced by one cosmic ray muon. . . . .	76
4.15	(a) The $N_{50}$ distribution for 1 neutron multiplicity in the signal region ( $[35, 235] \mu\text{s}$ ) and the background region ( $[335, 535] \mu\text{s}$ ). The blue line represents the signal region and the red line represents the background region. (b) The $N_{50}$ distribution for 1 neutron multiplicity. This distribution is obtained by subtracting the background region from the signal region. The red curve represents the result of the third fitting and the red line represents the mean $N_{50}$ . The mean $N_{50}$ for 1 neutron is $29.74 \pm 0.02$ . . . . .	77
4.16	The pile-up effect of the neutron multiplicity. The horizontal axis represents the neutron multiplicity. The vertical axis represents the mean $N_{50}$ for each neutron multiplicity. . . . .	78
4.17	The illustration of the selection of the sub-events. In the sub-trigger time window ( $1.3 \mu\text{s}$ ), the largest signal is selected as the sub-event. The yellow lines represent the PMT hits. . . . .	78
4.18	The deviation of the pile-up effect. The black line represents $\pm 0.5\%$ . . . .	79
4.19	(a) The $N_{\text{eff}}$ distribution of spallation neutron captures on Gd in the signal region ( $[35, 235] \mu\text{s}$ ) and the background region ( $[335, 535] \mu\text{s}$ ). The blue line represents the signal region and the red line represents the background region. The event selections are applied to the data. (b) The $N_{\text{eff}}$ distribution of spallation neutron captures on Gd. This distribution is obtained by subtracting the background region from the signal region. The red curve represents the final Gaussian fit and the mean value of this fit is used as the mean $N_{\text{eff}}$ . . . . .	81
4.20	(a) The energy distribution of spallation neutron captures on Gd in the signal region ( $[35, 235] \mu\text{s}$ ) and the background region ( $[335, 535] \mu\text{s}$ ). The blue line represents the signal region and the red line represents the background region. The event selections are applied to the data. (b) The energy distribution of spallation neutron captures on Gd. This distribution is obtained by subtracting the background region from the signal region. The red curve represents the final Gaussian fit and the mean value of this fit is used as the mean energy. . . . .	81
5.1	The distribution of produced neutrons. . . . .	83
5.2	The dt distribution of neutron capture events in SK-VI and SK-VII period. . . . .	84

5.3	(a) The $g_{vtx}$ distribution in the signal region and background region. The blue line represents the signal region ( $[35, 235] \mu s$ ) and the red line represents the background region ( $[335, 535] \mu s$ ). (b) The $g_{vtx}$ distribution of subtracting the background region from the signal region. The right side of the red line ( $g_{vtx} > 0.4$ ) is selected. . . . .	84
5.4	(a) The $g_{dir}$ distribution in the signal region and background region. The blue line represents the signal region ( $[35, 235] \mu s$ ) and the red line represents the background region ( $[335, 535] \mu s$ ). (b) The $g_{dir}$ distribution of subtracting the background region from the signal region. The left side of the red line ( $g_{dir} < 0.4$ ) is selected. . . . .	84
5.5	(a) The $t_0$ distribution in the signal region and background region. The blue line represents the signal region ( $[35, 235] \mu s$ ) and the red line represents the background region ( $[335, 535] \mu s$ ). (b) The $t_0$ distribution of subtracting the background region from the signal region. The area between the red lines ( $0.7 < t_0 < 1.0$ ) is selected. . . . .	85
6.1	The detector is divided into five regions in the $r^2$ -direction (left) and in the z-direction (right). . . . .	87
6.2	The energy distributions and the Gaussian fitting results for SK-VII. The left figure represents the $r^2$ -direction division areas. The right one represents the z-direction division areas. The red curves represent the fitting results. . . . .	87
6.3	The mean energies of the data and MC for SK-VI and SK-VII. The blue dots represent SK-VI and the red dots represent SK-VII. The circle dots represent the real data and the triangle dots represent the MC. . . . .	88
6.4	The $\text{diff}_{\text{pos}}$ of the data and MC for SK-VI. The blue dots represent the data and the red dots represent the MC. . . . .	89
6.5	The $\text{diff}_{\text{pos}}$ of the data and MC for SK-VII. The blue dots represent the data and the red dots represent the MC. . . . .	89
6.6	The position dependence in the $r^2$ -direction and the z-direction for SK-VI and SK-VII. The red dots represent the SK-VI result and the blue dots represent the SK-VII result. . . . .	90
6.7	The mean energy in each area for the SK-VI and SK-VII electron MC. The blue dots represent SK-VI and the red dots represent SK-VII. . . . .	91
6.8	The $\text{diff}_{\text{pos}}$ of the mean energy for the SK-VI electron and neutron MC. The blue dots represent the electron MC and the red dots represent the neutron MC. . . . .	91
6.9	The $\text{diff}_{\text{pos}}$ of the mean energy for the SK-VII electron and neutron MC. The blue dots represent the electron MC and the red dots represent the neutron MC. . . . .	92
6.10	The subtraction from the $\text{diff}_{\text{pos}}$ of the neutron MC from that of the electron MC. The blue dots represent the SK-VI MC, and the red dots represent the SK-VII MC. . . . .	92
6.11	The $\text{diff}_{\text{pos}}$ of each electron energy for the SK-VI electron MC. . . . .	93
6.12	The $\text{diff}_{\text{pos}}$ of each electron energy for the SK-VII electron MC. . . . .	94

6.13	The relationship between the deviation and the electron energy for the SK-VI and SK-VII MC. The blue dots represent the SK-VI MC and the red dots represent the SK-VII MC. . . . .	94
6.14	The energy spectrum of the gamma ray from neutron captures on gadolinium [59]. . . . .	94
6.15	The mean $N_{\text{eff}}$ using the different tuning source parameters. The red dots represent the mean $N_{\text{eff}}$ using the decay electrons tuning parameters, and the blue dots represent that using the 50 MeV electrons tuning parameters. The green dots represent the mean $N_{\text{eff}}$ of the SK-VII MC. . . . .	96
6.16	(a) Area division. (b) The reconstructed energy distribution in each area. . . . .	96
6.17	The time distribution of the mean energy for SK-VI data. . . . .	97
6.18	The $\text{diff}_{\text{period}}$ of the mean energy for SK-VI data. . . . .	97
6.19	The time distribution of the mean energy for SK-VII data. . . . .	98
6.20	The $\text{diff}_{\text{period}}$ of the mean energy for SK-VII data. . . . .	98
A.1	The $N_{\text{eff}}$ distribution for the SK-VI MC. The black line represents the signals from neutron captures on hydrogen. The red line represents those from neutron captures on gadolinium. The green line represents other signals. The blue line represents the sum of all signals. . . . .	105
A.2	The $N_{\text{eff}}$ distribution for the SK-VII MC. The black line represents the signals from neutron captures on hydrogen. The red line represents those from neutron captures on gadolinium. The green line represents other signals. The blue line represents the sum of all signals. . . . .	106

# List of Tables

1.1	Neutrino oscillation parameters [17]. NO is normal mass ordering and IO is inverted mass ordering. . . . .	5
2.1	Typical performance of the ID PMTs [36]. . . . .	21
2.2	The detector performance per data acquisition period. . . . .	25
2.3	The summary of Cherenkov threshold in water. . . . .	26
2.4	The gain channels of QTC and the dynamic ranges and charge resolution of each channel [42]. . . . .	28
2.5	The summary of the software triggers. . . . .	30
2.6	The natural abundance ratio and the thermal neutron capture cross-sections [45]. . . . .	31
3.1	The value of the absolute gain in each SK phase [39]. . . . .	40
3.2	The summary of the parameters $P_0$ to $P_8$ for SK-VI and SK-VII . . . . .	47
3.3	The coordinates of the injection position of the LINAC electron beam. . . . .	57
3.4	The value of COREPMT for each MC package and measurement phase. . . . .	58
4.1	Predicted radioisotopes by oxygen nucleus spallation with cosmic ray muons in the SK detector. The fourth column shows the maximum kinetic energy of the emitted electron or positron. The fifth column shows an expected yield of the radioisotope [53,54]. . . . .	67
4.2	Number of fit and fit range. . . . .	77
4.3	The summary of the event selections for spallation neutron captures on gadolinium. $L_t$ is the distance between a muon track and a reconstructed event point. $t_0$ is the reconstructed time. n is the neutron multiplicity. . . . .	80
4.4	Number of fit and fit range. . . . .	80
5.1	The summary of the event selections for MC. $t_0$ is the reconstructed time. n is the neutron multiplicity. . . . .	85
6.1	The average values of the mean energy for each analysis. The numbers in brackets are the coefficients of variation (CV). . . . .	88
6.2	The average values of the mean energy for the electron MC in SK-VI and SK-VII. The numbers in brackets are the coefficients of variation (CV). . . . .	90
6.3	The standard deviation of the $\text{diff}_{\text{pos}}$ for the electron and neutron MC. . . . .	92
6.4	The parameters determined by different methods. . . . .	95

A.1	The ratio of each signal. Gadolinium means the signals from neutron captures on gadolinium, hydrogen means those from neutron captures on hydrogen, and all means all signals. . . . .	106
A.2	The mean $N_{\text{eff}}$ for all signals (all) and signals only from neutron captures on Gd (gadolinium). . . . .	107

# Chapter 1

## Physics motivation

Accurately measuring neutrino oscillations and solar neutrinos contributes to understanding the properties of neutrinos, solar physics, and cosmic evolution. Moreover, the ability to observe the Diffuse Supernova Neutrino Background (DSNB) would enhance our understanding of supernova explosion mechanisms. Therefore, it is important to reduce systematic uncertainties in the detector and to accurately measure such phenomena.

In this chapter, we first describe neutrinos, and introductions to solar neutrinos and DSNB are given.

### 1.1 Neutrino

In Standard Model, neutrinos ( $\nu$ ) are fundamental particles classified as leptons and spin- $\frac{1}{2}$  fermions. They exist in three flavors: electron neutrino ( $\nu_e$ ), muon neutrino ( $\nu_\mu$ ), and tau neutrino ( $\nu_\tau$ ) along with their corresponding anti-neutrinos ( $\bar{\nu}$ ). Each flavor is associated with a charged lepton of the same name. Because neutrinos have no charge, they interact with other particles via weak force and gravity only.

The existence of neutrinos was first hypothesized by W. Pauli in 1930 to account for the conservation of energy in beta decay [1]. This prediction was experimentally confirmed in 1956 when C. Cowan and F. Reines observed anti-electron neutrinos [2]. Subsequently, muon neutrinos were discovered in 1962 by L. Laderman, M. Schwartz and J. Steinberger et al [3]. The existence of tau neutrinos was proposed after the discovery of the tau particle in 1975 and was first observed in the DONUT experiment by Niwa et al in 2000 [4]. The helicity of the neutrinos was measured by Goldhaber et al in 1958 [5].

Astrophysical neutrinos can be used to investigate the phenomena occurring at their source. So far, astrophysical neutrinos have been observed from fusion reactions in the center of the Sun [6], supernova explosions [7], and blazars [8].

#### 1.1.1 Neutrino oscillation

One of the most remarkable properties of neutrinos is their ability to oscillate between different flavors. This phenomenon, known as neutrino oscillation, was proposed by Maki, Nakagawa, and Sakata in the 1960s [9]. It describes how a neutrino produced as one flavor can later be observed as a different flavor. The first signs of neutrino oscillations were found in measurements of neutrinos produced in nuclear fusion reactions inside the Sun

(solar neutrinos). In the Homestakes experiment and Kamiokande experiment, the flux of solar neutrinos was measured and the flux of electron neutrinos was found to be smaller than predicted by the standard solar model (solar neutrino problem) [10] [11]. The signs of neutrino oscillation were found by the measurement of neutrinos produced in the atmosphere (atmospheric neutrinos) in the Kamiokande experiment in 1988 [12] and IMB experiment in 1992 [13]. Finally, the evidence of neutrino oscillations was found in the Super-Kamiokande experiment in 1998 [14]. In 2001, the solar neutrino flux measurement in Super-Kamiokande experiment [15] and SNO [16] experiment showed that solar neutrino problem is due to neutrino oscillations.

The neutrino flavor eigenstates  $|\nu_\alpha\rangle$  ( $\alpha = e, \mu, \tau$ ) can be expressed by their mass eigenstates  $|\nu_i\rangle$  ( $i = 1, 2, 3$ ):

$$|\nu_\alpha\rangle = \sum_{i=1}^3 U_{\alpha i}^* |\nu_i\rangle \quad (1.1)$$

where  $U$  is a  $3 \times 3$  unitary matrix which is called Pontecorvo-Maki-Nakagawa-Sakata (PMNS) matrix [9]. This PMNS matrix can be written as below:

$$\begin{aligned} U &= \begin{pmatrix} 1 & 0 & 0 \\ 0 & c_{23} & s_{23} \\ 0 & -s_{23} & c_{23} \end{pmatrix} \begin{pmatrix} c_{13} & 0 & s_{13}e^{-i\delta_{CP}} \\ 0 & 1 & 0 \\ -s_{13}e^{i\delta_{CP}} & 0 & c_{13} \end{pmatrix} \begin{pmatrix} c_{12} & s_{12} & 0 \\ -s_{12} & c_{12} & 0 \\ 0 & 0 & 1 \end{pmatrix} \\ &= \begin{pmatrix} c_{12}c_{13} & s_{12}c_{13} & s_{13}e^{-i\delta_{CP}} \\ -s_{12}c_{23} - c_{12}s_{13}s_{23}e^{i\delta_{CP}} & c_{12}c_{23} - s_{12}s_{13}s_{23}e^{i\delta_{CP}} & c_{13}s_{23} \\ s_{12}s_{23} - c_{12}c_{23}s_{13}e^{i\delta_{CP}} & -c_{12}s_{23} - s_{12}s_{13}c_{23}e^{i\delta_{CP}} & c_{13}c_{23} \end{pmatrix} \end{aligned} \quad (1.2)$$

where  $c_{ij} = \cos \theta_{ij}$  and  $s_{ij} = \sin \theta_{ij}$ , and  $\theta_{ij}$  is the mixing angle of mass eigenstate  $i$  and mass eigenstate  $j$ .  $\delta_{CP}$  is the phase angle related to the symmetry of charge and parity (CP symmetry). When  $\sin \delta_{CP} \neq 0$ , the CP symmetry of neutrino is broken, but this has not yet been observed. In a vacuum, the time evolution of the neutrino mass eigenstate  $|\nu_i(t)\rangle$  satisfies the following Schrödinger equation,

$$-i \frac{d}{dt} |\nu_i(t)\rangle = \mathcal{H} |\nu_i(t)\rangle = E_i |\nu_i(t)\rangle \quad (1.3)$$

$$|\nu_i(t)\rangle = \exp(-iE_i t) |\nu_i(0)\rangle \quad (1.4)$$

where  $E_i$  is the energy of mass eigenstate,  $\mathcal{H}$  is Hamiltonian, and  $t$  is the traveling time of the neutrino. From Eq. (1.1), the time evolution of a flavor eigenstate  $|\nu_\alpha(t)\rangle$  can be written as

$$|\nu_\alpha(t)\rangle = \sum_{i=1}^3 U_{\alpha i}^* \exp(-iE_i t) |\nu_i(0)\rangle \quad (1.5)$$

The amplitude when  $\nu_\beta$  is detected at time  $t$  starting from  $\nu_\alpha$  is

$$\begin{aligned} A(\nu_\alpha \rightarrow \nu_\beta) &= \langle \nu_\beta | \nu_\alpha(t) \rangle \\ &= \sum_i \sum_j \exp(-iE_i t) U_{\alpha i}^* U_{\beta j} \langle \nu_j | \nu_i \rangle \\ &= \sum_i \exp(-iE_i t) U_{\alpha i}^* U_{\beta i} \end{aligned} \quad (1.6)$$

The neutrino oscillation probability ( $\nu_\alpha \rightarrow \nu_\beta$ ) in a vacuum is given as follows.

$$\begin{aligned} P(\nu_\alpha \rightarrow \nu_\beta) &= |A(\nu_\alpha \rightarrow \nu_\beta)|^2 \\ &= \sum_i \sum_j U_{\alpha i}^* U_{\beta i} U_{\alpha j} U_{\beta j}^* \exp(-i(E_i - E_j)t) \end{aligned} \quad (1.7)$$

When the squared mass of a neutrino  $m_i^2$  is small compared to its momenta  $\mathbf{p}$ , its energy can be approximated as following,

$$E_i = \sqrt{p_i^2 + m_i^2} \simeq p_i + \frac{m_i^2}{2p_i} \simeq p + \frac{m_i^2}{2E_i} \quad (1.8)$$

where  $p_i$  and  $m_i$  represent the momentum eigenvalue and mass eigenvalue respectively. When  $E \simeq p_i = p_j$ , Eq. (1.7) becomes

$$\begin{aligned} P(\nu_\alpha \rightarrow \nu_\beta) &= \sum_{ij} U_{\alpha i}^* U_{\beta i} U_{\alpha j} U_{\beta j}^* \exp\left(-i \frac{\Delta m_{ij}^2}{2E} t\right) \\ &= \sum_i U_{\alpha i}^* U_{\beta i} U_{\alpha i} U_{\beta i}^* + \sum_{i \neq j} U_{\alpha i}^* U_{\beta i} U_{\alpha j} U_{\beta j}^* \exp\left(-i \frac{\Delta m_{ij}^2}{2E} L\right) \\ &= \sum_i U_{\alpha i}^* U_{\beta i} U_{\alpha i} U_{\beta i}^* + \sum_{i \neq j} U_{\alpha i}^* U_{\beta i} U_{\alpha j} U_{\beta j}^* \\ &\quad - 2 \sum_{i \neq j} U_{\alpha i}^* U_{\beta i} U_{\alpha j} U_{\beta j}^* \sin^2\left(\frac{\Delta m_{ij}^2 L}{4E}\right) \\ &\quad + i \sum_{i \neq j} U_{\alpha i}^* U_{\beta i} U_{\alpha j} U_{\beta j}^* \sin\left(\frac{\Delta m_{ij}^2 L}{2E}\right) \end{aligned} \quad (1.9)$$

where  $\Delta m_{ij}^2 = m_i^2 - m_j^2$  is a mass-squared difference,  $E$  is the average neutrino energy  $E \simeq \gamma(m_i + m_j)/2$  and  $t$  is replaced with a travel distance  $L = ct$ . An equation transformation for each of the terms in Eq. (1.9) yields the following,

$$\begin{aligned} (\text{1st term}) + (\text{2nd term}) &= \sum_{ij} U_{\alpha i}^* U_{\beta i} U_{\alpha j} U_{\beta j}^* \\ &= \sum_i (U_{\alpha i}^* U_{\beta i}) \sum_j (U_{\alpha j} U_{\beta j}^*) \\ &= \left| \sum_i U_{\alpha i}^* U_{\beta i} \right|^2 \\ &= \delta_{\alpha\beta} \end{aligned} \quad (1.10)$$

$$\begin{aligned} (\text{3rd term}) &= -2 \sum_{i \neq j} U_{\alpha i}^* U_{\beta i} U_{\alpha j} U_{\beta j}^* \sin^2\left(\frac{\Delta m_{ij}^2 L}{4E}\right) \\ &= -2 \sum_{i < j} (U_{\alpha i}^* U_{\beta i} U_{\alpha j} U_{\beta j}^* + U_{\alpha j}^* U_{\beta j} U_{\alpha i} U_{\beta i}^*) \sin^2\left(\frac{\Delta m_{ij}^2 L}{4E}\right) \\ &= -4 \sum_{i < j} \text{Re}[U_{\alpha i}^* U_{\beta i} U_{\alpha j} U_{\beta j}^*] \sin^2\left(\frac{\Delta m_{ij}^2 L}{4E}\right) \end{aligned} \quad (1.11)$$

$$\begin{aligned}
(4\text{th term}) &= i \sum_{i \neq j} U_{\alpha i}^* U_{\beta i} U_{\alpha j} U_{\beta j}^* \sin\left(\frac{\Delta m_{ij}^2 L}{2E}\right) \\
&= i \sum_{i < j} (U_{\alpha i}^* U_{\beta i} U_{\alpha j} U_{\beta j}^* - U_{\alpha j}^* U_{\beta j} U_{\alpha i} U_{\beta i}^*) \sin\left(\frac{\Delta m_{ij}^2 L}{2E}\right) \\
&= 2 \sum_{i < j} \text{Im}[U_{\alpha i}^* U_{\beta i} U_{\alpha j} U_{\beta j}^*] \sin\left(\frac{\Delta m_{ij}^2 L}{2E}\right)
\end{aligned} \tag{1.12}$$

where  $\delta_{\alpha\beta}$  is the Kronecker's delta. From Eq. (1.9) to Eq. (1.12), the neutrino oscillation probability becomes as follows.

$$\begin{aligned}
P(\nu_\alpha \rightarrow \nu_\beta) &= \delta_{\alpha\beta} - 4 \sum_{i < j} \text{Re}[U_{\alpha i}^* U_{\beta i} U_{\alpha j} U_{\beta j}^*] \sin^2\left(\frac{\Delta m_{ij}^2 L}{4E}\right) \\
&\quad + 2 \sum_{i < j} \text{Im}[U_{\alpha i}^* U_{\beta i} U_{\alpha j} U_{\beta j}^*] \sin\left(\frac{\Delta m_{ij}^2 L}{2E}\right)
\end{aligned} \tag{1.13}$$

From Eq. (1.13), if  $m_i \neq m_j$  then neutrino oscillations occur.

Considering two generations of neutrino oscillation at  $\nu_e \leftrightarrow \nu_\mu$  for simplicity, the unitary matrix is written as

$$U_{2 \times 2} = \begin{pmatrix} \cos \theta & \sin \theta \\ -\sin \theta & \cos \theta \end{pmatrix} \tag{1.14}$$

The neutrino oscillation probability  $P(\nu_e \leftrightarrow \nu_\mu)$  is written as follows.

$$\begin{aligned}
P(\nu_e \leftrightarrow \nu_\mu) &= \sin^2 2\theta \sin^2\left(\frac{\Delta m^2 L}{4E}\right) \\
&= \sin^2 2\theta \sin^2\left(\frac{\Delta m^2 L}{4E\hbar c}\right) \\
&= \sin^2 2\theta \sin^2\left(\frac{1.27\Delta m^2 [\text{eV}^2] L [\text{m}]}{E [\text{MeV}]}\right)
\end{aligned} \tag{1.15}$$

From Eq. (1.15), it can be seen that neutrino oscillations occur when there is a difference in the neutrino mass eigenvalues. The mixing angle  $\theta$  is related to the amplitude of the transition probability and the mass difference  $\Delta m^2$  is related to the vibration of the transition probability. Therefore, in neutrino oscillation experiments, the mixing angle is estimated by measuring the amplitude of the oscillation, and the mass difference is estimated by evaluating the energy (E) and distance (L) dependence of the oscillation.

Neutrino oscillation in a vacuum can be described by six parameters:

$$\theta_{12}, \theta_{23}, \theta_{13}, \Delta_{21}^2, \Delta_{32}^2, \delta_{CP} \tag{1.16}$$

These parameters have been measured by using various neutrino sources, such as solar, reactor, atmospheric, and accelerator neutrinos. The best-fit value of the global analysis of neutrino data is summarized in Table 1.1. There are two probabilities of mass ordering, which depend on the ordering of the neutrino mass eigenstates. This is because neutrino

	NO	IO
$\sin^2 \theta_{12}$	$0.307^{+0.013}_{-0.012}$	
$\sin^2 \theta_{23}$	$0.558^{+0.015}_{-0.021}$	$0.553^{+0.016}_{-0.024}$
$\sin^2 \theta_{13}$	$0.0219 \pm 0.0007$	
$\Delta m_{21}^2$ [ $/10^{-5}\text{eV}$ ]	$7.53 \pm 0.18$	
$\Delta m_{32}^2$ [ $/10^{-5}\text{eV}$ ]	$+2.455 \pm 0.028$	$-2.529 \pm 0.029$
$\delta_{CP}$ [ $\pi\text{rad}$ ]	$1.19 \pm 0.22$	

Table 1.1: Neutrino oscillation parameters [17]. NO is normal mass ordering and IO is inverted mass ordering.

oscillation experiments can mainly measure the absolute value of  $\Delta m^2$ , but they are not very sensitive to its sign. The order  $m_1 < m_2 < m_3$  is called Normal Ordering (NO), and the order  $m_3 < m_1 < m_2$  is called Inverted Ordering (IO). The relationship between  $m_1$  and  $m_2$  is fixed and  $\Delta m_{21}^2$  is a positive value. On the other hand, because the relationship between  $m_2$  and  $m_3$  is not fixed, the parameters depend on which mass ordering is used.

## 1.2 Solar neutrino

Solar neutrinos are produced during nuclear fusion reactions in the Sun. Every second, about  $2 \times 10^{38}$  electron neutrinos are generated, primarily through two processes: the pp-chain and the CNO cycle. Solar neutrinos have been observed in experiments such as Super-Kamiokande, Kamiokande, Homestake, KamLAND, SAGE, GALLEX/GNO, Borexino, and Sudbury Neutrino Observatory (SNO).

For the solar neutrino energy spectrum measurements, the position dependence of the detector affects the energy resolution and detection efficiency. This introduces systematic errors in the analysis of solar neutrino properties and solar interior models described in the following sections. Therefore, it is important to reduce the position dependence of the detector's energy scale.

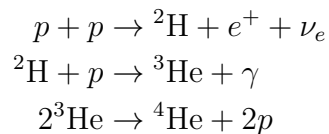
### 1.2.1 Solar neutrino production

#### pp-chain

In the pp-chain, solar neutrinos are produced by the following five reactions.

##### (1) pp neutrinos

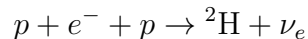
pp neutrinos account for 89.9% [18] of total solar neutrinos. Their flux was measured by the gallium experiments in SAGE [19] and GALLEX/GNO [20]. The Q value of a pp neutrino is 0.420 MeV.



##### (2) pep neutrinos

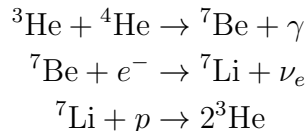
Pep neutrinos account for 0.22% [18] of total solar neutrinos. Because of two-body

decay, the energy of a pep neutrino is 1.442 MeV. Their flux was measured by Borexino [21].



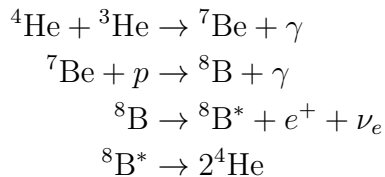
(3)  ${}^7\text{Be}$  neutrinos

${}^7\text{Be}$  neutrinos account for 7.2% [18] of total solar neutrinos. The energy of a  ${}^7\text{Be}$  neutrino depends on its state. It emits 0.861 MeV at a Branch ratio (BR) of 89.7% and 0.384 MeV at a BR of 10.3%. Their flux was measured by the Homestake experiment [22], Borexino [23], and KamLAND [24].



(4)  ${}^8\text{B}$  neutrinos

${}^8\text{B}$  neutrinos account for  $7.8 \times 10^{-3}\%$  of total solar neutrinos. They are produced through the following process called pp-3chain. Their production rate per second is small but they have high energy and their Q value is 17.98 MeV. Super-Kamiokande mainly uses these  ${}^8\text{B}$  neutrinos as the target for solar neutrino observations [25]. Other observation experiments were carried out at Kamiokande [26], SNO [27], KamLAND [28], and Borexino.



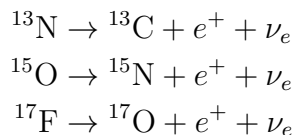
(5) hep neutrinos

Hep neutrinos account for  $3 \times 10^{-5}\%$  of total solar neutrinos. Super-Kamiokande and SNO showed that the upper limit of their flux was determined to be  $< 3.0 \times 10^4 \text{ cm}^{-2}\cdot\text{s}^{-1}$  [29], but hep neutrinos have not been measured yet. The Q value is 18.77 MeV.



### CNO cycle

1.6% of solar neutrinos derive from the CNO cycle. In the CNO cycle, solar neutrinos are produced by the following reactions:



These neutrinos are called  ${}^{13}\text{N}$  neutrinos,  ${}^{15}\text{O}$  neutrinos, and  ${}^{17}\text{F}$  neutrinos respectively. When the temperature of a stellar core is above  $1.8 \times 10^7$  K, the CNO cycle is dominant rather than pp-chain. However, because the solar core temperature is  $1.5 \times 10^7$  K, the main reaction is pp-chain for solar neutrino production. Figure 1.1 shows the solar neutrino energy spectrum predicted from the standard solar model. The pep neutrinos and  ${}^7\text{Be}$  neutrinos are produced with a two-body final state, so they have a single energy spectrum, while all the others are produced with three-body final state, so they have a broad energy spectrum.

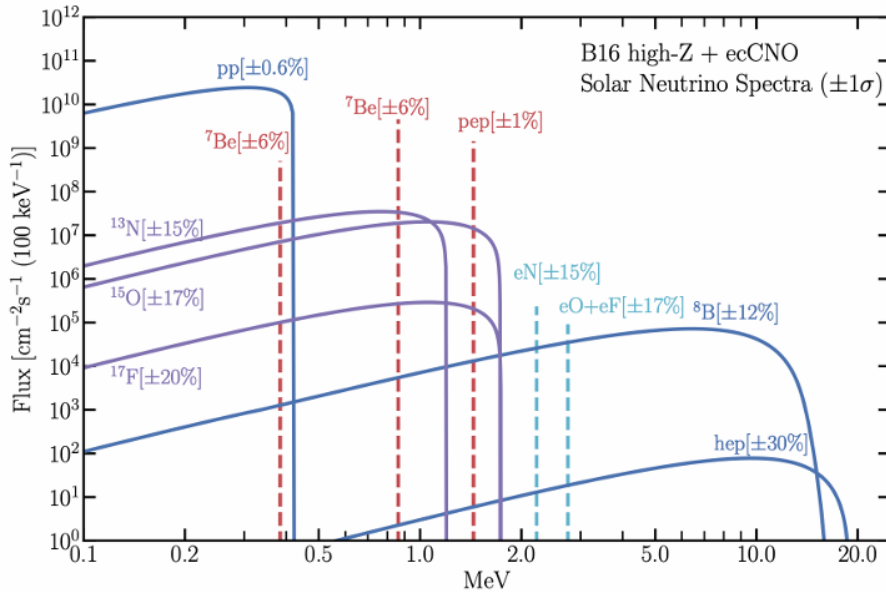


Figure 1.1: Energy spectrum of the solar neutrino

## 1.2.2 Solar neutrino problem

Solar neutrinos have been observed in experiments such as Homestake, GALLEX, GNO, SAGE, and Super-Kamiokande. However, the measured solar neutrino flux was only one-third to one-half of the value predicted by the Standard Solar Model (SSM). This discrepancy, known as the "solar neutrino problem", was a major challenge in neutrino physics. The discovery of neutrino oscillations provided a critical breakthrough in addressing this problem. To check the neutrino oscillation in solar neutrino, the SNO experiment was carried out in Canada which used 1,000 tons of heavy water to detect the solar neutrino. The specific point of the SNO experiment was that solar neutrino can be measured by three interactions; neutral current interaction, charged current interaction, and elastic scattering interaction.

$$\begin{aligned}
 \nu_\alpha + D &\rightarrow \nu_\alpha + p + n \\
 \nu_e + D &\rightarrow e^- + p + p \\
 \nu_\alpha + e^- &\rightarrow \nu_\alpha + e^-
 \end{aligned}$$

Because all flavor neutrinos interact via the neutral current interaction, the total solar neutrino flux does not change even when electron neutrinos change to other flavors by neutrino oscillation. Because only electron neutrinos interact via the charged current interaction, the flux of electron neutrinos can be measured. All flavor neutrinos have elastic scattering interaction with electrons, but electron neutrinos scatter via both the neutral current interaction and the charged current interaction, whereas mu neutrinos and tau neutrinos scatter via only the neutral current interaction. Therefore, the relationship between scattering cross sections for electron neutrinos and electrons  $\sigma(\nu_e, e)$  and that for mu neutrinos, tau neutrinos and electrons  $\sigma(\nu_{\mu,\tau}, e)$  is known to be  $\sigma(\nu_{\mu,\tau}, e) \simeq 0.16\sigma(\nu_e, e)$ . If the flux of electron neutrinos is  $\phi_e$  and the sum of the flux of mu neutrinos and tau neutrinos is  $\phi_{\mu,\tau}$ , the neutrino flux  $\phi_{NC}$  that are interacted via neutral current

interaction, the neutrino flux  $\phi_{CC}$  that are interacted via charged current interaction, and the neutrino flux  $\phi_{ES}$  that are interacted via elastic scattering are represented as follows.

$$\phi_{NC} = \phi_e + \phi_{\mu,\tau} \quad (1.17)$$

$$\phi_{CC} = \phi_e \quad (1.18)$$

$$\phi_{ES} \simeq \phi_e + 0.16\phi_{\mu\tau} \quad (1.19)$$

The value of those flux were determined as follows by measuring  $\phi_{NC}$ ,  $\phi_{CC}$ , and  $\phi_{ES}$  [30]. Figure 1.2 shows this result.

$$\phi_{NC} = 5.09_{-0.43}^{+0.44}(\text{stat.})_{-0.43}^{+0.46}(\text{syst.}) \times 10^6 \text{ cm}^{-2}\text{s}^{-1} \quad (1.20)$$

$$\phi_{CC} = 1.76_{-0.05}^{+0.06}(\text{stat.})_{-0.09}^{+0.09}(\text{syst.}) \times 10^6 \text{ cm}^{-2}\text{s}^{-1} \quad (1.21)$$

$$\phi_{ES} = 2.39_{-0.23}^{+0.24}(\text{stat.})_{-0.12}^{+0.12}(\text{syst.}) \times 10^6 \text{ cm}^{-2}\text{s}^{-1} \quad (1.22)$$

$$\phi_e = 1.76_{-0.05}^{+0.05}(\text{stat.})_{-0.09}^{+0.09}(\text{syst.}) \times 10^6 \text{ cm}^{-2}\text{s}^{-1} \quad (1.23)$$

$$\phi_{\mu\tau} = 3.41_{-0.45}^{+0.45}(\text{stat.})_{-0.45}^{+0.48}(\text{syst.}) \times 10^6 \text{ cm}^{-2}\text{s}^{-1} \quad (1.24)$$

$$(1.25)$$

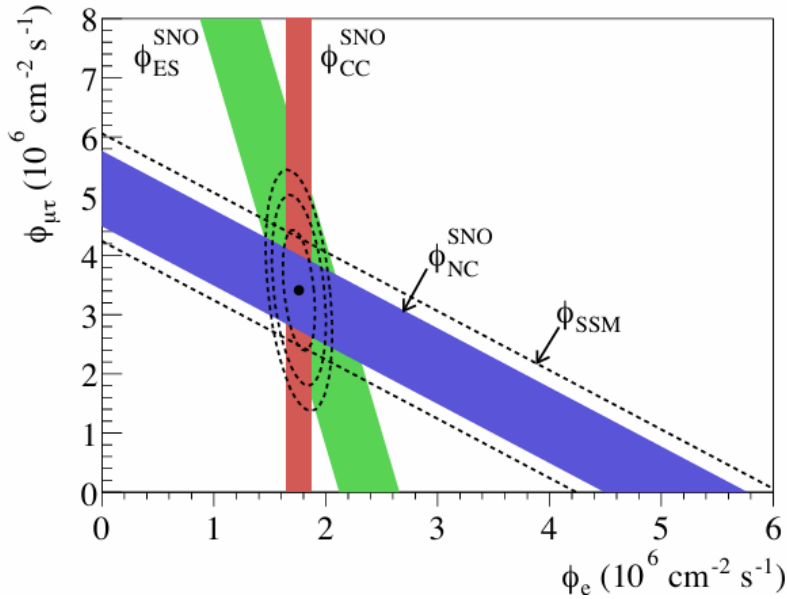


Figure 1.2: The measurement result in SNO experiment [30]. The red belt is 68 % C.L. of  $\phi_{CC}$ , the blue belt is that of  $\phi_{NC}$ , the green belt is that of  $\phi_{ES}$ , and the ellipses drawn with dotted lines are 68 %, 95 %, and 99 % C.L. from the inside. The belt between two dotted line is the 68 % C.L. of the SSM predicted value  $\phi_{SSM}$

Because  $\phi_{NC} = \phi_e + \phi_{\mu,\tau}$ , it was confirmed that  $\nu_e$  changes to  $\nu_\mu$  or  $\nu_\tau$ .  $\phi_{NC}(= \phi_e + \phi_{\mu\tau})$  agreed with the SSM predicted value  $\phi_{SSM} = 5.05_{-0.81}^{+1.01} \times 10^6 \text{ cm}^{-2}\text{s}^{-1}$ , so the solar neutrino problem was solved.

### 1.2.3 MSW effect of solar neutrino

As neutrinos travel through matter, they undergo elastic scattering with electrons, protons, and neutrons, causing the matter field to influence the neutrinos. Neutral-current

interactions occur across all neutrino flavors via neutral current Z boson exchange, while charged-current interactions are exclusive to electron neutrinos through charged current  $W^\pm$  boson exchange. Figure 1.3 illustrates those interactions. Consequently, as neutrinos

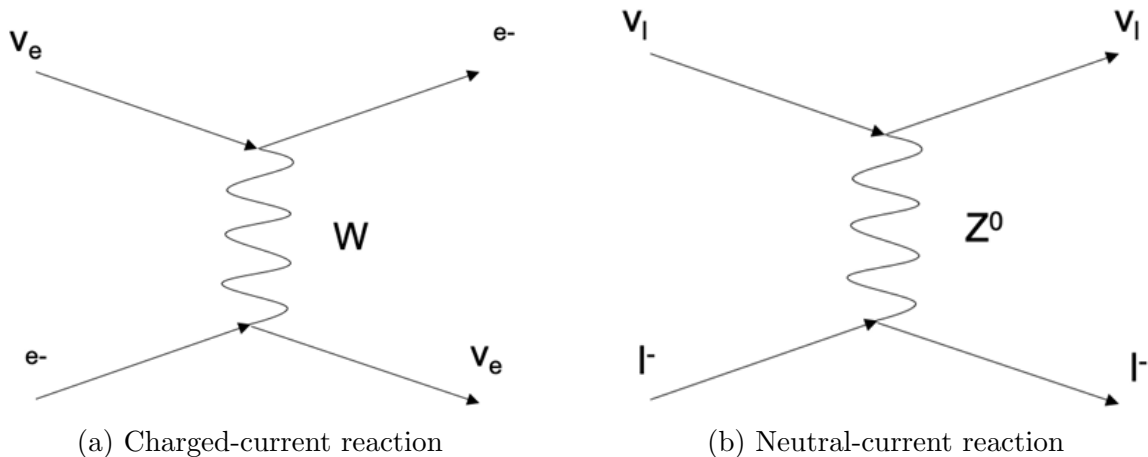


Figure 1.3: weak interaction of neutrinos

propagate through matter, additional contributions to the Hamiltonian arise, modifying the oscillation dynamics. The effective potentials for the different neutrino flavors are written as,

$$V_e = V_{CC} + V_{NC} \quad (1.26)$$

$$V_\mu = V_\tau = V_{NC} \quad (1.27)$$

where NC represents the neutral current and CC represents the charged current interactions. They are expressed as

$$V_{CC} = \sqrt{2}G_F n_e \quad (1.28)$$

$$V_{NC} = -\frac{\sqrt{2}}{2}G_F n_n \quad (1.29)$$

where  $n_e$  is the effective potential of the number density of electrons in the material,  $n_n$  is the effective potential of the number density of neutrons in the material, and  $G_F$  is the Fermi coupling constant.

Considering two generations of neutrino oscillation at  $\nu_e \leftrightarrow \nu_\mu$  for simplicity, from Eq. (1.1) and Eq. (1.3), the time evolution of neutrino flavor in a vacuum is expressed as follows.

$$i \frac{d}{dt} \begin{pmatrix} \nu_e \\ \nu_\mu \end{pmatrix} = \begin{pmatrix} E_1 \cos^2 \theta + E_2 \sin^2 \theta & \sin \theta \cos \theta (E_2 - E_1) \\ \sin \theta \cos \theta (E_2 - E_1) & E_1 \sin^2 \theta + E_2 \cos^2 \theta \end{pmatrix} \begin{pmatrix} \nu_e \\ \nu_\mu \end{pmatrix} \quad (1.30)$$

Using  $E_1 \simeq p + \frac{m_1^2}{2p}$ ,  $E_2 \simeq p + \frac{m_2^2}{2p}$ ,  $\Delta m^2 = m_2^2 - m_1^2$ , and  $p \simeq E$ , Eq. (1.30) becomes as follow.

$$i \frac{d}{dt} \begin{pmatrix} \nu_e \\ \nu_\mu \end{pmatrix} = \frac{\Delta m^2}{4E} \begin{pmatrix} -\cos 2\theta & \sin 2\theta \\ \sin 2\theta & \cos 2\theta \end{pmatrix} \begin{pmatrix} \nu_e \\ \nu_\mu \end{pmatrix} + \begin{pmatrix} p & 0 \\ 0 & p \end{pmatrix} \begin{pmatrix} \nu_e \\ \nu_\mu \end{pmatrix} + \frac{m_1^2 + m_2^2}{4p} \begin{pmatrix} 1 & 0 \\ 0 & 1 \end{pmatrix} \begin{pmatrix} \nu_e \\ \nu_\mu \end{pmatrix} \quad (1.31)$$

The second and third terms of Eq. (1.31) are diagonal matrices and they don't affect neutrino oscillations, so they can be ignored. When neutrinos pass through materials, neutral current interaction potentials  $V_{NC}$  are diagonal components and they also can be ignored. Therefore, Eq. (1.31) becomes as follows considering the additional contribution from the charged current interaction potentials  $V_{CC}$ .

$$\begin{aligned} i \frac{d}{dt} \begin{pmatrix} \nu_e \\ \nu_\mu \end{pmatrix} &= \left[ \frac{\Delta m^2}{4E} \begin{pmatrix} -\cos 2\theta & \sin 2\theta \\ \sin 2\theta & \cos 2\theta \end{pmatrix} + \begin{pmatrix} V_{CC} & 0 \\ 0 & 0 \end{pmatrix} \right] \begin{pmatrix} \nu_e \\ \nu_\mu \end{pmatrix} \\ &= \begin{pmatrix} -\frac{\Delta m^2}{4E} \cos 2\theta + \sqrt{2} G_F n_e & \frac{\Delta m^2}{4E} \sin 2\theta \\ \frac{\Delta m^2}{4E} \sin 2\theta & \frac{\Delta m^2}{4E} \cos 2\theta \end{pmatrix} \begin{pmatrix} \nu_e \\ \nu_\mu \end{pmatrix} \end{aligned} \quad (1.32)$$

To diagonalize the matrix, the mixing matrix in matter  $U_M$  is defined as,

$$U_M = \begin{pmatrix} \cos \theta_M & \sin \theta_M \\ \sin \theta_M & \cos \theta_M \end{pmatrix} \quad (1.33)$$

where the effective mixing angle  $\theta_M$  is given by

$$\tan 2\theta_M = \frac{\frac{\Delta m^2}{2E} \sin 2\theta}{\frac{\Delta m^2}{2E} \cos 2\theta - \sqrt{2} G_F n_e} \quad (1.34)$$

Therefore, the oscillatory term in Eq. (1.32) can be written as,

$$i \frac{d}{dt} \begin{pmatrix} \nu_e \\ \nu_\mu \end{pmatrix} = \frac{\Delta m_M^2}{4E} \begin{pmatrix} -\cos 2\theta_M & \sin 2\theta_M \\ \sin 2\theta_M & \cos 2\theta_M \end{pmatrix} \begin{pmatrix} \nu_e \\ \nu_\mu \end{pmatrix} \quad (1.35)$$

where  $\Delta m_M^2$  is the effective mixing mass difference,

$$\Delta m_M^2 = \Delta m^2 \sqrt{(\cos 2\theta - A)^2 + \sin^2 2\theta} \quad (1.36)$$

where

$$A = \frac{2\sqrt{2} G_F n_e E}{\Delta m^2} \quad (1.37)$$

The neutrino oscillation probability  $P_M(\nu_e \leftrightarrow \nu_\mu)$  in matter is expressed as follows.

$$P_M(\nu_e \leftrightarrow \nu_\mu) = \sin^2 2\theta_M \sin^2 \left( \frac{\Delta m_M^2 L}{4E} \right) \quad (1.38)$$

It can be seen that the oscillation probability is determined by the density of matter passing through in addition to the neutrino energy and flight distance. If  $A = \cos 2\theta$ , that is,

$$n_e^R = \frac{\Delta m^2}{2\sqrt{2} G_F E} \cos 2\theta \quad (1.39)$$

the neutrino mixing is maximum. This effect is called the MSW (Minkheyev-Smirnov-Wolfenstein) effect [31].

Solar neutrinos are produced near the high-density solar center and are therefore affected by the MSW effect in the process of reaching the surface of the Sun. Figure 1.4 shows the dependence of neutrino mass on electron density in the Sun. The flavors of neutrinos are mixed, so they transition along the solid line in the figure, keeping  $\Delta m_M^2 \neq 0$ . Thus, electron neutrinos produced near the dense solar center change to mu neutrinos when they come to the solar surface ( $n_e = 0$ ) due to the MSW effect.

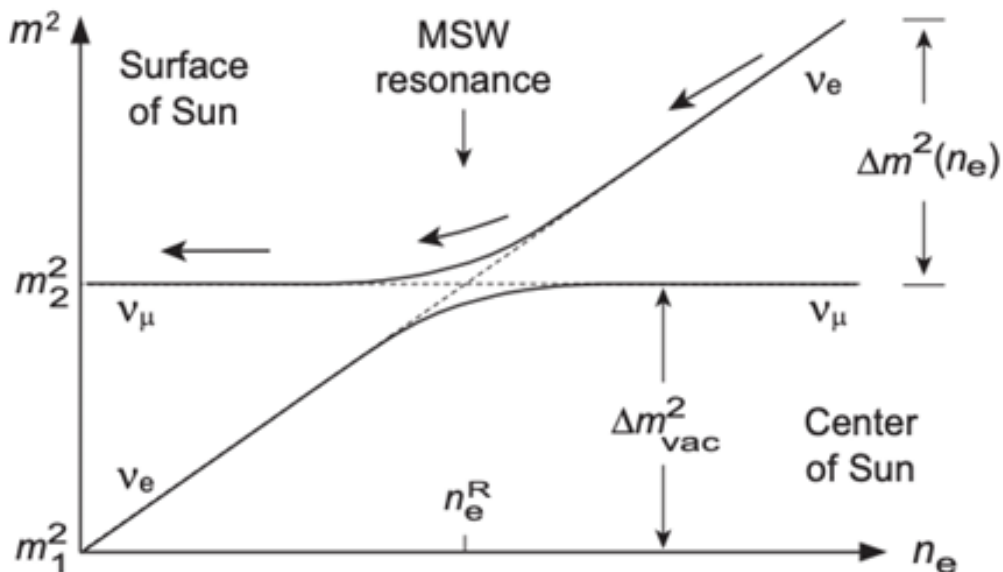


Figure 1.4: Electron density dependence of neutrino masses in the sun [32]. The vertical axis represents neutrino mass squared, the horizontal axis represents electron density.

### 1.2.4 Up-turn effect of solar neutrino

Due to the MSW effect in the Sun, an electron neutrino with high energy ( $> 5$  MeV) changes to the other flavor neutrino. While in the low energy region ( $< 3$  MeV), the MSW effect becomes weak. As a result, the survival probability of electron neutrinos is a lower value of  $\simeq 0.3$  at high energy ( $> 10$  MeV) and a higher value of  $\simeq 0.6$  at low energy ( $< 1$  MeV) [33]. This energy dependence of the survival probability is called "up-turn". Figure 1.5 shows the experimental results of the up-turn effect. The SK+SNO results show a weak hint of the spectrum upturn consistent with the prediction of the MSW effect.

In Figure 1.5, the green line represents the theoretical prediction using the solar neutrino measurement results of  $\Delta m_{21}^2$  and  $\theta_{21}$ , and the blue line represents that using the solar neutrino and reactor neutrino measurement in KamLAND result. If the up-turn effect can be measured precisely, this difference can be checked experimentally. Therefore, it needs to measure the solar neutrino energy more precisely and to reduce the systematic uncertainty of the detector.

### 1.2.5 Day/night effect of solar neutrino

When solar neutrinos are measured on the Earth, they fly overhead during the day, but through the Earth at night. Solar electron neutrinos  $\nu_e$  change to  $\nu_\mu$  or  $\nu_\tau$  by MSW effect in the Sun, but those changed  $\nu_\mu$  or  $\nu_\tau$  become electron neutrinos  $\nu_e$  again by passing through the Earth. The MSW effect on neutrinos can be measured directly by comparing solar neutrino flux during the day and night. This result places the limit on the neutrino oscillation parameter  $\Delta m_{21}^2$ . If solar neutrino flux in the day is  $\Phi_D$  and that in the night

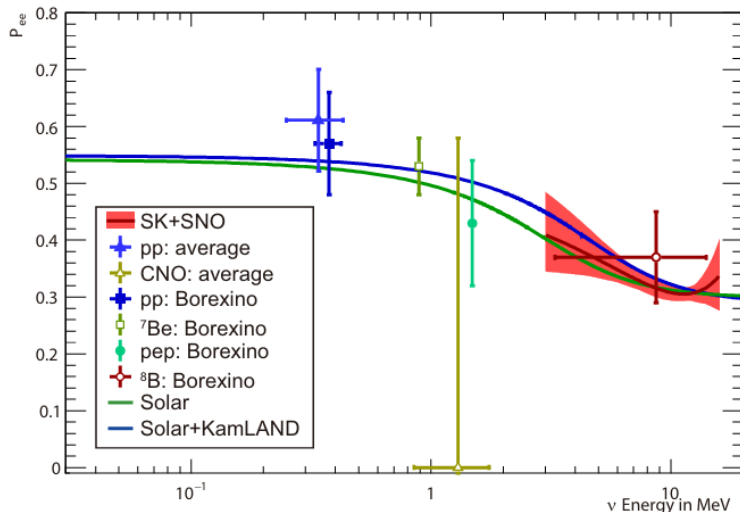


Figure 1.5: The electron neutrino survival probability as a function of neutrino energy and solar neutrino measurements [33]. The red area is theoretically predicted using the SK+SNO spectrum data.

is  $\Phi_N$ , the day/night asymmetry of the flux  $A_{DN}$  is written as follows.

$$A_{DN} = \frac{\Phi_D - \Phi_N}{(\Phi_D + \Phi_N)/2} \quad (1.40)$$

The solar neutrino flux day/night asymmetry  $A_{DN}$  is determined to be  $A_{DN} = -3.6 \pm 1.6(\text{stat.}) \pm 0.6(\text{syst.}) \%$  by Super-Kamiokande (SK-IV) [33].

## 1.2.6 Oscillation parameter determination with solar neutrinos

In the solar neutrino measurement, the electron neutrinos disappearance phenomenon  $\nu_e \rightarrow \nu_{\mu,\tau}$  is mainly measured, so oscillation parameter  $\theta_{12}$  and  $\Delta m_{21}^2$  are mainly detectable. Up to now, the values of  $\theta_{12}$  which were measured by solar neutrino measurement and reactor neutrino measurement in KamLAND respectively agree with each other, whereas the values of  $\Delta m_{21}^2$  have about  $1.5\sigma$  difference between those two measurements (Figure 1.6) [33]. The measured neutrinos differ between solar neutrino and reactor neutrino measurements in KamLAND. That is to say, The solar neutrinos are  $\nu_e$ , whereas the reactor neutrinos are  $\bar{\nu}_e$ . Solar neutrino oscillation is strongly affected by the MSW effect, but reactor neutrino oscillation can be approximated to oscillation in a vacuum. One of the challenges of solar neutrino measurement is to determine whether this  $\Delta m_{21}^2$  difference is significant or not by measuring the up-turn effect and day/night asymmetry of solar neutrino flux more precisely. The calibration to reduce the systematic uncertainty is important for the accurate analysis of these effects. In Super-Kamiokande, the current systematic error for the solar neutrino energy spectrum measurement is 0.48 % [33] and more measurements with this level of systematic uncertainty will be required.

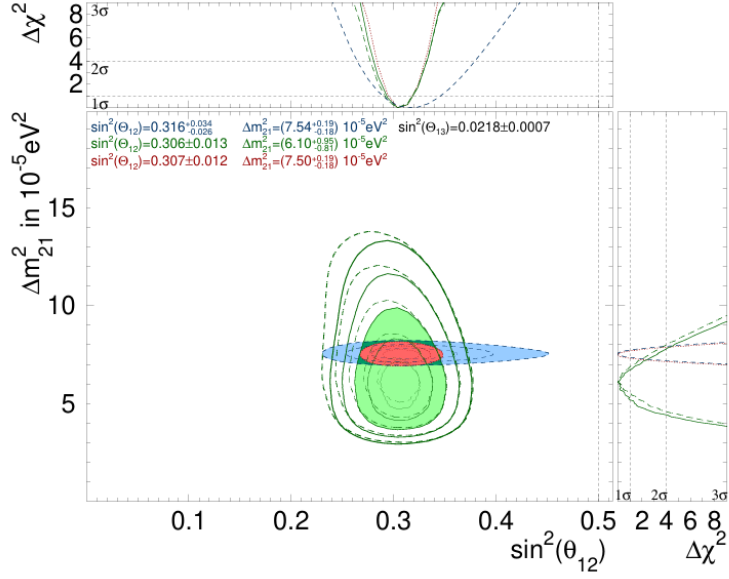


Figure 1.6: The allowable range of  $\theta_{12}$  and  $\Delta m^2_{21}$  which were measured by solar neutrino measurement and reactor neutrino measurement in KamLAND [33]. The blue area represents the result of solar neutrino measurement, and the green one represents the result of reactor measurement in KamLAND. The red area represents the combined result.

## 1.3 Diffuse Supernova Neutrino Background (DSNB)

### 1.3.1 Supernova explosion

A supernova explosion is an explosion that occurs when a massive star or white dwarf reaches the end of its life or exceeds a certain amount of mass due to interaction with another dwarf star. After the explosion, the energy ( $10^{51}$  erg) spreads throughout the universe and is the basis for the evolution of galaxies, planets, and other stars. Therefore, supernova events are of great interest to astrophysics. Supernova explosions are classified according to the emission lines in the spectrum as follows.

#### 1. Type I supernova explosion

An explosion that has no absorption line of H in the optical observation spectrum is classified as Type I. Type I explosion can be further classified into four categories as follows.

##### (1) Type Ia

The Type I explosion that has an absorption line of Si in the optical observation spectrum is classified as Type Ia. The surface of a red dwarf is sucked in by a nearby white dwarf, and it creates a disk of gas. The white dwarf gradually grows in size, and when it exceeds 1.4 times the mass of the Sun (the Chandrasekhar limit), a fusion reaction of carbon inside the white dwarf causes a thermo-runaway explosion. This type of explosion is the brightest explosion of the Type I explosion.

##### (2) Type .Ia

This type represents explosions where the brightness of the explosion and its duration is only 10 % of that of Type Ia. A white dwarf (the main star) made up of carbon and

oxygen attracts another white dwarf (the companion star) made up mainly of He, and the helium from the companion star covers the main star. When helium exceeds a certain amount, it explodes very brightly over a short time. At the time of the explosion, only helium explodes and two white dwarfs keep revolving around each other, so this explosion occurs repeatedly.

### **(3) Type Ib**

The Type I explosion that has an absorption line of He in the optical observation spectrum is classified as Type Ib. This phenomenon occurs when a star explodes at the end of its life due to the gravitational collapse of its central core. It is considered that because the layer of hydrogen is removed by strong stellar wind or interaction with a companion star that has three to four times the mass of the Sun, the spectrum absorption line of hydrogen disappears.

### **(4) Type Ic**

The Type I explosion that has no absorption line of both Helium and hydrogen is classified as this explosion. Same as the Type Ib explosion, this is a phenomenon when a star explodes at the end of its life due to the gravitational collapse of its central core. It is considered that because the layers of hydrogen and helium are removed by stellar wind or interaction with a companion star, those spectrum lines disappear at the explosion.

## **2. Type II supernova explosion**

Unlike the Type I explosion, an explosion with the optical observation spectrum of hydrogen is classified as this explosion. It is considered that this explosion occurs when a star with over eight times the mass of the Sun runs out of materials that are needed for nuclear fusion reaction and the pressure to support the entire star is removed. This explosions are classified according to changes in luminous intensity as follows.

### **(1) Type IIP**

This is the Type II supernova explosion where the shape of the light intensity curve slightly decreases beyond the peak and then flattens out.

### **(2) Type IIL**

This is the Type II supernova explosion where the shape of the light intensity curve monotonically decreases beyond the peak.

Type Ia supernova explosions are caused by the reaction of thermonuclear fusion. Neutrinos emitted by Type Ia supernova explosions have energies of  $10^{49}$  erg or less. On the other hand, the Type Ib, Ic, and II supernova explosions are caused by core collapse. Neutrinos emitted by them have energies of  $10^{53}$  erg.

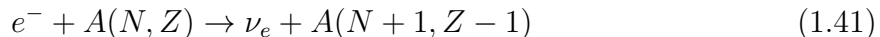
### **1.3.2 Supernova neutrino**

Supernova neutrinos are produced mainly by Type Ib, Ic, and II supernova explosions which are caused by core collapse. How neutrinos are emitted from these supernova explosions is described below.

#### **(1) Start of gravitational collapse**

The core of the star starts to collapse and the Fermi energy of electrons increases.

Then an element of the star captures an electron and an electron neutrino is emitted.



The density of the core increases and neutrino confinement (the reverse reaction of Eq. (1.41)) occurs. The neutrinos are absorbed into the core due to the neutrino confinement. However, because the time scale of neutrino emission is smaller than that of core collapse, the produced neutrinos may escape to the outside.

(2) Production of neutrino sphere

The density of the core increases as a result of progressive gravitational collapse, then the core is opaque to neutrinos. When the core becomes ultra-dense above  $10^{11}$  g/cm<sup>3</sup>, a region (neutrino sphere) is created in the center of the star where neutrinos are trapped and can only gradually escape.

(3) Shock wave

When the core density reaches the nucleon density, neutron degeneracy pressure stops contraction. However, since material falls from the outer core at supersonic speed, a shock wave is generated at the interface between the inner core and the outer core.

(4) Neutronization burst

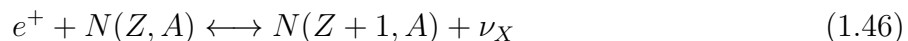
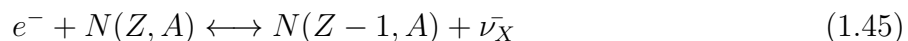
Electron neutrinos are produced by the capture of surrounding electrons by protons which is produced during shock wave propagation.



While the shock wave is propagating inside the neutrino sphere, the electron neutrinos cannot escape, but when the shock wave reaches the outside of the neutrino sphere, the electron neutrinos can fly out. This is called  $\nu_e$  neutronization burst. Also, a Proto Neutron Star (PNS) is formed inside the star.

(5) Cooling of the PNS

After the shock wave has passed through, the nuclei, electrons, and positrons produced fall into the PNS. The various flavors of neutrinos are produced at the time. The neutrinos heat the material behind the shock wave, reviving the stalled shock wave. The PNS is also cooled because of the heat brought out by the neutrinos.



where  $\gamma^*$  is plasmon.

(6) Supernova explosion

When the shock wave reaches the surface of the star, a supernova explosion occurs, blowing away all the outer layers. Only the neutron star produced by the cooling of PNS is left.

Different flavor neutrinos evolve differently, giving the following energy hierarchy.

$$\langle E_{\nu_e} \rangle < \langle E_{\bar{\nu}_e} \rangle < \langle E_{\nu_X} \rangle \quad (1.50)$$

where  $X = \mu, \tau$ . Figure 1.7 shows the time distribution of neutrino energy and luminosity obtained by simulation.  $\nu_X$  in the figure represents  $\nu_X = (\nu_\mu + \bar{\nu}_\mu + \nu_\tau + \bar{\nu}_\tau)/4$ . These energies range from 10 MeV to around 20 MeV.

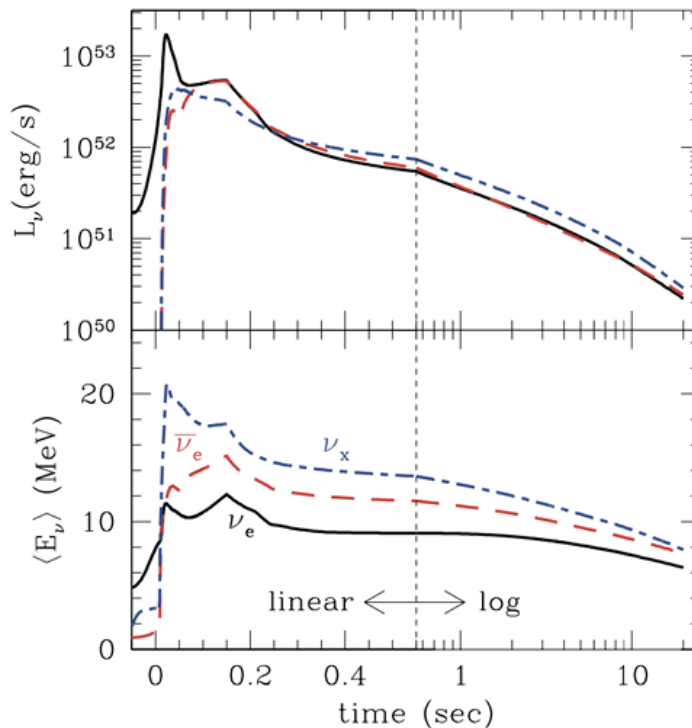


Figure 1.7: Time distribution of supernova neutrino energy and luminosity [34].

### 1.3.3 Diffuse Supernova Neutrino Background (DSNB)

The Diffuse Supernova Neutrino Background (DSNB) is the overall neutrino flux of all core-collapse Supernova that happened in the history of the universe. There are DSNB in the universe from  $10^{17}$  supernova explosions from the Big Bang to the present. The number density of DSNB is written as follows.

$$\begin{aligned} dn_\nu &= R_{SN}(z)(1+z)^3 \frac{dt}{dz} dz \frac{dN_\nu(E'_\nu)}{dE'_\nu} dE'_\nu (1+z)^{-3} \\ &= R_{SN}(z) \frac{dt}{dz} dz \frac{dN_\nu(E'_\nu)}{dE'_\nu} dE'_\nu (1+z) \end{aligned} \quad (1.51)$$

where  $R_{SN}$  represents the core-collapse supernova rate as a function of redshift  $z$  and  $R_{SN} \times (1+z)^3$  means the core-collapse supernova rate per unit time.  $\frac{dz}{dt}$  is the relationship between cosmic time  $t$  and redshift  $z$  given by,

$$\frac{dz}{dt} = -H_0(1+z)\sqrt{\Omega_\Delta + \Omega_m(1+z)^3} \quad (1.52)$$

where  $H_0$  is the Hubble constant and  $\Omega$  is the cosmological parameters.  $\frac{dN_\nu(E'_\nu)}{dE'_\nu}$  represents the number of DSNB with energy  $E'_\nu$  from a single supernova explosion. The energy  $E'_\nu$  of neutrinos with redshift  $z$  can be represented as  $E'_\nu = (1+z)E_\nu$ . Regarding the differential flux of DSNB  $\frac{dF_\nu}{dE_\nu}$ , there is an equation  $\frac{dF_\nu}{dE_\nu} = c \frac{dn_\nu(E_\nu)}{dE_\nu}$ , therefore the following equation holds.

$$\frac{dF_\nu}{dE_\nu} = c \int_0^{z_{max}} R_{SN}(z) \frac{dN_\nu(E'_\nu)}{dE'_\nu} (1+z) \frac{dt}{dz} dz \quad (1.53)$$

where  $z_{max}$  means the upper limit of redshift when core collapse occurs.

Many theoretical models have been proposed to predict the DSNB flux. Figure 1.8 shows the predicted energy distribution of the  $\bar{\nu}_e$  flux [35]. Various searches for DSNB have been conducted so far, but they have not yet been discovered. In Super-Kamiokande, gadolinium has been loaded to improve the neutron detection rate and detection capability of DSNB. DSNB event rate is expected to be several times per year [35]. If the DSNB are observed and their energy spectra can be compared with theoretical predictions, the mechanism and rate of supernova explosions also can be understood, as well as the initial mass distribution of stars.

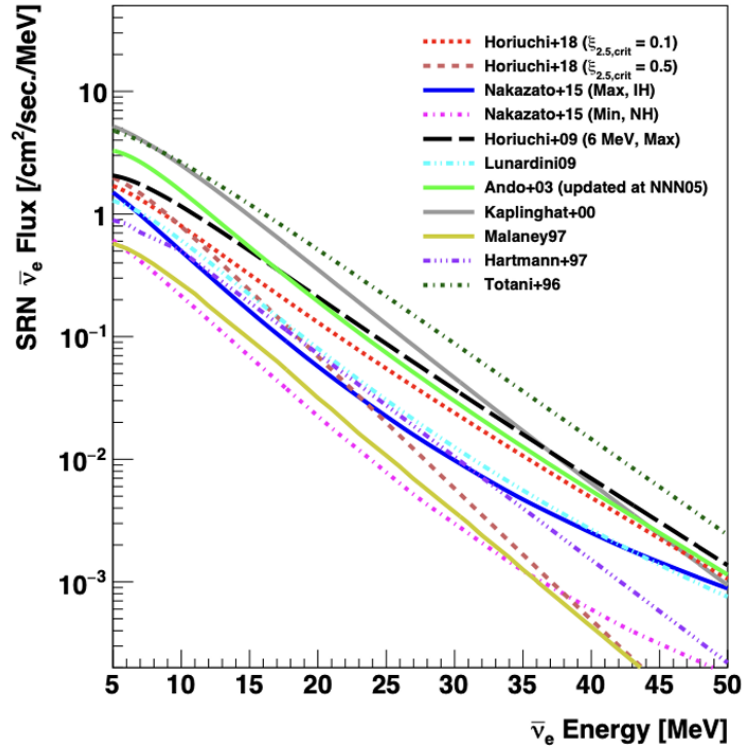


Figure 1.8: DSNB  $\bar{\nu}_e$  flux prediction from various theoretical models [35]

# Chapter 2

## Super-Kamiokande experiment

The Super-Kamiokande detector is the large water Cherenkov detector [36, 37]. The Super-Kamiokande experiment has a wide variety of astroparticle and particle physics targets. The main purposes of the experiment are to reveal the properties of neutrinos, to understand the history of the universe by observing neutrinos, and to test the grand unified theory by searching for proton decays.

In this chapter, the overview of the detector, the principle of detection, and the data acquisition system are explained.

### 2.1 Super-Kamiokande detector

The Super-Kamiokande detector is located 1,000 m underground in Mt. Ikenoyama, in the Kamioka mine, Hida City, Gifu Prefecture, Japan. The overview of the detector is shown in Figure 2.1 [37]. The main reason why the detector is placed underground is to shield the cosmic ray muons. It is hard to measure neutrinos on the ground because neutrinos very rarely interact with water and there are so many background signals produced by cosmic ray muons showering constantly. On the other hand, in the deep underground, the surrounding rock significantly reduces cosmic ray muons and background signals, so cosmic ray muons are reduced to about 1/100,000th at the depth of the SK detector [36].

The detector is a cylindrical stainless tank with 39.3 m in diameter and 41.4 m in height. The detector is comprised of the Inner detector (ID) and the Outer detector (OD) as shown in Figure 2.2. Photomultiplier tubes (PMT) are located on the inner and outer walls of the detector. Previously, pure water was used as the detector medium and the weight was about  $5 \times 10^4$  tons. In 2020, gadolinium with a concentration of 0.01 % was introduced. The concentration was increased to about 0.03 % in 2022. Super-Kamiokande with gadolinium will be explained in Section 2.4.

#### 2.1.1 Inner detector

As explained in the last section, the Super-Kamiokande detector is divided into two regions: the Inner detector (ID) and the Outer detector (OD). The ID and the OD are separated by a stainless steel structure called a super module as shown in Figure 2.3 [36]. The ID is a cylindrical detector with 33.8 m in diameter and 36.3 m in height.

20-inch PMTs are installed on the inner wall facing inside. They detect the Cherenkov

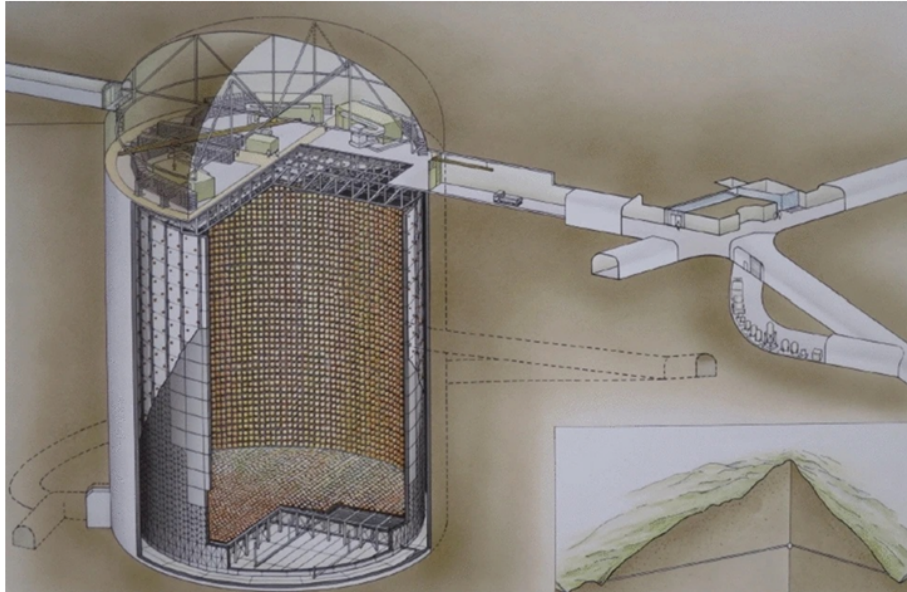


Figure 2.1: The overview of the detector [37]

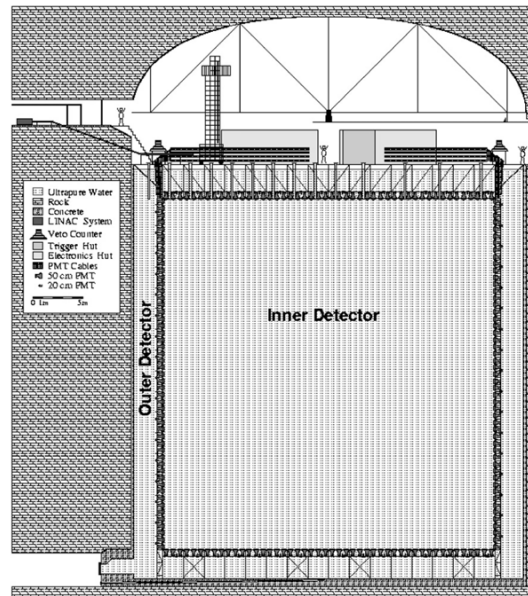


Figure 2.2: The cross-section of SK detector [36].

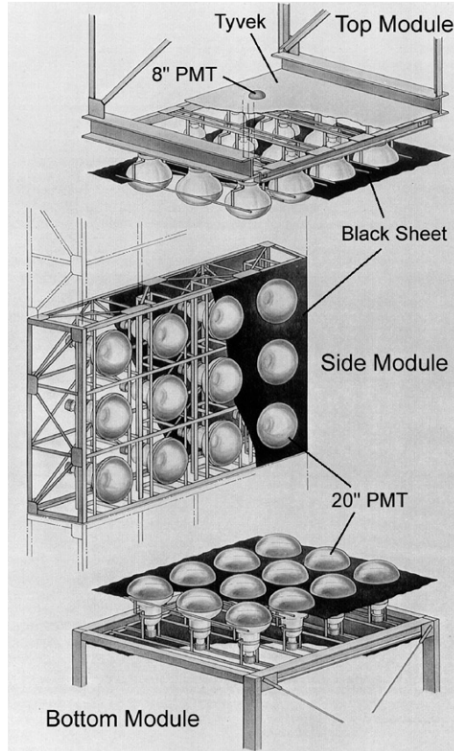


Figure 2.3: The super module [36].

light emitted by charged particles in the ID and are responsible for reconstructing the position and energy of the event. Currently, there are 1,740 PMTs at the top of the ID, 1,739 PMTs at the bottom of the ID, and 7,650 PMTs at the side of the ID. The total number of the ID PMTs is 11,129. They cover about 40 % of the surface area of the ID. The surfaces without the PMTs are covered with black sheets to prevent light reflection on the wall surface.

Hamamatsu R3600 developed by Hamamatsu Photonics is used for the ID PMT. Figure 2.4 shows the schematic view of Hamamatsu R3600. The photocathode of Hamamatsu R3600 consists of bialkali (Sb-K-Cs) to detect the Cherenkov light. The detectable wavelength range of this PMT is from 280 nm to 660 nm, and the peak of quantum efficiency (QE) is about 22 % around 390 nm (Figure 2.5). In Super-Kamiokande, a high voltage of about 2,000 V is applied to the dynode, and the amplification factor is about  $10^7$  times. The time resolution is about 2.2 ns. The performance of the ID PMTs is summarized in Table 2.1.

The coordinate of the SK detector is taken as shown in Figure 2.6. The x and y-axes are taken in the horizontal direction and the z-axis in the vertical direction. The origin point of each axis is the center of the SK detector (the black dot in the figure).

In the wake of the November 2001 explosion (described in section 2.1.4), the PMTs are covered with acrylic and the fiber reinforced plastic (FRP) covers to prevent the chain failure.

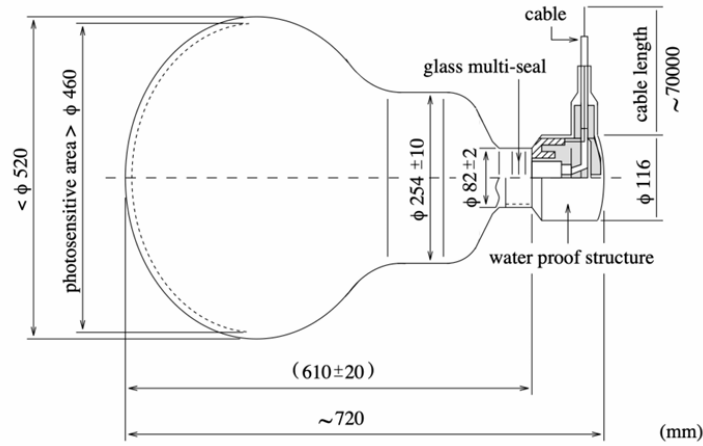


Figure 2.4: Schematic view of Hamamatsu R3600 [36].

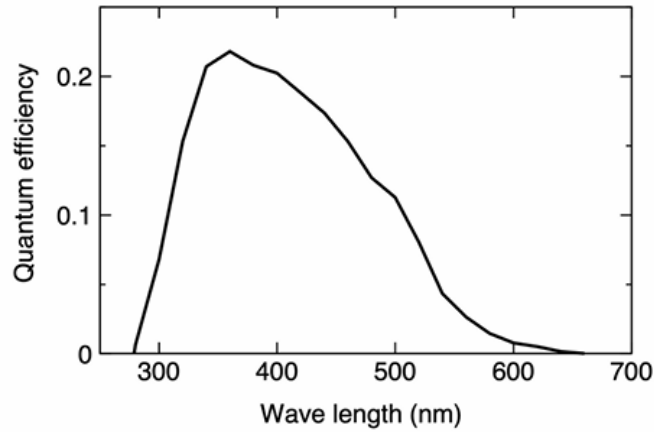


Figure 2.5: The wavelength dependence of quantum efficiency of the PMT [36].

Model number	R3600
Photocathode material	Bialkali (Sb-K-Bs)
Photoelectron collection efficiency	70 %
Quantum efficiency	22 % ( $\lambda$ : 360 - 400 nm)
Dynode structure	11-stage Venetian blind type
Gain	$10^7$ at 2000 V
Dark current	200 nA at $10^7$ gain
Dark rate	3 kHz at $10^7$ gain
Transit time	90 ns at $10^7$ gain
Transit time spread	2.2 ns ( $1\sigma$ )
Weight	13 kg
Pressure resistance	6 kg/cm <sup>2</sup>

Table 2.1: Typical performance of the ID PMTs [36].

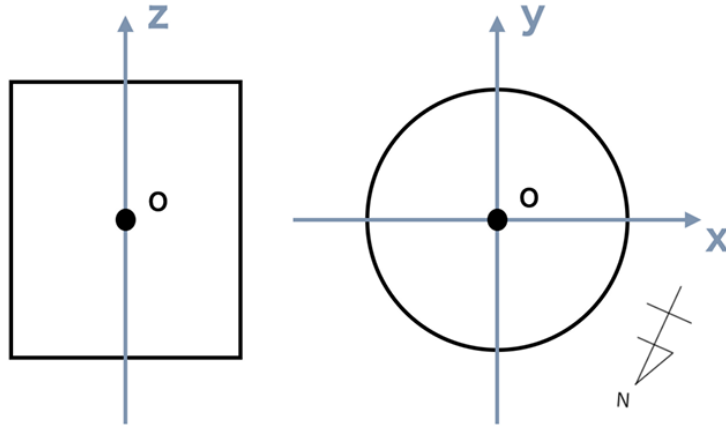


Figure 2.6: The coordinate of the SK detector.

### 2.1.2 Outer detector

OD is the region outside the ID, covering a thickness of 2.05 m on the top and bottom surfaces and 2.2 m on the side. The volume is about  $1.75 \times 10^4$  tons. 1,885 8-inch PMTs are installed facing outwards on the walls. 1,275 PMTs are attached to the side, 308 PMTs to the bottom, and 302 PMTs to the top. The OD is responsible for identifying cosmic ray muons and shielding neutrons and gamma rays produced in the surrounding rock. The surfaces except the PMTs are covered with a white reflective sheet called a Tyvek sheet to improve the light collection efficiency and to prevent light generated in the OD from entering the ID.

Hamamatsu R5912 is mainly used for the Outer detector PMT. Because the OD detector PMTs are small and there are a few PMTs, a Wavelength-shifter (WS) plate is attached to each PMT to improve coverage rate. The size of the WS plate is  $60 \text{ cm} \times 60 \text{ cm} \times 1.3 \text{ cm}$  and it is acrylic board with 50 mg/L bis-MSB ( $\text{C}_{24}\text{H}_{22}$ ) added. It absorbs photons whose wavelength is in the ultraviolet region and emits light whose wavelength is in the blue to green region. Thanks to the WS plates, the OD's collection efficiency of the light reaches 60 %. On the other hand, the time resolution is reduced to about 13 to 15 ns.

The positional relationship between the ID PMTs and the OD PMTs is shown in Figure 2.7

### 2.1.3 Geomagnetic field compensation coil

Photo-electrons emitted from the photocathode of the PMTs are collected to the dynode by the electric field in the PMTs. The collection efficiency is affected by the geomagnetism. There is an average geomagnetic field of 450 mG around the SK detector. To prevent the influence of this magnetic field, Helmholtz coils are installed in the horizontal and vertical directions around the detector as shown in Figure 2.8. There are 26 coils in total. Those coils reduce the magnetic field to about 50 mG [39].

In October 2023, one of the vertical coils went off, and in November 2023, another vertical coil also went off. These vertical coils were repaired in December 2023. Furthermore, in December 2023, one of the horizontal coils went off, and due to this problem, all of

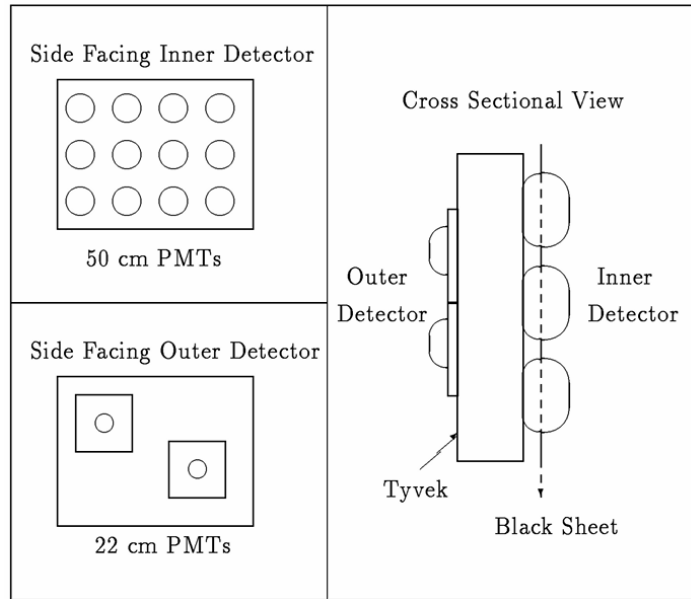


Figure 2.7: The positional relationship between the ID PMTs and the OD PMTs [38].

coils B in Figure 2.8 were off. Those coil problems decreased about 10-20 % in collection efficiency for about 20 % of PMTs in the barrel. Those broken horizontal coils and one of the vertical coils were replaced with new coils in July 2024.

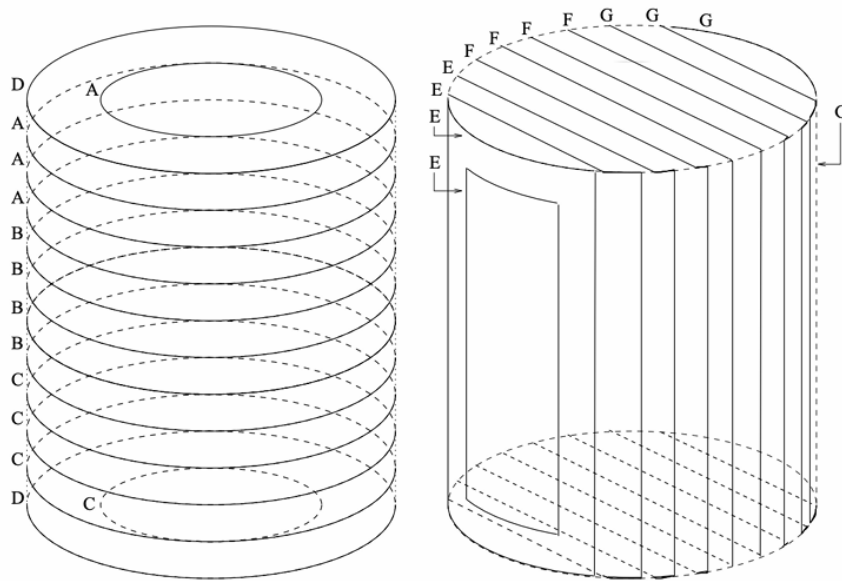


Figure 2.8: The overview of the compensation coil [40].

### 2.1.4 Data acquisition phase of Super-Kamiokande

Super-Kamiokande detector has been operated since April 1996, and there are 8 data acquisition phases in total. Table 2.2 shows the detector performance in each phase, and each phase is explained below.

## **SK-I**

SK-I is a phase that officially began operation on April 1, 1996, and continued until July 2001. The electronics called Analog Timing Module (ATM) were used for measurement during this phase. The total measurement date is 1,496 days. There were 11,146 ID PMTs and 1,885 OD PMTs. The coverage rate of PMTs against the surface of the ID was about 40 %. After the end of SK-I, damaged PMTs were changed. However, on November 11, 2001, the bottom PMTs imploded consecutively and 6,779 ID PMTs and 1,017 OD PMTs were broken. As a result, the anti-shock cases comprised of acrylic and FRP were attached to the PMTs.

## **SK-II**

After the PMT chain implosion accident was settled and the anti-shock cases were developed, SK-II started in October 2002 and continued until October 2005. There were only 5,128 PMTs in total and the coverage rate of PMTs reduced to about 20 %. As a result, the energy resolution and threshold got worse.

## **SK-III**

In this phase, new ID PMTs were produced and attached to the ID. SK-III started in July 2006. There were 11,129 ID PMTs and 1,885 OD PMTs in total and the coverage rate of PMTs returned to 40 %. The energy resolution also returned to the same level as SK-I. This period continued until August 2008.

## **SK-IV**

SK-IV started in September 2008. The electronics were replaced from ATM to QBEE. QBEE is explained in detail in Section 2.3. This period continued until May 2018.

## **SK-V**

For the SK-Gd experiment, waterproofing reinforcement work, improvement of piping inside the tank, and replacement of faulty PMTs, etc was carried out from July 2018 to January 2019. Data-taking period from the end of January 2019 after the completion of the repair work to June 2020 when the gadolinium addition work started.

## **SK-VI**

From July 2020, 13 tons of  $\text{Gd}_2(\text{SO}_4)_3 \cdot 8\text{H}_2\text{O}$  was introduced into the detector. This loading was completed in August 2020 and SK-VI started. The mass concentration of Gd was approximately 0.011 % and the neutron capture efficiency was about 50 %. SK-IV continued until June 2022.

## **SK-VII**

From June 2022, the additional about 26 tons of  $\text{Gd}_2(\text{SO}_4)_3 \cdot 8\text{H}_2\text{O}$  was introduced into the detector. This loading was completed in July 2022 and SK-VII started. The mass concentration of Gd was about 0.03 % and the neutron capture efficiency was about 75 %. From October to December 2023, some of the magnetic compensation coils were broken and the coil repair work was carried out in August 2024 as explained in the last section.

## SK-VIII

After the coil repair, the additional about 2.2 tons of  $\text{Gd}_2(\text{SO}_4)_3 \cdot \text{H}_2\text{O}$  was introduced to the detector to recover the Gd concentration. Then in September 2024, the SK-VIII period started. The mass concentration of Gd is about 0.033 %.

Phase	Period	ID PMT	Gd concentration	coverage	electronics
SK-I	1996/04 - 2001/07	11,149	0 %	40 %	ATM
SK-II	2002/10 - 2005/10	5,182	0 %	19 %	ATM
SK-III	2006/07 - 2008/08	11,129	0 %	40 %	ATM
SK-IV	2008/09 - 2018/05	11,129	0 %	40 %	QBEE
SK-V	2019/01 - 2020/06	11,129	0 %	40 %	QBEE
SK-VI	2020/07 - 2022/06	11,129	0.01 %	40 %	QBEE
SK-VII	2022/06 - 2024/09	11,129	0.03 %	40 %	QBEE
SK-VIII	2024/09 -	11,129	0.03 %	40 %	QBEE

Table 2.2: The detector performance per data acquisition period.

## 2.2 Principle of detection

### 2.2.1 Cherenkov light

Cherenkov light is emitted when a charged particle passes through a material with a refractive index  $n$  larger than 1 and moves faster than the speed of light in it. If the speed of the charged particle is  $v$  and the speed of light in a vacuum is  $c$ , Cherenkov light is emitted when the following equation holds.

$$v > \frac{c}{n} \quad (2.1)$$

Figure 2.9 shows the outline drawing of the Cherenkov light. It is emitted in a conical shape at an opening angle  $\theta_C$  with respect to the direction of movement of the charged particle. The opening angle  $\theta_C$  between the charged particle and Cherenkov light is given by

$$\cos \theta_C = \frac{1}{n\beta} \quad (2.2)$$

where  $\beta = v/c$  is the speed of the charged particle. In Super-Kamiokande, Cherenkov light is projected to the wall of the tank as a ring, and particles are identified by the shape of the ring. When the medium is water, the refractive index is  $n \simeq 1.34$ . Similarly for gadolinium water,  $n \simeq 1.34$ . If an electron produced by an interaction moves with the speed of light in the medium ( $\beta \simeq 1$ ), the opening angle is about  $42^\circ$ . From Eq. (2.2), the opening angle depends on the velocity of the charged particle. Considering Eq. (2.1), the threshold of the speed to emit Cherenkov light can be calculated. If the threshold velocity and  $\beta$  are  $v_{\text{thr}}$  and  $\beta_{\text{thr}}$ , they are written as the following equation.

$$\beta_{\text{thr}} = v_{\text{thr}} = \frac{1}{n} \quad (2.3)$$

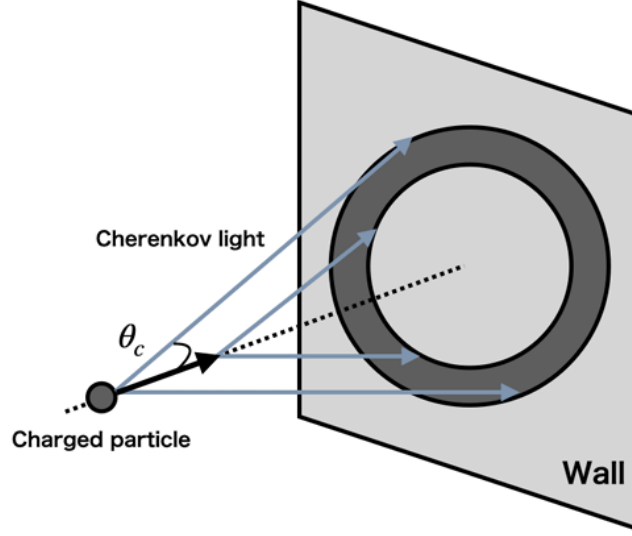


Figure 2.9: Outline drawing of Cherenkov light

The momentum threshold for Cherenkov radiation is written as the following equation and called as Cherenkov threshold.

$$p_{\text{thr}} = \frac{m}{\sqrt{n^2 - 1}} \quad (2.4)$$

Where  $m$  is the mass of the charged particle. From Eq. 2.4, the Cherenkov threshold depends on masses of particles. Table 2.3 summarizes Cherenkov thresholds for each charged particle in water.

charged particle	mass [MeV/c <sup>2</sup> ]	Cherenkov threshold [MeV/c]
$e^\pm$	0.5110	0.573
$\mu^\pm$	105.7	118.5
$\pi^\pm$	139.6	156.5
$K^\pm$	493.7	553.5
$p^\pm$	938.3	1052

Table 2.3: The summary of Cherenkov threshold in water.

The number of Cherenkov photons  $dN$  emitted by a particle with a unit charge per flight distance  $dx$  is given by

$$\frac{d^2N}{d\lambda dx} = \frac{2\pi\alpha}{\lambda^2} \left(1 - \frac{1}{n^2\beta^2}\right) \quad (2.5)$$

where  $\lambda$  is the wavelength of emitted light and  $\alpha$  is the fine structure constant ( $\simeq 1/137$ ). When an electron travels 1 cm in the PMT's sensitivity range of light wavelength 300-600 nm, the number of Cherenkov photons  $N$  is given by

$$N = \int_0^{1\text{cm}} dx \int_{300\text{nm}}^{600\text{nm}} d\lambda \frac{2\pi\alpha}{\lambda^2} \left(1 - \frac{1}{n^2\beta^2}\right) \simeq 340 \quad (2.6)$$

Gamma rays can also be detected by Compton-scattered electrons and by pair-produced electrons and positrons.

## 2.3 Data acquisition system

From SK-IV, the electronics were updated from Analog Timing Module (ATM) to QTC Based Electronics with Ethernet (QBEE) and QBEE has been used until now. In this section, the details of QBEE, the data acquisition system after SK-IV, and the software trigger are explained.

### 2.3.1 QTC Based Electronics with Ethernet (QBEE)

QBEE module consists of an Application-Specific Integrated Circuits (ASIC) with 8 QTC (high-speed charge-to-timing converter) and a TDC (Multi-hit time-to-digital converter). The diagram of QBEE is shown in Figure 2.10. One QTC can deal with

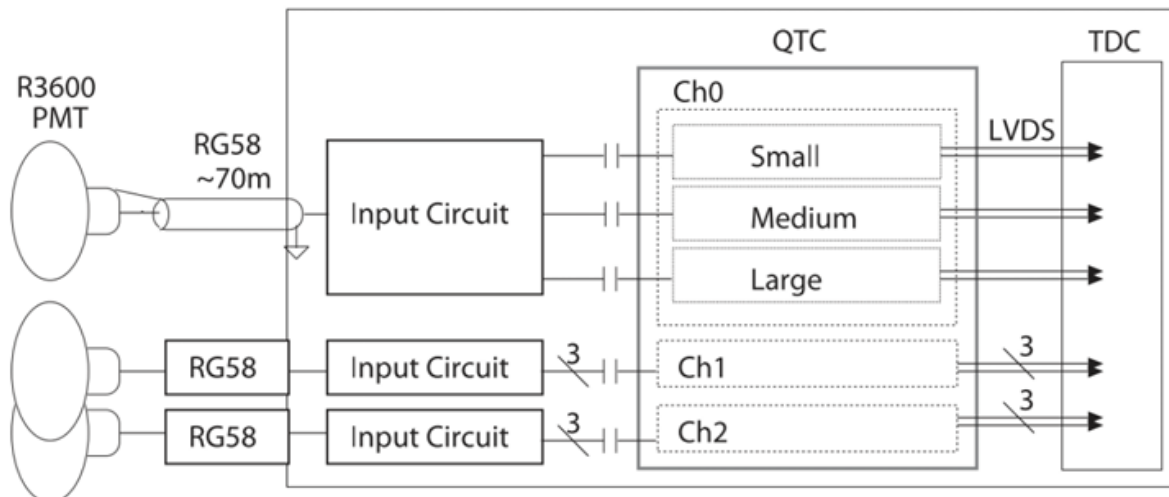


Figure 2.10: QBEE system [42].

signals from three PMTs, so each QBEE can deal with signals from 24 PMTs. QBEE can record all PMT hits. As shown in Figure 2.10, there are three gain ranges in each channel of QTC. Each gains are Small, Medium, and Large respectively, and the ratio of those gains is 1:1/7:1/49. Using those three gain ranges, the detectable charge range (dynamic range) is 0.2-2500 pC. Table 2.4 shows the relationship among gain channel, dynamic range, and charge resolution.

When the QBEE receives input from a PMT with an analog signal larger than 0.25 p.e., the QTC opens the Charge gate, Discharge gate, and VETO gate. Firstly, the Charge gate integrates the charge in the first 400 ns. Then, the Discharge gate is open during the next 350 ns, and the signals in this time window are ignored. Finally, the VETO gate is open during the next 150 ns, and the signals in this time window are also ignored. The gate opening time for one signal is 900 ns. The QTC outputs a square-wave pulse proportional to the integrated charge. Figure 2.11 shows the timing chart inside the

gain channel	dynamic range [pC]	charge resolution [pC/count]
Small	0.2 - 51	0.1 (0.04 p.e./count)
Medium	1 - 357	0.7 (0.26 p.e./count)
Large	5 - 2500	4.9 (1.8 p.e./count)

Table 2.4: The gain channels of QTC and the dynamic ranges and charge resolution of each channel [42].

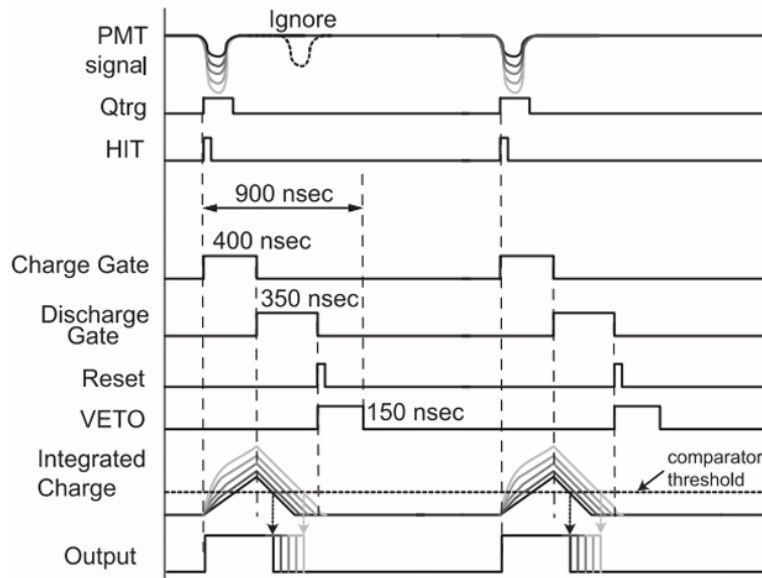


Figure 2.11: The timing chart inside the QTC [42].

QTC.

The square-wave pulses produced by QTC are sent to the TDC, and the width and rise time of the pulse are recorded. The charge resolution is about 5 % for 1 p.e. and less than 2 % for above 3 p.e.. The FPGA (Field Programmable Gate Array) deals with the recorded data. The width of the pulse is digitalized as the charge information and the rise time of the pulse is digitalized as the time information by FPGA. Each digital signal is sent to front-end PCs in the mine through the Ethernets.

### 2.3.2 DAQ

Figure 2.12 shows the diagram of the data acquisition system after SK-IV. The data

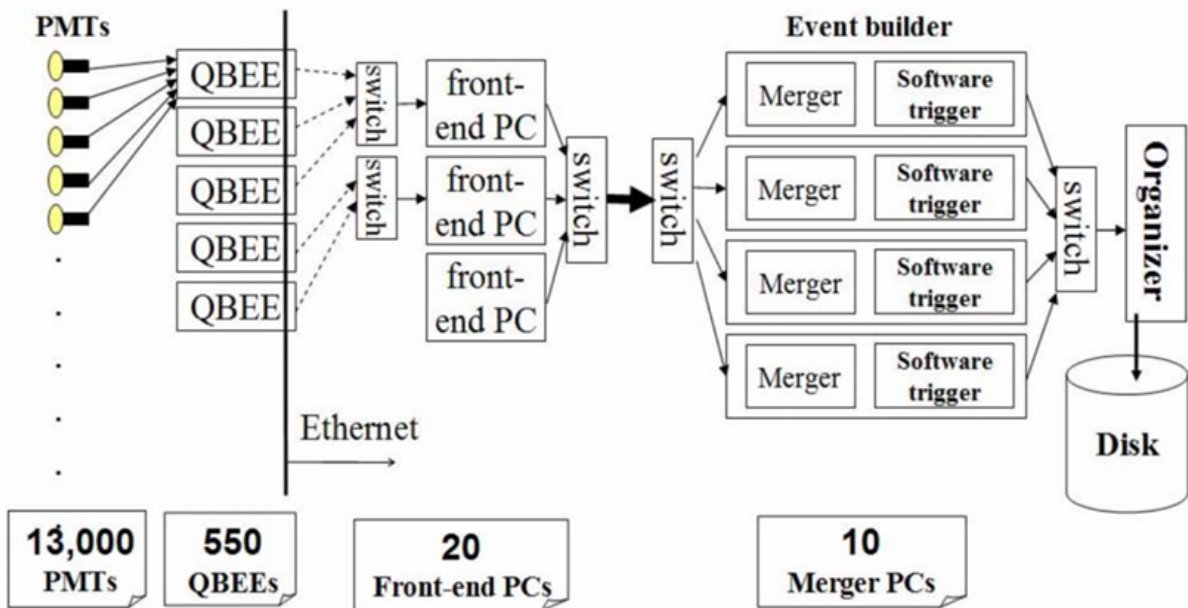


Figure 2.12: The diagram of the DAQ [43].

are sent from about 550 QBEE boards to 20 front-end PCs using TCP. One front-end PC processes the data from about 30 QBEE boards. Those processed data are sent to 10 Merger PCs. Those Merger PCs merge all of the data from the front-end PCs, and events are triggered by the software trigger. There are four energy regions, i.e. SLE (Super Low Energy), LE (Low Energy), HE (High Energy), and SHE (Super High Energy). The events are categorized into those energy regions and saved in the tree structure of ROOT [44].

### 2.3.3 Software trigger

Thanks to QBEE, signals from PMTs can be processed quickly and the Merger PCs can save all PMT hits temporarily. Software trigger counts PMT hits within 200 ns time window ( $N_{200}$ ) and events are classified as SLE, LE, HE, SHE, and OD when  $N_{200}$  exceeds a certain threshold. The thresholds and the time window of these triggers are summarized in Table 2.5. When a trigger is issued, that time is set to 0 s, and its time window is used to search related events.

There is another trigger called AFT trigger. This trigger is designed for searching

for DSNB. When the SHE trigger is issued, the AFT trigger which is the 500  $\mu\text{s}$  trigger from  $[+35, +535]$   $\mu\text{s}$  is issued following the SHE trigger. Previously, the AFT trigger was issued when the SHE trigger was issued without the OD trigger. From June 2020 (SK-VI), we changed the condition of the AFT trigger to capture the signal of neutron capture on gadolinium generated by the spallation reaction of a cosmic ray muon. The AFT trigger was also issued when the OD trigger was issued at the same time as the SHE trigger was issued. In our study of spallation neutron captures on gadolinium, the signals in the SHE and AFT triggers are used.

Trigger	$N_{200}$ threshold	time window [ $\mu\text{s}$ ]
SLE	35	$[-0.5, +1.0]$
LE	49	$[-5, +35]$
HE	52	$[-5, +35]$
SHE	60	$[-5, 35]$
OD	22	$[-5, +35]$

Table 2.5: The summary of the software triggers.

## 2.4 Super-Kamiokande with gadolinium

### 2.4.1 Gadolinium

For neutrino searches such as DSNB, it is important to improve the neutron detection efficiency. In ultrapure water without gadolinium, neutrons are captured by hydrogen, and a single 2.2 MeV gamma ray is emitted. However, this gamma-ray signal is difficult to detect because its energy is low and there are many background events. So the neutron detection efficiency was about 20 %. From July 2020, gadolinium was loaded into the detector to improve the neutron detection efficiency.

Gadolinium is a rare earth element with atomic number 64. Gadolinium has the largest thermal neutron capture cross-section among natural elements. When it captures a thermal neutron, it emits a total of about 8 MeV gamma rays. Table 2.6 shows the natural abundance ratio and the thermal neutron capture cross-sections for different isotopes of gadolinium [45].

When  $^{157}\text{Gd}$  ( $^{155}\text{Gd}$ ) captures a neutron, it becomes the excited state of  $^{158}\text{Gd}$  ( $^{156}\text{Gd}$ ). Then  $^{158}\text{Gd}$  ( $^{156}\text{Gd}$ ) emits gamma rays whose energies are 7.9 MeV for  $^{157}\text{Gd}$  and 8.4 MeV for  $^{155}\text{Gd}$  in total as it transitions to the ground state of  $^{158}\text{Gd}$  ( $^{156}\text{Gd}$ ). Figure 2.13 shows the fraction of neutron captures on Gd as a function of the mass concentration of Gd dissolved in pure water. In the 2020 Gd-loading, the mass concentration was about 0.011 % and the fraction was about 50 %. In the additional Gd-loading in 2022, the mass concentration was about 0.03 % and the fraction was about 75 %.

### 2.4.2 Ultrapure water purification system

The ultrapure water in the SK detector is produced by groundwater in the Kamioka mine. This groundwater contains some impurities such as bacteria, radioactive materials, and minerals. Those impurities are background signals of neutrino measurements in

Isotope	Natural abundance ratio [%]	Cross section [b]
<sup>152</sup> Gd	0.20	740
<sup>154</sup> Gd	2.18	85.8
<sup>155</sup> Gd	14.80	611000
<sup>156</sup> Gd	20.47	1.81
<sup>157</sup> Gd	15.65	254000
<sup>158</sup> Gd	24.84	2.22
<sup>160</sup> Gd	21.86	1.42
<sup>1</sup> H	99.99	0.33
<sup>16</sup> O	99.76	0.0002

Table 2.6: The natural abundance ratio and the thermal neutron capture cross-sections [45].

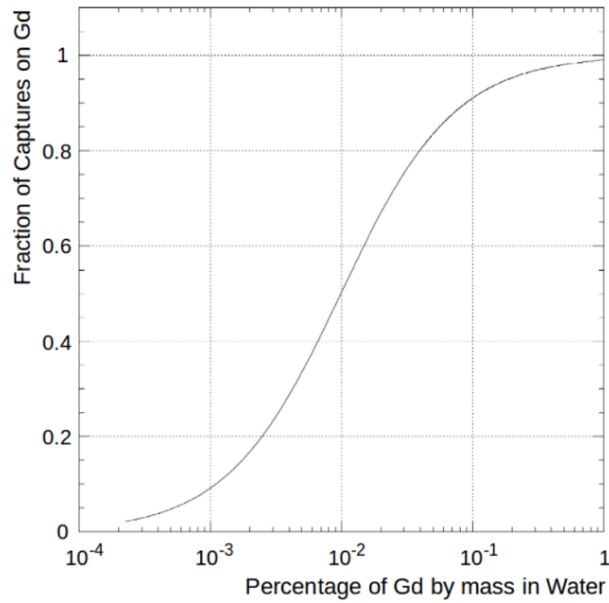


Figure 2.13: The fraction of thermal neutrons captured by gadolinium.

several MeV regions and reduce water transparency by scattering Cherenkov light. Regarding the radioactive materials, the beta decay of  $^{214}\text{Bi}$ , a progeny nuclide of  $^{222}\text{Rn}$  in the uranium series, emits electrons with a Q value of 3.26 MeV and those electrons affect seriously on the measurement in low energy region. Therefore, it is essential to remove  $^{222}\text{Rn}$ . To remove those impurities, the ultrapure water purification system was developed. This system was used before SK-V. The main pieces of equipment are explained in the following, and Figure 2.14 shows the overview of this system.

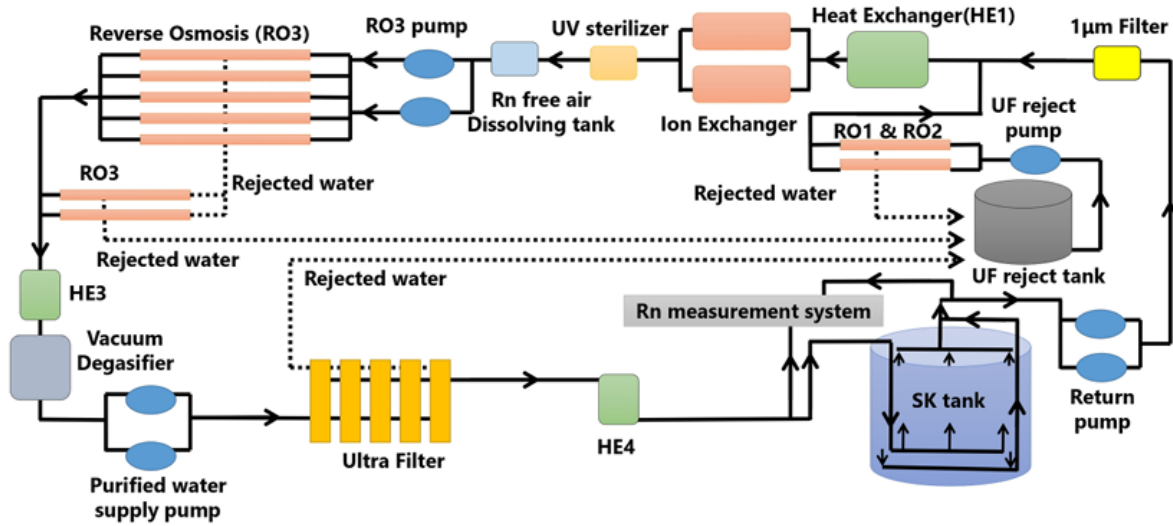


Figure 2.14: The overview of the ultrapure water purification system [41].

- 1  $\mu\text{m}$  mesh filter  
This filter removes impurities larger than 1  $\mu\text{m}$ .
- Heat exchanger  
The temperature of ultrapure water in the detector rises due to the generation of heat by water circulation pumps and PMTs. To prevent increasing dark noise and multiplying bacteria due to increasing the temperature of the water, the heat exchangers exchange heat and keep the water temperature at about 13  $^{\circ}\text{C}$ . During one water cycle, there are three heat exchangers.
- Ion exchanger  
The ion exchanger consists of a cation exchange resin and an anion exchange resin and removes some cations such as  $\text{Zn}^+$ ,  $\text{Cd}^+$ ,  $\text{Fe}^{2+}$  and some anions such as  $\text{CO}_3^-$  which are dissolved in water. It can be checked by measuring the specific resistance of water whether those ions are removed properly. When the ion concentration in water is 0, the specific resistance of water is 18.24  $\text{M}\Omega\cdot\text{cm}$ . Using this ion exchanger, the specific resistance of ultrapure water keeps at above 18.2  $\text{M}\Omega\cdot\text{cm}$ .
- UV sterilizer  
This system sterilizes bacteria by irradiating UV with 253.7 nm wavelength.

- Radon-free air dissolving system  
To improve radon removal efficiency in the vacuum degasifier, which is explained in the following, the air without radon is dissolved in water.
- Reverse osmosis filter  
This filter removes organic matter whose molecular weight is larger than 1,000.
- Vacuum degasifier  
This vacuum degasifier removes gases that are dissolved in water. It removes about 96 % of radon gas and about 99 % of oxygen gas.
- Ultra filter (UF)  
This filter removes fine particles which are larger than 10 nm.
- Membrane degasifier  
This membrane degasifier removes radon gas which remains in water.

The ultrapure water purified by the above process was circulated continuously through the purification system at a flow rate of 60 tons/hour to maintain the water quality inside the detector. The  $^{222}\text{Rn}$  concentration is reduced to  $1.7 \text{ mBq/m}^3$  by this purification system [41].

### 2.4.3 Radon-free air production system

In the Kamioka mine, because the rock contains a lot of  $^{238}\text{U}$  and  $^{222}\text{Rn}$  gas is emitted, the  $^{222}\text{Rn}$  concentration in the air is more than 100 times higher than that of the air above ground. When radon gas dissolves in water, it causes background signals in low-energy regions. Therefore, radon concentration must be kept as low as possible to prevent it from dissolving in water. So the system shown in Figure 2.15 is used in Super-Kamiokande. This system removes radon from the air in the mine and lets this radon-free air into the detector, the buffer tank, and the laboratory. The main equipments of this system are explained in the following.

- Compressor  
This compressor compresses the air to 7.5-8 atm.
- Air filter  
This filter removes dust in the compressed air. There are three air filters and  $0.3 \mu\text{m}$ ,  $0.1 \mu\text{m}$ , and  $0.01 \mu\text{m}$  filters are installed respectively.
- Air drier  
This drier removes moisture from the air to improve radon removal efficiency.

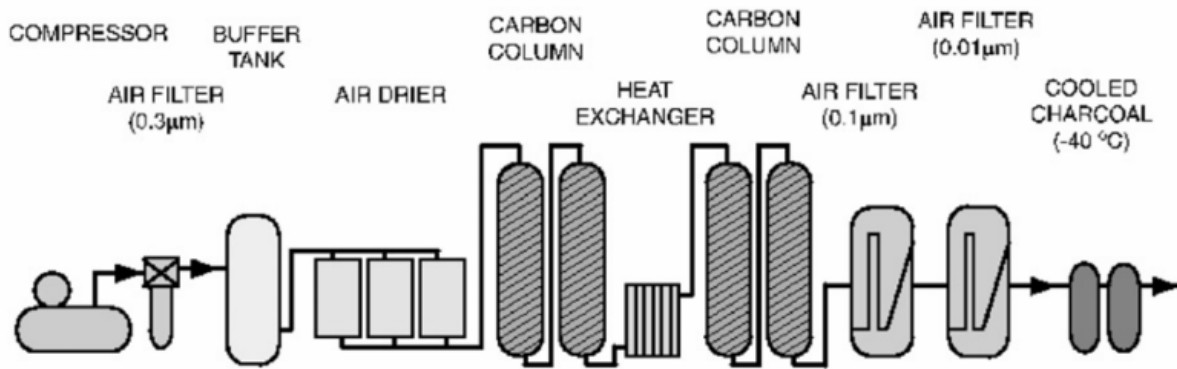


Figure 2.15: The schematic drawing of the radon-free air dissolving system [36].

- Carbon column  
This removes radon from the air using activated carbons which absorb radon.
- Cooled charcoal  
Same as the carbon column, this device also removes radon using activated carbons. Those carbons are cooled to  $-60\text{ }^{\circ}\text{C}$  and the radon absorption rate is about 100 %.

Radon-free air produced by the above process is let into the tank. The air outside the mine is let into the laboratory at the rate  $70\text{ m}^3/\text{min}$  and the radon concentration is kept at about  $50\text{ Bq}/\text{m}^3$ .

#### 2.4.4 Gadolinium sulfate solution system

After the end of the SK-IV period, a new water circulation system was developed. This new system made it possible to purify and circulate the ultrapure water, and dissolve gadolinium in the ultrapure water. To dissolve gadolinium in ultrapure water,  $\text{Gd}_2(\text{SO}_4)_3 \cdot 8\text{H}_2\text{O}$  was used because gadolinium itself is insoluble in water. The conventional water purification system has ion-exchange resins, where ions are removed. However, in SK-Gd, it is necessary to circulate water while retaining gadolinium ions ( $\text{Gd}^{3+}$ ) and sulfate ions ( $\text{SO}_4^{2-}$ ). Therefore, a new circulation and purification system was developed to remove ions other than gadolinium and sulfate ions. The overview of this system is shown in Figure 2.16. The main steps are explained below.

#### Gd dissolving system

The Gd dissolving system consists of the following pieces of equipment.

- Weighing hopper  
The  $\text{Gd}_2(\text{SO}_4)_3 \cdot 8\text{H}_2\text{O}$  powder is weighed.
- Circle feeder  
The  $\text{Gd}_2(\text{SO}_4)_3 \cdot 8\text{H}_2\text{O}$  powder is delivered in regulated quantities via the circle feeder.

- Solvent tank  
A fraction of the SK water being continuously recirculated is stored.
- Shear blender and dissolving tank  
 $\text{Gd}_2(\text{SO}_4)_3 \cdot 8\text{H}_2\text{O}$  powder is dissolved in water from the solvent tank.
- Solution tank  
The resulting solution is stored.

### **Pre-treatment system**

In this process, impurities such as ions other than Gd ion and sulfate ion, bacteria, and dust are removed.

- 1  $\mu\text{m}$  filter  
This filter is the same as the filter in Section 2.4.2.
- UV total organic carbon reduction lamp (TOC lamp)  
Organic matters are oxidized and decomposed by UV with 184.9 nm wavelength. Bacteria are sterilized by UV at 253.7 nm.
- Strongly acidic cation exchange resin (C-Ex resin)  
Cations other than  $\text{Gd}^{3+}$  are removed. This resin contains  $\text{Gd}^{3+}$  ions not to remove this ion.
- Strongly basic anion exchange resin (A-Ex resin)  
Anions other than  $\text{SO}_4^{2-}$  are removed. This resin contains  $\text{SO}_4^{2-}$  not to remove this ion.
- UV sterilizer  
Bacteria in the Gd solution are sterilized by UV at 253.7 nm.
- 0.2  $\mu\text{m}$  filter  
This filter removes fine particles which are smaller than 1  $\mu\text{m}$ .

### **Gd solution purification and circulation system**

This system purifies and circulates gadolinium sulfate solution, which is delivered from the Gd dissolving system and the pre-treatment system, keeping  $\text{Gd}^{3+}$  and  $\text{SO}_4^{2-}$  concentration constant.

- Return water filter  
This filter removes impurities larger than 1  $\mu\text{m}$ .

- 1st buffer tank  
This tank received Gd solution from the pre-treatment system and return water from the circulation system and kept gadolinium concentration at 0.01 %. There were two systems where water flowed at 60 m<sup>3</sup>/h after this tank.
  
- TOC lamp  
This is the same as in the pre-treatment system.
  
- Heat exchanger (HE)  
This is the same as in the ultrapure water purification system in Section 2.4.2.
  
- C-Ex resin  
This is the same as in the pre-treatment system.
  
- A-Ex resin  
This is the same as in the pre-treatment system.
  
- 1 μm filter  
This is the same as in the pre-treatment system.
  
- UV sterilizer  
This is the same as in the pre-treatment system.
  
- Ultra filter modules  
This filter removes particles smaller than 1 μm.
  
- 2nd buffer tank  
Two systems where water flowed at 60 m<sup>3</sup>/h joined together in this tank.
  
- Temperature control units  
These units can control the water temperature with 0.01 [°C] accuracy.
  
- Membrane degasifier  
This is the same as in the ultrapure water purification system in Section 2.4.2.

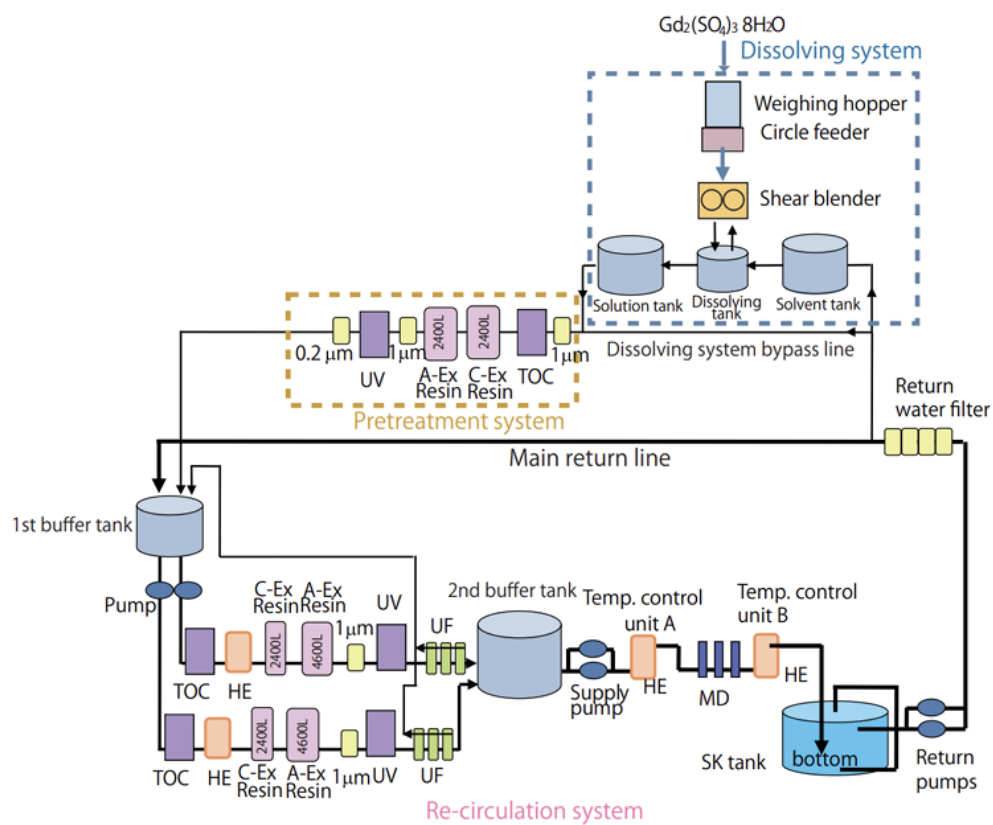


Figure 2.16: Schematic diagram of SK-Gd water system [45].

# Chapter 3

## Energy calibration and reconstruction

Super-Kamiokande conducts detector calibrations regularly and determines parameters to correct the data obtained. Detector calibration also determines parameters that allow Monte Carlo simulations (MC) to reproduce events occurring inside the detector. Regarding  $\mathcal{O}(1-10)$  MeV events, the Cherenkov photons emitted from those events are a few dozen and the energies of those events are reconstructed by the number of photons detected. Therefore, it is essential to calibrate the response of the ID PMTs and photon transport in the water.

In this section, the calibration of the ID and the energy calibration of  $\mathcal{O}(1-10)$  MeV events are described.

### 3.1 Inner detector related calibration

The processes for calibrating the ID are as follows: Firstly, the gain and quantum efficiency of each PMT are measured. Then, the time response of each PMT is calibrated. The processing time of electrical circuits, the difference in cable length, and the difference in the time response of the PMTs due to the wave height of PMT signals are corrected.

#### 3.1.1 Measurement of relative gain

The gain of PMT is defined as the amplification rate of photoelectrons that reach the PMT dynode. To determine the gain of each PMT, it is necessary to measure the average gain of all PMTs and the relative gain of each PMT. The relative gain is the difference between the average gain and each gain. In this section, the relative gain is explained.

To measure the relative gain, an isotropic light source composed of  $N_2$  dye laser is used. There are 2 steps in this measurement. Firstly, high-intensity light is injected so that all PMTs can detect sufficient light. The average charge that each PMT detects is defined as  $Q_{\text{obs}}(i)$  where  $i$  represents the  $i$ -th PMT. Then, low-intensity light is injected. In this step, a few PMTs detect the light, and the signal of 1 p.e. is measured. The number of detections in which  $i$ -th PMT detected charge above the threshold is defined

as  $N_{\text{obs}}(i)$  in this measurement.  $Q_{\text{obs}}(i)$  and  $N_{\text{obs}}(i)$  are calculated as follows.

$$Q_{\text{obs}}(i) \propto I_H \times a(i) \times \epsilon(i) \times G(i) \quad (3.1)$$

$$N_{\text{obs}}(i) \propto I_L \times a(i) \times \epsilon(i) \quad (3.2)$$

where  $I_H$  ( $I_L$ ) is the average light intensity of high-intensity (low-intensity) light,  $a(i)$  is the acceptance of  $i$ -th PMT,  $\epsilon(i)$  is the quantum efficiency of  $i$ -th PMT, and  $G(i)$  is the gain of  $i$ -th PMT. The gain of each PMT ( $G(i)$ ) can be obtained from the ratio  $Q_{\text{obs}}$  to  $N_{\text{obs}}$ .

$$G(i) \propto \frac{Q_{\text{obs}}(i)}{N_{\text{obs}}(i)} \quad (3.3)$$

The relative gain of each PMT is obtained by normalizing Eq. (3.3) by the average gain of all PMTs. The term of  $I_H/I_L$  is canceled by this normalization. Figure 3.1 shows the distribution of relative gain for SK-V analysis. In this analysis, the PMTs were grouped based on their position relative to the light source and the signals are weighted according to this grouping. This relative gain of each PMT is used as a correction factor when converting the output charge to the number of photoelectrons.

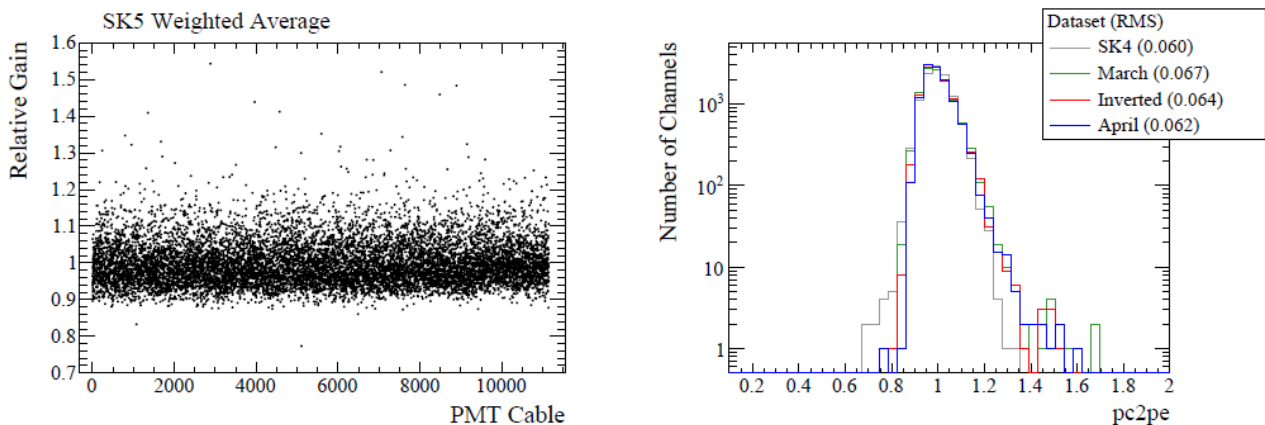


Figure 3.1: The distribution of the relative gain of each PMT (left) and projection onto the vertical axis for all data sets (right) in SK-V. In the right figure, each colored line represents the measurement period.

### 3.1.2 Measurement of absolute gain

The absolute gain is a coefficient used to convert obtained charge [pC] to photoelectrons [p.e.]. The value of the absolute gain is determined by the charge distribution of 1 p.e. signal. For this measurement, a Ni-Cf source is used. This source emits about 9 MeV  $\gamma$  rays isotropically. If it is installed at the center of the detector, more than 99 % of signals are 1 p.e. signals.

#### Ni-Cf source

The Ni-Cf source consists of  $^{252}\text{Cf}$  source, a 16 cm diameter ball (Ni ball) which is composed of 65 % nickel oxide ( $\text{NiO}_2$ ) and 35 % polyethylene resin, and brass rod. The  $^{252}\text{Cf}$

source is attached to the rod and the rod is inserted into a hole through the center of the Ni ball. Figure 3.2 shows the diagram of the Ni-Cf source and the emission of  $\gamma$  ray.  $^{252}\text{Cf}$  has a half-life of 2.65 years, 96.9 % undergo  $\alpha$  decay and the remaining 3.1 % undergo spontaneous fission. In this measurement, neutrons produced via spontaneous fission are important. The generated neutrons are elastically scattered with the protons in the Ni ball in a few  $\mu\text{s}$ . Then, the neutrons lose their energy and are eventually thermalized. These thermalized neutrons are captured by nickel and about 9 MeV  $\gamma$  rays are emitted. These generated  $\gamma$  rays cause electron-positron pair production and Compton scattering

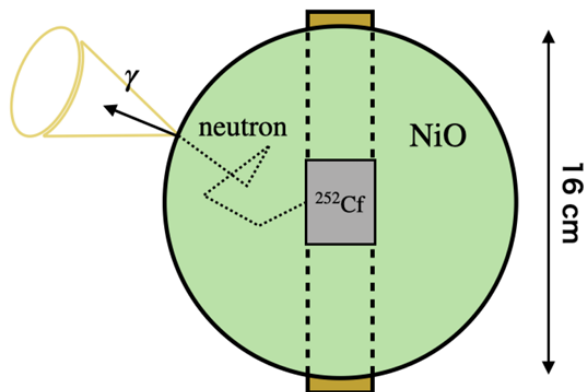


Figure 3.2: The diagram of Ni-Cf source and the emission of  $\gamma$  ray.

in the water, resulting in the emission of Cherenkov light. Only a few dozen PMTs detect these Cherenkov lights, so the detected signals are expected to be 1 p.e. signals. Because the Ni-Cf source is spherical, the Cherenkov light is emitted isotropically.

Figure 3.3 the charge distribution of 1 p.e. signal using Ni-Cf source in SK-III. In this figure, the relative gain (Section 3.1.1) was corrected and all signals of PMTs were summed up. The dark noise of PMTs was reduced by making distributions in a time window without Ni-Cf signals (off-time) and with Ni-Cf signals (on-time) respectively and subtracting the off-time distribution from the on-time distribution. The largest peak near 0 represents photoelectrons which were not multiplied at the first dynode, and the peak around 3 pC represents the 1 p.e. signals. The absolute gain is defined as the average value of overall this distribution.

Table 3.1 shows the value of the absolute gain in each SK phase. Because the high voltages are not adjusted after SK-V, the values after SK-V are the same.

SK phase	SK-I	SK-II	SK-III	SK-IV	SK-V to SK-VIII
Absolute gain [pC/p.e.]	2.055	2.297	2.243	2.658	2.460

Table 3.1: The value of the absolute gain in each SK phase [39].

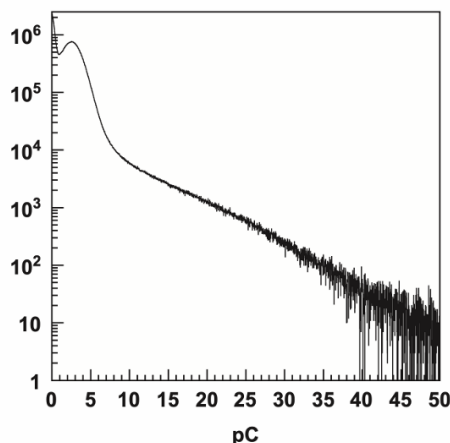


Figure 3.3: The charge distribution using Ni-Cf source in SK-III [39].

### 3.1.3 Measurement of relative quantum efficiency

The relative QE is used to reconstruct the energy of events in the low-energy region. The Ni-Cf source is also used to calculate the relative QE. From Eq. (3.2), PMT hits are proportional to the quantum efficiency in low-energy regions. Hence, the relative QE of each PMT can be calculated by comparing the MC simulation with the real data. In the MC simulation, the relative QE of each PMT is set to 1. The hit rate for the real data and MC is calculated. The relative QE of each PMT is the ratio of the hit rate for the real data to that for MC.

$$R_{\text{QE}}(i) = \frac{R_{\text{data}}(i)}{R_{\text{MC}}(i)} \quad (3.4)$$

Where  $R_{\text{QE}}(i)$  is the relative of  $i$ -th PMT,  $R_{\text{data}}(i)$  is the hit rate for the real data, and  $R_{\text{MC}}(i)$  is the hit rate for the MC simulation. Figure 3.4 shows the relative QE distribution for the SK-IV data. The black histogram represents the relative QE of all PMTs and the colored histograms are split by year of manufacture of PMTs. A table that summarizes this relative QE of each PMT is called a "QE table". This table is used to reproduce the PMT response in MC.

### 3.1.4 Measurement of hit collection efficiency

After the magnetic compensation coil failure in October 2023 (Section 2.1.3), the collection efficiency (CE) of each PMT is changed. To correct this difference in the CE, the data in all coils on phase and that in the coil failure phase is compared. The Ni-Cf source data in each phase are used for this correction. Like Eq. (3.2), the number of PMT hits also depends on the collection efficiency.

$$N(i) \propto a(i) \times \epsilon(i) \times CE(i) \quad (3.5)$$

where  $CE(i)$  is the collection efficiency of  $i$ -th PMT.  $\epsilon(i)$  is not thought to be affected by the coil failure. Therefore, the relative CE is defined as the ratio of the hit rate in all coils on phase to that in the coil failure phase.

$$R_{\text{CE}}(i) = \frac{R_{\text{coiloff}}(i)}{R_{\text{coilon}}(i)} \quad (3.6)$$

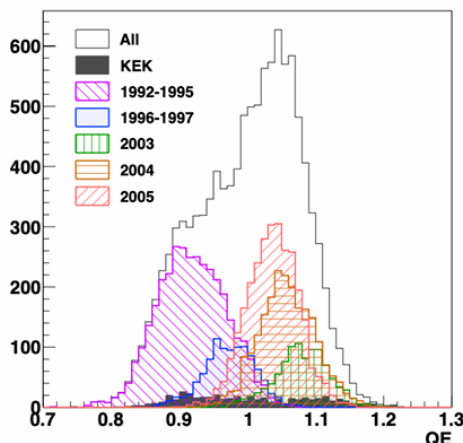


Figure 3.4: The distribution of relative QE [46]. Each colored histogram represents the year of manufacture of each PMT as in the figure.

Where  $R_{CE}(i)$  is the relative CE of  $i$ -th PMT,  $R_{coilon}(i)$  is the hit rate of  $i$ -th PMT in all coils on phase, and  $R_{coiloff}(i)$  is the hit rate of  $i$ -th PMT in the coil failure phase. In this analysis, the Ni-Cf source is also used and the SK state is assumed to be the same when all coils are on and the coil failure phase. Figure 3.5 shows the relative CE of each PMT. From this figure, the PMTs in the position where the coils were broken have low relative CE. These results are summarized in a table called a "CE table".

### 3.1.5 Calibration of time response

Each PMT's time response shifts due to the PMT performance difference, the length of the cable, the process in the electrical circuit, and the wave height. Correcting this effect is also important for the position and direction reconstruction of events.

Figure 3.6 shows the diagram of the equipment for the calibration of the time response. In this measurement, a light source of nitrogen laser (USHO laser) is used. This laser is monochromatic and emits pulsed light with 337 nm wavelength and 0,4 ns full width at half maximum (FWHM). The generation time of the pulse is determined by the 2-inch PMT (monitor PMT). Then the wavelength is converted to 398 nm, at which the quantum efficiency of PMT is large. This converted light is diffused isotropically by the diffuser ball. By changing the intensity of light using the light filters, the time response for various wave heights can be measured. The wave height is proportional to the charge, so this calibration is called TQ calibration.

The calibration of time response is based on the two-dimensional distribution of the time and charge (wave height). This distribution is called the "TQ map" and Figure 3.7 shows the typical TQ map. The TOF (Time of Flight) is calculated by the distance between the light source and the PMT, Then, using the observed time  $T_{obs}$  and the time of the monitor PMT  $T_{monitor}$ , the hit time  $T$  (the vertical axis in Figure 3.7) is calculated by  $T_{obs} - TOF - T_{monitor}$ . The peak of each QBin is determined, and these peaks are fitted with the following polynomials. From these fitting functions, a total of 15 correction

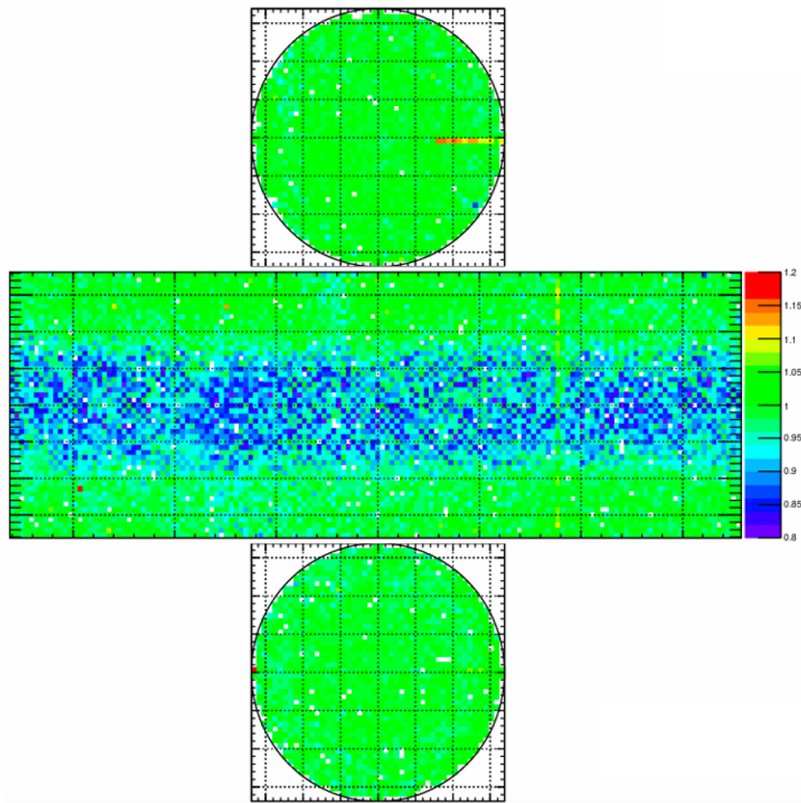


Figure 3.5: The relative CE of each PMT [47].

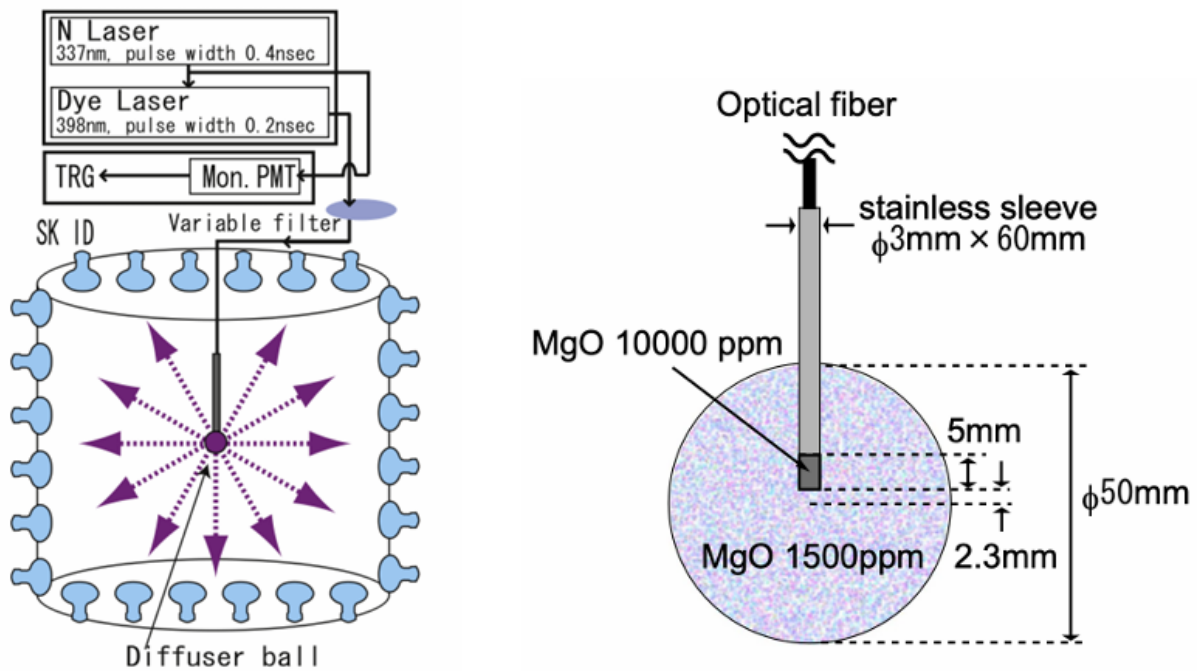


Figure 3.6: The diagram of TQ calibration (left) and the cross-section of the diffuser ball (right) [39].

coefficients are determined.

$$\text{pol}N(x) \equiv p_0 + p_1x + p_2x^2 + \dots + p_Nx^N \quad (3.7)$$

$$\text{QBin} \leq 10 : F_1(x) \equiv \text{pol}3(x) \quad (3.8)$$

$$\text{QBin} \leq 50 : F_2(x) \equiv F_1(10) + (x - 10)[F_1'(10) + (x - 10)\text{pol}3(x - 10)] \quad (3.9)$$

$$\text{QBin} > 50 : F_3(x) \equiv F_2(50) + (x - 50)\text{pol}6(x - 50) \quad (3.10)$$

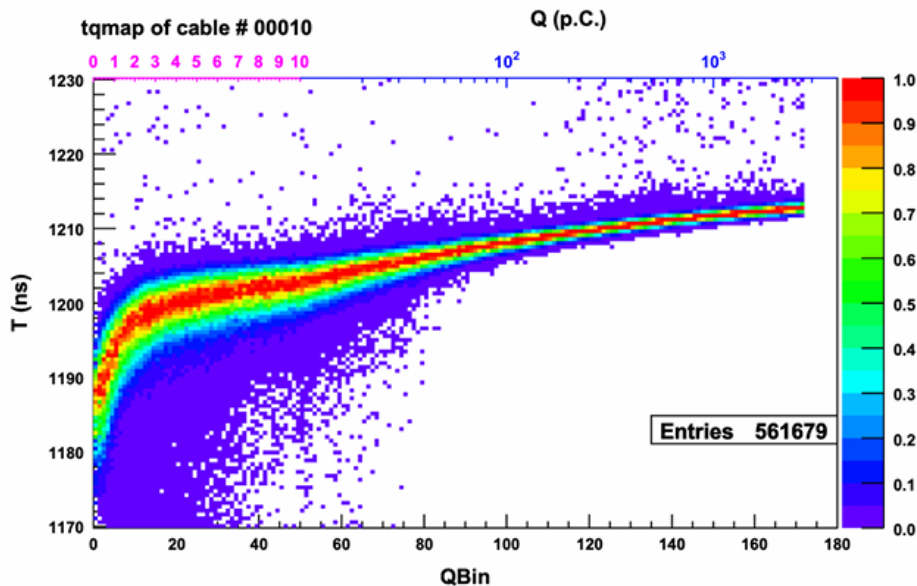


Figure 3.7: The relationship between the charge and hit time in one PMT [39].

## 3.2 Water related calibration

Water transparency is an important parameter for reconstructing the energy of an event precisely. The water transparency is measured with a laser and decay electrons from cosmic ray muon. In this section, these two methods are discussed and the Top-Bottom asymmetry is explained.

### 3.2.1 Measurement of the water transparency with a laser

The intensity of light decreases exponentially as the following equation.

$$I(\lambda) = I_0(\lambda) \exp\left(-\frac{r}{L(\lambda)}\right) \quad (3.11)$$

where  $\lambda$  is the wavelength of the light,  $I_0(\lambda)$  is the initial value of the intensity,  $r$  is the length of flight, and  $L(\lambda)$  is the attenuation length of water. When light passes through the water, it is affected by the effect of absorption and scattering. For the scattering effect, there are symmetric scattering and asymmetric scattering (Figure 3.8).

The symmetric scattering consists of Rayleigh scattering, and the asymmetric scattering consists of forward Mie scattering. Considering this scattering effect, the attenuation length of water is defined as the following equation in MC.

$$L(\lambda) = \frac{1}{\alpha_{\text{abs}}(\lambda) + \alpha_{\text{sca,sym}}(\lambda) + \alpha_{\text{sca,asy}}(\lambda)} \quad (3.12)$$

Where  $\alpha_{\text{abs}}(\lambda)$ ,  $\alpha_{\text{sca,sym}}(\lambda)$ ,  $\alpha_{\text{sca,asy}}(\lambda)$  are parameters for absorption, symmetric scattering, and asymmetric scattering, respectively. These parameters are measured using a laser.

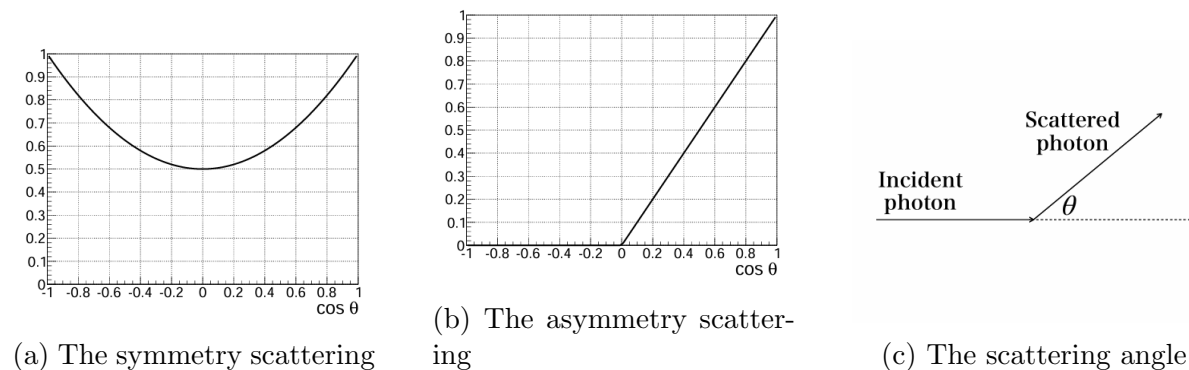


Figure 3.8: The scattering effect [57].

To measure these absorption and scattering parameters, light with 337 nm wavelength is injected by  $N_2$  laser, and lights with 375 nm, 405 nm, 445 nm, and 473 nm wavelength are injected by a laser diode. The barrel region of the detector is divided into 5 areas as Figure 3.9 and the hit rate of PMTs in each area and the top of the detector is measured. As in Figure 3.9, the laser is injected from the top of the detector and the scattering photons are detected by the PMTs. The parameters in Eq. (3.12) are determined by this measurement. Figure 3.10 shows the hit rate of PMTs at the top of the detector and in each area for the data and MC. The horizontal axis in Figure 3.10 shows the PMT hit time after subtracting the TOF. In Figure 3.10, there are two regions between the blue lines. The left one is due to the scattering photons. By measuring the signals of these scattering photons, the attenuation coefficient is determined. The peak in the right region is thought to be due to the reflected photons by the PMT or black sheet.

The parameters  $\alpha_{\text{abs}}(\lambda)$ ,  $\alpha_{\text{sca,sym}}(\lambda)$ , and  $\alpha_{\text{sca,asy}}(\lambda)$  are calculated as follows.

$$\alpha_{\text{abs}}(\lambda) = P_0 \times \frac{P_1}{\lambda^4} + P_0 \times P_2 \times 0.0279 \times \left(\frac{\lambda}{500}\right)^{P_3} \quad (3.13)$$

$$\alpha_{\text{sca,sym}} = \frac{P_4}{\lambda^4} \times \left(1.0 + \frac{P_5}{\lambda^2}\right) \quad (3.14)$$

$$\alpha_{\text{sca,asy}} = P_6 \times \left(1.0 + \frac{P_7}{\lambda^4} \times (\lambda - P_8)^2\right) \quad (3.15)$$

These nine parameters  $P_0$  to  $P_8$  are determined when the  $\chi^2$  is the minimum of comparing the hit time distribution of MC with data. The values of these parameters in SK-VI and SK-VII are summarized in Table 3.2.

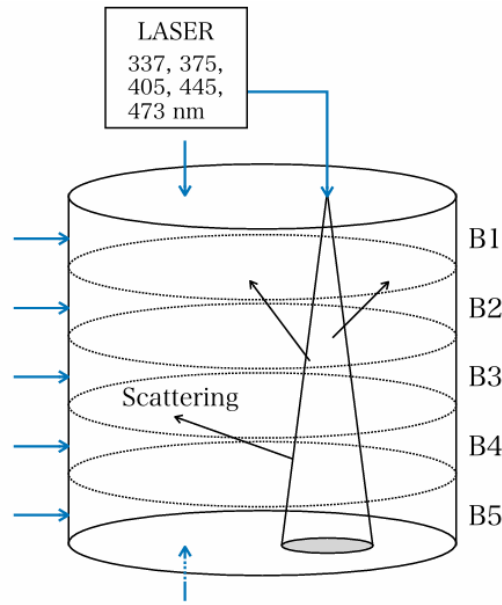


Figure 3.9: The diagram of the measurement of the water transparency [39]. The PMTs are divided into 6 areas, the top of the detector, B1, B2, B3, B4, and B5.

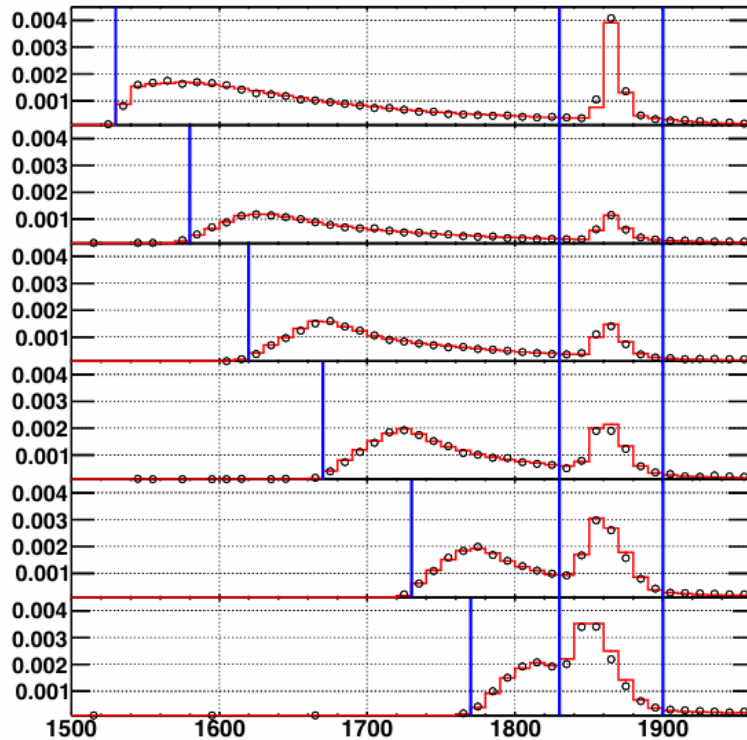


Figure 3.10: The hit time distribution of data and MC using the 405 nm wavelength laser [39]. From the top, each histogram represents the top of the tank, B1, B2, B3, B4, and B5 in Figure 3.9. The black line represents the data and the red line represents the MC.

	SK-VI	SK-VII
$P_0$	0.5966	0.6348
$P_1$	$5.189 \times 10^7$	$8.772 \times 10^7$
$P_2$	1.065	0.9245
$P_3$	14.19	16.97
$P_4$	$1.138 \times 10^8$	$9.321 \times 10^7$
$P_5$	$5.791 \times 10^4$	$9.595 \times 10^4$
$P_6$	$2.262 \times 10^{-4}$	$8.268 \times 10^{-4}$
$P_7$	17.13	156.2
$P_8$	$4.486 \times 10^4$	$8.664 \times 10^3$

Table 3.2: The summary of the parameters  $P_0$  to  $P_8$  for SK-VI and SK-VII

### 3.2.2 Measurement of water transparency with decay electrons

The average water transparency throughout the detector is measured using the decay electrons from cosmic ray muons in the detector. This measurement can monitor the time variation of the water. The decay electrons event selections are below.

- The time difference  $\Delta t$  between the arrival time of the muon and the generation time of the decay electron candidate is  $3.0 \mu\text{s} \leq \Delta t \leq 8.0 \mu\text{s}$ .
- The reconstructed position of the decay electron candidate is within the fiducial volume of the detector.
- The distance between the muon stopping point and the decay electron generation point is within 250 cm.

For the second condition, the fiducial volume is the volume more than 2 m away from the inner wall of the ID. After this selection, the distance  $r$  between the PMT that detected the Cherenkov light emitted from the decay electrons and the reconstructed position of the decay electron is calculated. Then, the relationship between distance  $r$  and the detected charge is plotted and this plot is fitted with the exponential function to derive the water transparency called "WT<sub>decay-e</sub>" (Figure 3.11). Figure 3.12 shows the time variation of the WT<sub>decay-e</sub> from SK-VI to SK-VII before the coil failure. The scale factor  $C_{\text{abs}}$  is defined to reproduce this time variation of WT<sub>decay-e</sub>. The absorption parameter  $\alpha_{\text{abs}}(\lambda)$  in Eq. (3.13) is multiplied by this factor.  $C_{\text{abs}}$  is determined as follows. Firstly, decay electrons in MC are generated at different settings of  $C_{\text{abs}}$ . Then, the correlation between the WT<sub>decay-e</sub> and  $C_{\text{abs}}$  is plotted and fitted with the following function.

$$C_{\text{abs}} = p_0 + \frac{p_1}{\text{WT}_{\text{decay-e}}} \quad (3.16)$$

Where  $p_0$  and  $p_1$  are fit parameters. For SK-VI, they are -1.187 and 27840, respectively. For SK-VII, they are -0.664 and 22170, respectively. Figure 3.13 shows the correlation plot between  $C_{\text{abs}}$  and the water transparency.

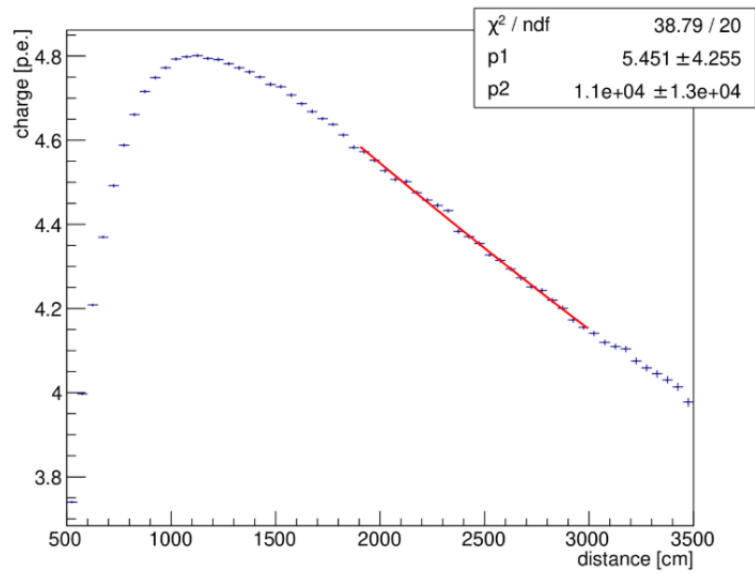


Figure 3.11: The charge vs distance  $r$  plot.

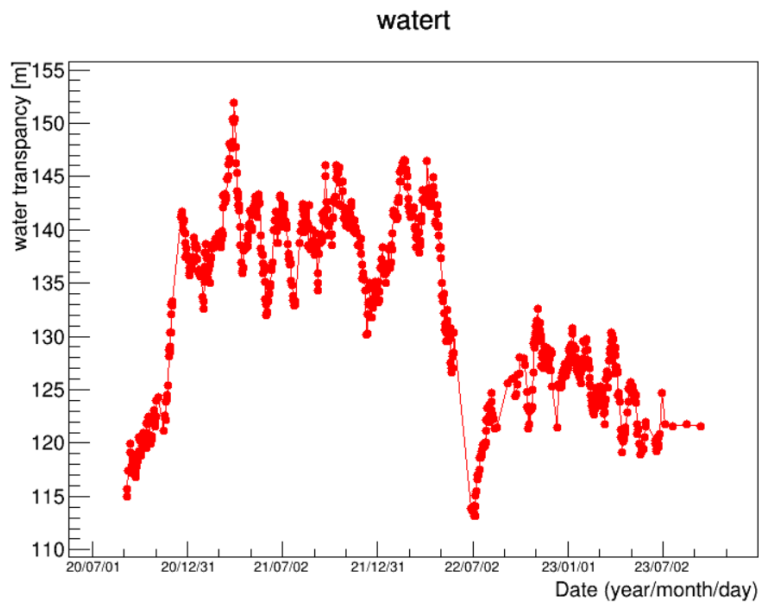


Figure 3.12: The time variation of the water transparency.

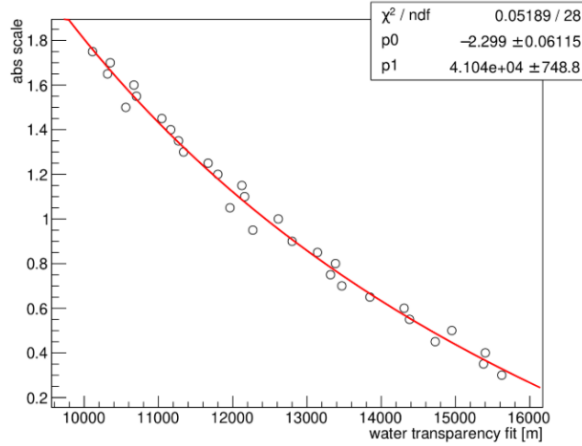


Figure 3.13: The correlation plot between  $C_{\text{abs}}$  and the  $WT_{\text{decay-e}}$ .

### 3.2.3 Top-bottom asymmetry

In SK, the water is injected into the tank from the bottom and extracted from the top. The water is convected at the bottom and the temperature is stable, while the water is not convected above a certain height and the temperature increases with the height. The variations of the water flow are monitored using the water temperature. The water transparency difference is called Top-bottom asymmetry (TBA). This asymmetry should be reproduced in MC. The TBA is measured by both the Xe isotropic light source and the Ni-Cf source. The TBA of the water  $\alpha_{\text{TBA}}$  is expressed as follows.

$$\alpha_{\text{TBA}} = \frac{\langle N_{\text{top}} \rangle - \langle N_{\text{bottom}} \rangle}{\langle N_{\text{barrel}} \rangle} \quad (3.17)$$

Where  $\langle N_{\text{top}} \rangle$ ,  $\langle N_{\text{bottom}} \rangle$ , and  $\langle N_{\text{barrel}} \rangle$  represent the average PMT hit at the top, bottom, and barrel of the detector, respectively. Figure 3.14 shows the time variation of  $\alpha_{\text{TBA}}$  is SK-IV [33]. This time variation is mainly due to the time variation of absorption. Therefore, the  $z$ -dependence of the water transparency is considered by multiplying the factor  $A(z, t)$  to the  $\alpha_{\text{abs}}$  in Eq. (3.13). The factor  $A(z, t)$  is defined as follows.

$$A(z) \equiv \begin{cases} 1 + z \cdot \beta & (z \geq z_i \text{m}) \\ 1 - z_i \cdot \beta & (z < z_i \text{m}) \end{cases} \quad (3.18)$$

For SK-VI,  $z_i$  is -11 m. For SK-VII,  $z_i$  is -15 m.  $z_i$  was determined by the water temperature distribution in the tank. The value of  $\beta$  is calculated by comparing the data of the Ni-Cf source with MC generated by changing  $\beta$ . Then,  $\beta$  is expressed as follows.

$$\beta = 0.01 \times (\text{slope} \times 100 \times \text{TBA} - \text{intercept}) \quad (3.19)$$

For SK-VI, slope and intercept in Eq. (3.18) are -0.006322 and -0.004130, respectively. For SK-VII, they are -0.006729 and -0.007502, respectively. This equation is used for the detector MC and reconstruction of the energy.

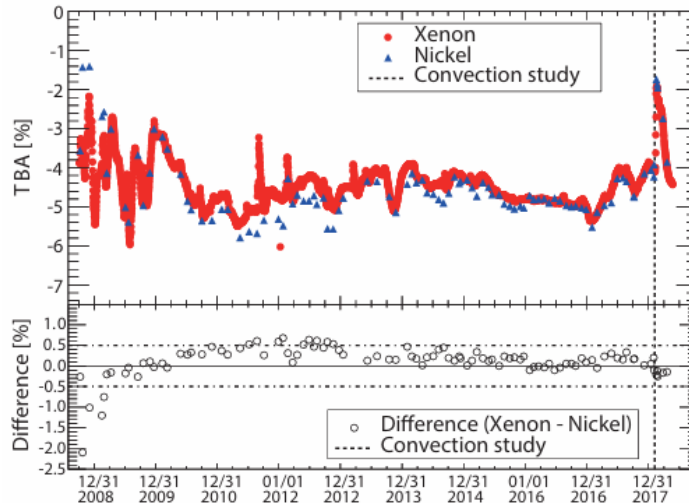


Figure 3.14: Top: The time variation of the top-bottom asymmetry (TBA) throughout SK-IV. [36]. The red dots represent the Xe light source data and the blue dots represent the Ni-Cf source data. Bottom: The difference between two TBA measurements.

### 3.3 Event reconstruction

In the low-energy region, a reconstruction program called BONSAI (Branch Optimization Navigating Successive Annealing Interactions) is used to reconstruct the position and direction of an event. The energy of an event is reconstructed by the BONSAI result and the number of PMT hits. In this section, the reconstruction method for low-energy events in the SK is described.

#### 3.3.1 Vertex reconstruction

In the SK low-energy region, the trajectory of a charged particle can be assumed to be a point compared to the vertex resolution of the SK analysis. For example, while the vertex resolution is about 50 cm [33], an electron with an energy of 20 MeV can travel about 10 cm in the water.

The vertex position is reconstructed using the timing information of PMT that detected the light. If the hit time of  $i$ -th PMT is  $t_i$ , the generation position of a charged particle is  $(x, y, z)$ , the flight time of the Cherenkov light from the generation position to the  $i$ -th PMT is  $t_{\text{tof}}$ , and the generation time of the charged particle is  $t_0$ , a residual time  $t_{\text{res},i}$  is defined as follow.

$$t_{\text{res},i} = t_i - t_{\text{tof}} - t_0 \quad (3.20)$$

The likelihood function is defined as follows using this residual time.

$$\mathcal{L}(\vec{x}, t_0) = \sum_{i=0}^{N_{\text{hit}}} \ln P(t_{\text{res},i}) \quad (3.21)$$

Where  $\vec{x} = (x, y, z)$  and  $P(t_{\text{res},i})$  is the probability density function of  $t_{\text{res},i}$ . Figure 3.15 shows this probability density function. The likelihood function  $\mathcal{L}(\vec{x}, t_0)$  is calculated while

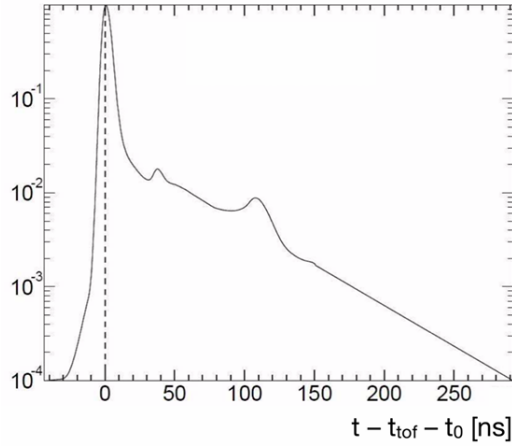


Figure 3.15: The probability density function of  $t_{\text{res},i}$  [46]. The second and third peaks around 40 ns and 110 ns are due to the after pulse of PMT.

changing  $\vec{x}$  in the ID, and  $\vec{x}$  is determined when the value of this function is maximum. The accuracy of the position reconstruction depends on the energy of the charged particle because the number of the Cherenkov photon depends on the energy of the charged particle and the number of PMT hits differs by the number of the Cherenkov photons. Figure 3.16 shows the energy dependence of the vertex resolution determined by LINAC (LINAC is explained in Section 3.4.1). From this figure, the vertex resolution improves as the energy is high. Here, the vertex resolution is defined as the root mean square of the residual difference between the generated position and the reconstructed position.

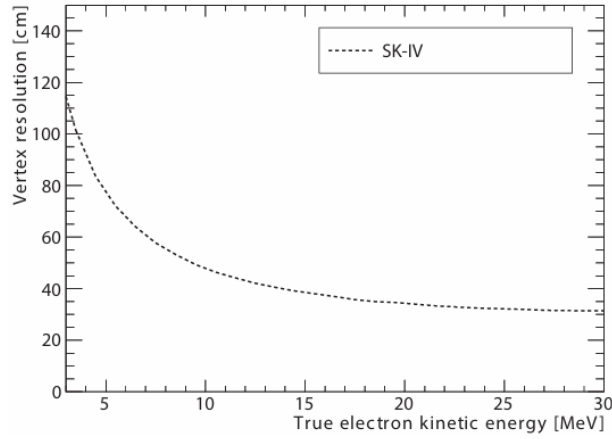


Figure 3.16: The energy dependence of the vertex resolution in SK-IV [36].

The quality of the reconstructed vertex is evaluated using a variable  $g_{vtx}$ .  $g_{vtx}$  is defined as follows.

$$g_{vtx} = \frac{\sum_i \exp \left[ - \left( \frac{t_{\text{res},i}}{\sqrt{2}\omega} \right)^2 \right] \exp \left[ - \left( \frac{t_{\text{res},i}}{\sqrt{2}\sigma} \right)^2 \right]}{\exp \left[ - \left( \frac{t_{\text{res},i}}{\sqrt{2}\omega} \right)^2 \right]} \quad (3.22)$$

Where  $i$  represents  $i$ -th PMT,  $\omega$  represents the resolution of the  $t_i - t_{\text{tof},i}$  distribution, and  $\sigma$  represents the time resolution of the PMT. This variable has a value in the range of 0 to 1. The closer to 1, the better the quality of the reconstruction is.

### 3.3.2 Direction reconstruction

The direction of an event is reconstructed by a hit pattern of the Cherenkov light. This is determined by maximizing the following likelihood function.

$$\mathcal{L}(\vec{d}) = \sum_{i=1}^{N_{20}} \log\{f(\cos \theta_i, E)\} \times \frac{\cos \theta_i}{a(\theta_i)} \quad (3.23)$$

Where  $\vec{d}$  is the direction of movement of the charged particle.  $N_{20}$  is the number of PMT hits when  $t_{\text{res},i}$  is within 20 ns from  $t_0$ .  $f(\cos \theta_i, E)$  is the expected angle distribution of an event with the energy  $E$ .  $\theta_i$  is the angle of incidence of photons on the PMT as shown in Figure 3.17.  $a(\theta_i)$  is a factor that corrects the acceptance of the PMT. Especially, this factor depends on the shape of the PMT and acrylic case.  $a(\theta_i)$  is defined as the following in MC.

$$a(\theta_i) = 0.205 + 0.524 \cos \theta_i + 0.390 \cos^2 \theta_i - 0.132 \cos^3 \theta_i \quad (3.24)$$

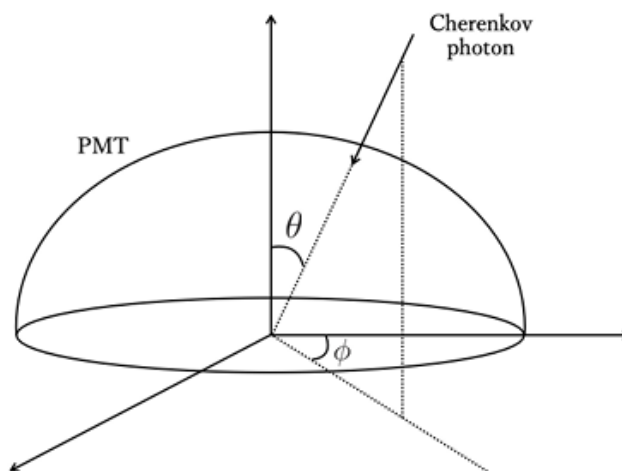


Figure 3.17: The definition of the incident angle of the photon on the PMT [48].

The quality of direction reconstruction is evaluated by the hit pattern of the PMT. This quality  $g_{dir}$  is defined as follows.

$$g_{dir} = \frac{\max\{\angle_{\text{uniform}}(i) - \angle_{\text{data}}(i)\} - \min\{\angle_{\text{uniform}}(i) - \angle_{\text{data}}(i)\}}{2\pi} \quad (3.25)$$

Where  $\angle(i)$  is the azimuth angle of  $i$ -th hit PMT.  $\angle_{\text{uniform}}(i)$  is the angle of the  $i$ -th hit PMT when PMT hits are assumed to be uniformly distributed around the ideal Cherenkov ring.  $\angle_{\text{data}}(i)$  represents the actual angle of the data.  $g_{dir}$  also has a value in the range of 0 to 1. The closer to 0, the better the reconstruction quality is.

### 3.3.3 Effective hits of the PMT $N_{\text{eff}}$

The effective number of PMT hits  $N_{\text{eff}}$  is used to reconstruct energy.  $N_{\text{eff}}$  corrects the water transparency, the noise of the PMT, and the quantum efficiency and gain of the PMT.  $N_{\text{eff}}$  is defined as follows.

$$N_{\text{eff}} \equiv \sum_i^{N_{50}} \left[ (X_i + \epsilon_{\text{tail}}^i - \epsilon_{\text{dark}}^i) \times \frac{N_{\text{all}}}{N_{\text{alive}}} \times \frac{S(0,0)}{S(\theta_i, \phi_i)} \times \exp\left(\frac{r_i}{L_{\text{eff}}^i}\right) \times \frac{1}{QE_i \times CE_i} \right] \quad (3.26)$$

$N_{50}$  is the PMT hits when  $t_i - t_{\text{tof}}$  is within 50 ns from  $t_0$ ,  $i$  represents the  $i$ -th PMT hit,  $N_{\text{all}}$  is the number of all PMTs (11,129), and  $N_{\text{alive}}$  represents the number of PMTs that are working properly. The other parameters are as follows.

- **Occupancy correction:**  $X_i$

$X_i$  is the estimated number of photons detected in a single PMT. The number of photons is estimated from the fraction of the PMTs with hits in a  $3 \times 3$  patch around  $i$ -th PMT ( $x_i$ ) shown in Figure 3.18. Using  $x_i$ , the occupancy correction  $X_i$

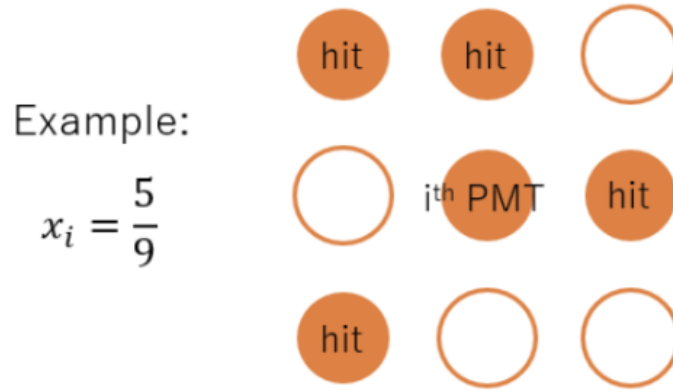


Figure 3.18: The diagram of the estimated number of photons.

is defined as follows.

$$X_i = \begin{cases} \frac{\log\left(\frac{1}{1-x_i}\right)}{x_i} & (x_i < 1) \\ 3.0 & (x_i = 1) \end{cases} \quad (3.27)$$

- **Delayed hit correction:**  $\epsilon_{\text{tail}}$

Some photons reflect at the surface of PMT and the black sheet, and the hit time is later than the normal photons. To correct these photons, the delayed hit correction  $\epsilon_{\text{tail}}$  is carried out.  $\epsilon_{\text{tail}}$  is defined as follows.

$$\epsilon_{\text{tail}}^i = \frac{N_{100} - N_{50} - N_{\text{alive}} \times R_{\text{dark}}^{\text{ave}} \times 50\text{ns}}{N_{50}} \quad (3.28)$$

Where  $N_{100}$  is the PMT hits when  $t_i - t_{\text{tof}}$  is within 100 ns from  $t_0$ ,  $R_{\text{dark}}^{\text{ave}}$  is the average dark noise hit rate of all PMTs ([hits/ns]).

- **Dark noise correction:**  $\epsilon_{\text{dark}}^i$

This factor corrects the dark noise of PMT and is defined as follows.

$$\epsilon_{\text{dark}}^i = \frac{N_{\text{alive}} \times R_{\text{dark}} \times 50ns}{N_{50}} \quad (3.29)$$

- **Photo coverage correction:**  $S(\theta, \phi)$

The coverage area of the photocathode of the PMT differs by the incident angle of the photon. The incident angle  $(\theta, \phi)$  is determined as in Figure 3.19. This dependence on the incident angle is corrected by the function shown in Figure 3.20.

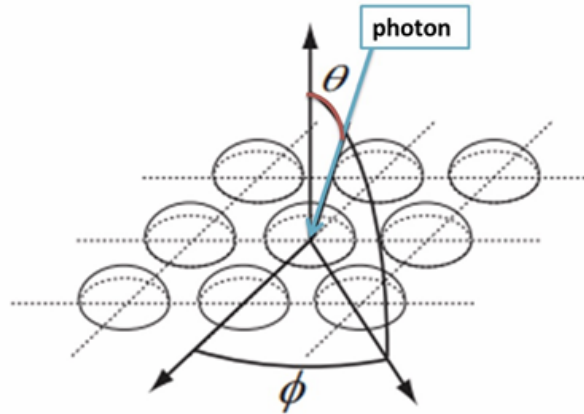


Figure 3.19: The definition of the incident angle of the photon.

- **Water transparency correction:**  $\exp(r_i/L_{\text{eff}}^i)$

This factor corrects the effect of attenuation of photons in the water.  $r_i$  represents the distance between the generated position of an event and the  $i$ -th hit PMT.  $L_{\text{eff}}^i$  is the attenuation length which considers water quality changes.  $L_{\text{eff}}^i$  is calculated using Eq. (3.12), (3.16), and (3.18).

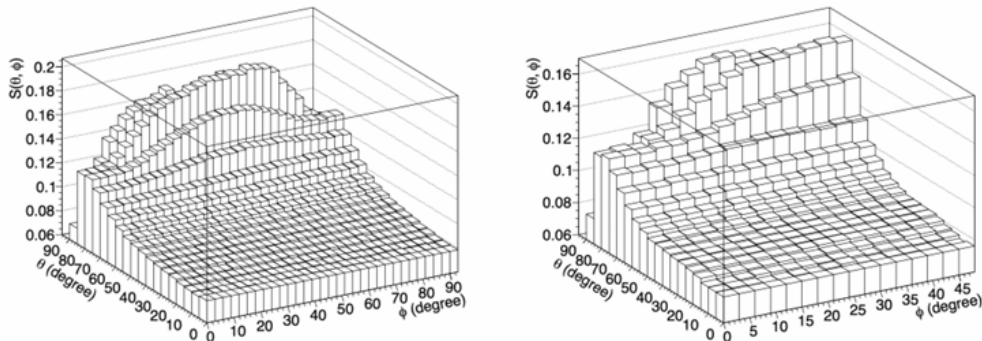


Figure 3.20: The correction function  $S(\theta, \phi)$  which corrects the coverage area of photocathode of the PMT. The left one is for the barrel PMTs and the right one is for the top and bottom PMTs.

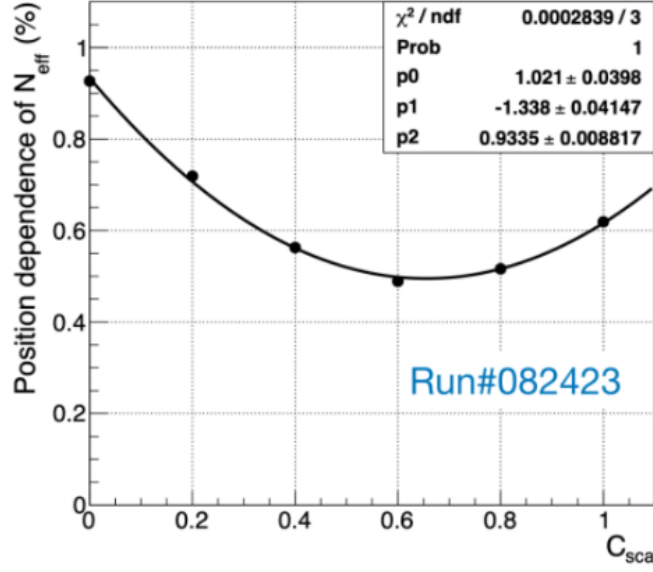


Figure 3.21: The relation between  $C_{sca}$  and the position dependence of  $N_{\text{eff}}$ .

- **Quantum efficiency and collection efficiency correction:**  $1/QE_i \times CE_i$

As described in Section 3.1.3, the quantum efficiency differs by the PMT. Also, as described in Section 3.1.4, the collection efficiency differs by the PMT after the coil failure. Before the coil failure,  $CE_i$  is 1 for all PMTs.

To reduce the position dependence of  $N_{\text{eff}}$ , the parameter  $C_{sca}$  is introduced. 10 MeV electrons are generated in MC with changing the value of  $C_{sca}$ . Then, the best value of  $C_{sca}$  is determined from the value which minimizes the positional dependent variation of  $N_{\text{eff}}$ . Figure 3.21 shows the relationship between  $C_{sca}$  and the position dependence of  $N_{\text{eff}}$ .

### 3.3.4 Energy reconstruction

The energy of an event is reconstructed using the function of  $N_{\text{eff}}$ . In the simulation, mono energy electrons are generated in the detector and  $N_{\text{eff}}$  are calculated. Then, the  $N_{\text{eff}}$  vs the electron energy is plotted and this plot is fitted by a function. This function is defined as follows.

$$E(N_{\text{eff}}) = \begin{cases} \sum_{i=0}^5 p_i (N_{\text{eff}})^i & (N_{\text{eff}} \leq p_6) \\ \sum_{i=0}^5 p_i p_6^i + \sum_{i=1}^5 p_i p_6^{i-1} (N_{\text{eff}} - p_6) & (N_{\text{eff}} > p_6) \end{cases} \quad (3.30)$$

Where  $p_i$  is a fitting parameter,  $p_6$  is the connection point between two functions.  $E(N_{\text{eff}})$  is a 5th polynomial function below  $p_6$  and a linear function above  $p_6$ . Figure 3.22 shows the  $E(N_{\text{eff}})$  function and the values from  $p_0$  to  $p_6$  in SK-VI data.

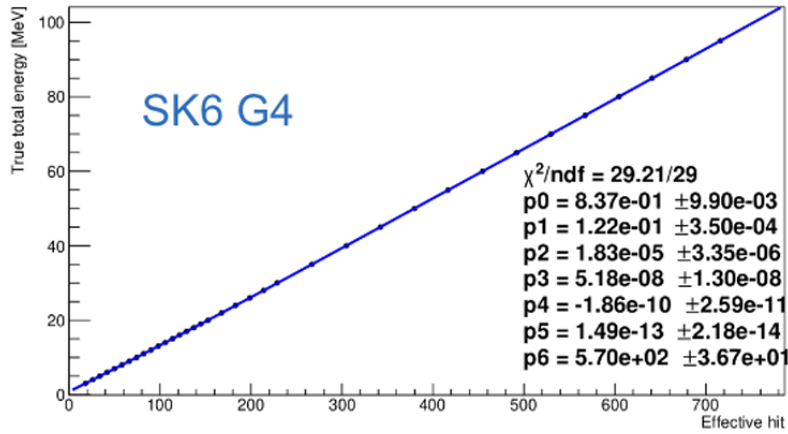


Figure 3.22: The  $E(N_{\text{eff}})$  function and the values from  $p_0$  to  $p_6$  in SK-VI. Black dots show MC simulation results and blue line represents the function derived by fitting. "G4" written in the figure is the name of the simulation package.

## 3.4 Energy calibration

The electron linear accelerator (LINAC) and deuterium-tritium neutron source (DT) are used for energy scale calibration and evaluation of systematic uncertainty. The result of energy calibration using these sources is fed back into the detector MC. Especially, there is a coefficient called "COREPMT", which determines the energy scale in MC. The COREPMT is determined so that the hit detection efficiency of the PMTs in MC is consistent with the data. This coefficient is obtained by the LINAC data.

In this section, the methods of LINAC and DT calibration are explained.

### 3.4.1 LINAC

In the low-energy region, the relation between the amount of the Cherenkov photons emitted from a charged particle and the energy of the charged particle is decided by LINAC. Also, LINAC can evaluate the time and position dependence of the detector.

LINAC is located above the tank as shown in Figure 3.23 [49]. The electrons generated in LINAC go through the D1 and D2 magnets in Figure 3.23, and their trajectories become parallel to the tank. Then, the D3 magnet bends them downwards. The LINAC beam pipe is inserted into the tank, and the electrons are injected into the detector through this pipe. About 0.1 electron per bunch is injected into the tank. The positions from A to I in Figure 3.23 represent the injection position. The coordinates of these positions are summarized in Table 3.3. The kinetic energies of the electrons are 5, 6, 8, 10, 12, and 18 MeV, and electrons with a single energy are injected. Because the LINAC measurement is a large scale, at least 10 people are needed for the measurement and the measurement period is about a few weeks.

The energy of the LINAC beam is measured using a germanium detector. The energy of electrons generated in LINAC is measured with 0.1 % accuracy by this detector.

Then, as described in the above sections, the reconstructions of the generation position, direction, and energy of events are carried out. After the reconstruction of events, the events are selected under the following conditions.

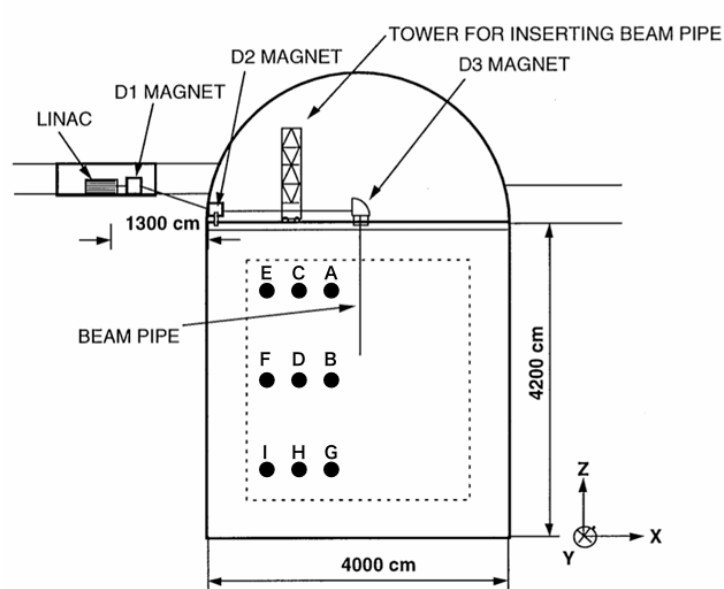


Figure 3.23: The schematic diagram of LINAC. The points from A to I represent the injection position of electrons [49].

Position	x [cm]	y [cm]	z [cm]
A	-388.9	-70.7	+1197
B	-388.9	-70.7	-6
C	-813.1	-70.7	+1197
D	-813.1	-70.7	-6
E	-1237	-70.7	+1197
F	-1237	-70.7	-6
G	-388.9	-70.7	-1209
H	-813.1	-70.7	-1209
I	-1237	-70.7	-1209

Table 3.3: The coordinates of the injection position of the LINAC electron beam.

- A scintillator for a trigger is attached to the end of the pipe and the trigger is issued when an electron passes. The events with the trigger are selected.
- The events with more than one electron are eliminated.
- When the reconstructed position is more than 2 m away from the end of the pipe, these events are removed.

The effective PMT hits  $N_{\text{eff}}$  is used for the evaluation of the energy scale. The  $N_{\text{eff}}$  of the LINAC data and MC are compared. Ideally, the  $N_{\text{eff}}$  of the data and MC should match, but they don't. This is due to the complicated characteristics of PMT or photon transport process which are not considered in the analysis. To correct this mismatch, the parameter "COREPMT" is introduced. This parameter is used for the low-energy analysis. In SK, there are two MC package. One is SKDETSIM, which is based on the Geant3, and the other is SKG4, which is based on the Geant4. Table 3.4 shows the value of COREPMT for each MC package and measurement phase. In our study, SKG4 is used and is discussed in detail in Chapter5.

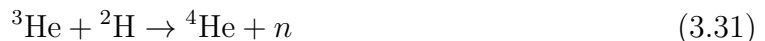
Phase	SKDETSIM	SKG4
SK-IV	0.866169	
SK-V	0.85142	
SK-VI	0.8648811	0.887656
SK-VII		0.909324

Table 3.4: The value of COREPMT for each MC package and measurement phase.

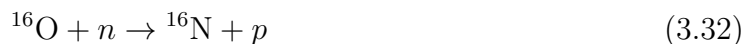
Figure 3.24 shows the result of the LINAC data and MC after correcting by the COREPMT factor, in SK-IV. The red dot lines represent  $\pm 0.5\%$  difference. The systematic uncertainty on the  $N_{\text{eff}}$  throughout the detector is  $0.40\%$  for SK-IV.

### 3.4.2 DT

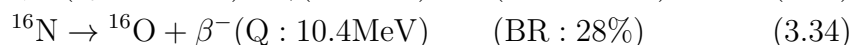
DT (Deuterium-Tririum neutron) generator is a calibration equipment that generates neutrons in the following reaction.



The energy of the generated neutron is 14.2 MeV. Then, it interacts with oxygen in the water and produces  ${}^{16}\text{N}$ .



The generated  ${}^{16}\text{N}$  has a half-life time of 7.13 s. It decays as the following reaction. Here, the decays with the Branching Ratio (BR) greater than  $1\%$  are described.



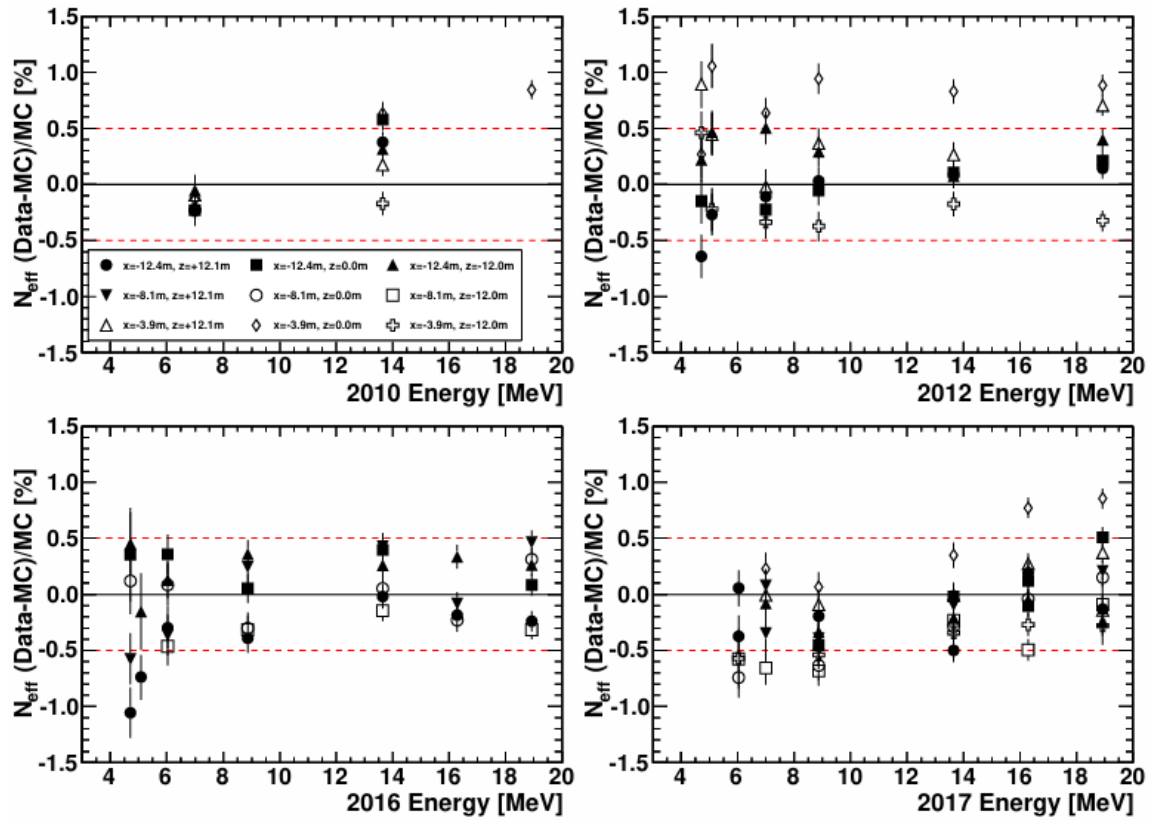


Figure 3.24: The  $N_{\text{eff}}$  difference of the LINAC data and MC in SK-IV [33]. Each marker represents each injection position. The red dot lines represent  $\pm 0.5\%$  difference.

The DT measurement is a smaller scale than the LINAC measurement, so the measurement can be performed by a relatively small number of people in a short time. Unlike LINAC, especially in the x- and y-direction, the data can be obtained at different positions. Also, while electrons can only be injected downwards in LINAC, the  $\beta$  and  $\gamma$  rays are emitted isotropically from  $^{16}\text{N}$  decays. Therefore, DT calibration evaluates the position and direction dependence more precisely than LINAC.

Figure 3.25 shows the schematic diagram of DT calibration [50]. The steps of measurement are below.

- a Install the DT generator (DTG) at the specific position in the detector using a crane.
- b Operate the DTG. About  $10^6$  neutrons are generated around the DTG and about  $10^4$   $^{16}\text{N}$  are generated in the water.
- c The DTG is raised 2 m so that its shadow does not interfere with the measurement. Then, start to obtain the data.

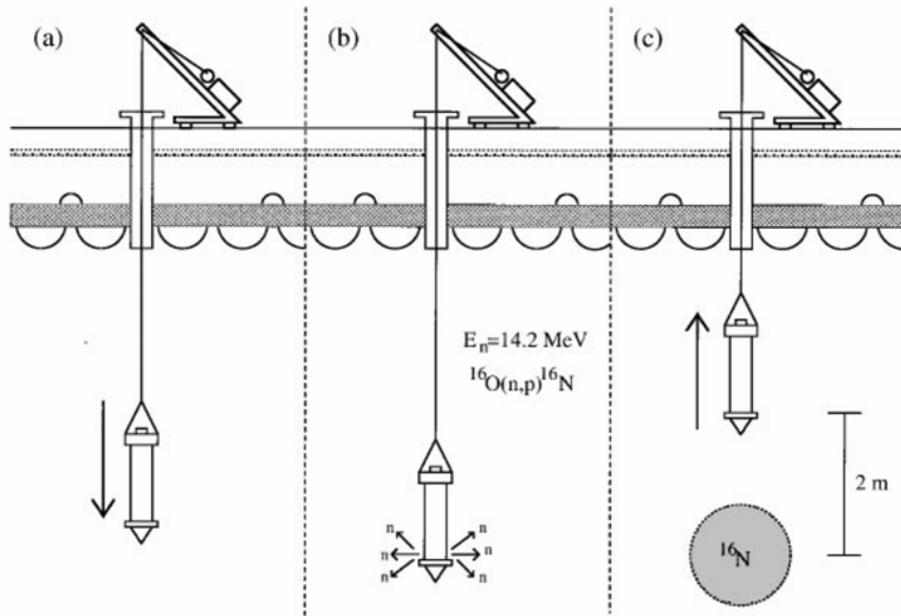


Figure 3.25: The schematic diagram of the DT measurement [50].

The position dependence, direction dependence, and time variation of the energy scale are evaluated by comparing  $N_{\text{eff}}$  of the DT data and MC. Figure 3.26 and 3.27 show the DT calibration result in SK-IV [33].

### 3.5 Energy scale monitoring

Because the condition of the water in the detector is continuously changing, evaluating the time variation of the energy scale is important. To monitor the time variation of

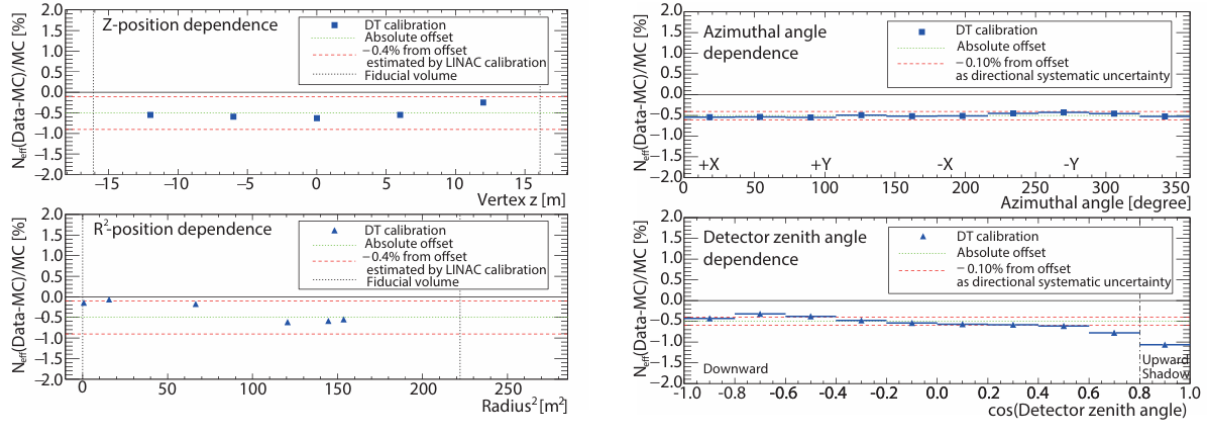


Figure 3.26: The position dependence (left) and directional dependence (right) of  $N_{\text{eff}}$  from DT calibration data in SK-IV [33].

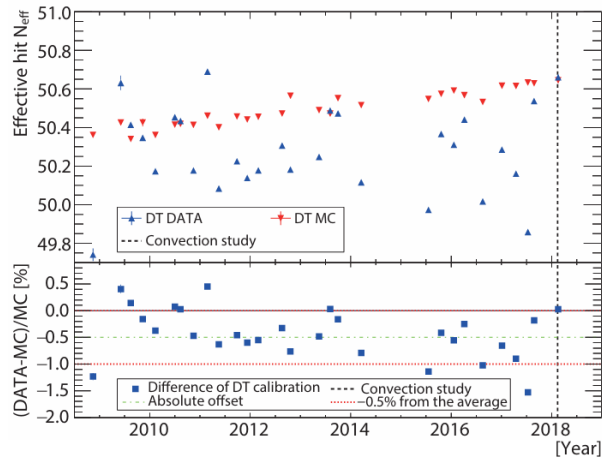


Figure 3.27: The time variation of  $N_{\text{eff}}$  from DT calibration data in SK-IV [33].

the energy scale, cosmic-ray-induced sources are used. In this section, the energy scale monitoring using the cosmic-ray-induced sources ( $^{16}\text{N}$  and decay electrons) are discussed.

### 3.5.1 $^{16}\text{N}$ analysis

When a cosmic ray muon enters the SK detector and is captured by  $^{16}\text{O}$  in the water,  $^{16}\text{N}$  is produced and a muon neutrino is emitted.



The produced  $^{16}\text{N}$  undergoes the reaction in Eqs. (3.33)-(3.35). These  $\beta$  and  $\gamma$  rays can be also used for energy calibration. Because the observed decay events have the same energy range as solar neutrinos, this calibration evaluates the energy scale for solar neutrino detection. Unlike DT, this calibration uses the reaction of the cosmic ray muons, so it can monitor the entire detector. Also, because the cosmic ray muons enter the detector at about 2 Hz, this calibration can monitor the entire SK period. However, since  $^{16}\text{N}$  is produced at a low rate, it takes a long time to get enough statistics.

Figure 3.28 shows the result of  $^{16}\text{N}$  calibration [51]. The energy scale was evaluated every 2 years for SK-IV and every 6 months for SK-V and SK-VI. The energy scale in the detector was within the statistical error range from SK-IV to SK-VI. The positional and directional dependence of the energy scale in SK-IV is shown in Figure 3.29 and Figure 3.30. It was compared to the DT calibration result. From these figures, the energy scale has no position or direction dependence within a statistical error of  $^{16}\text{N}$  analysis.

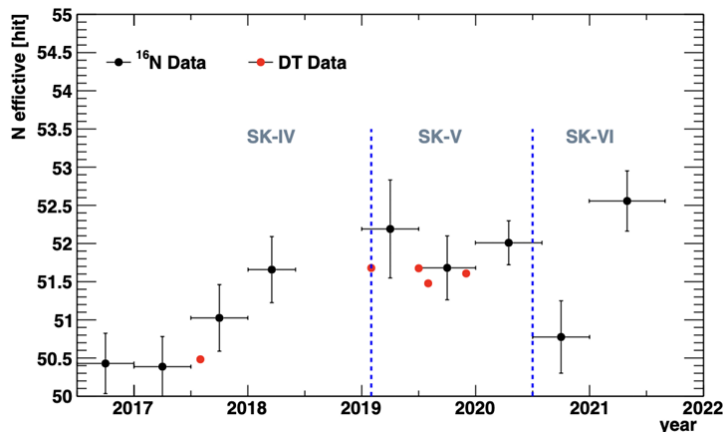


Figure 3.28: Energy scale evaluation of  $^{16}\text{N}$  and DT calibration [51]. The black dots represent the  $^{16}\text{N}$  data and the red dots represent the DT data.

### 3.5.2 Decay electron analysis

Decay electrons from cosmic ray muons are used to evaluate the energy scale as well as the time variations of the water transparency. Figure 3.31 shows the reconstructed energy spectrum of the decay electrons. The range of the decay electrons' energy is about 10 MeV to 60 MeV. Therefore, the decay electrons can evaluate the energy scale larger than 10 MeV. Same as  $^{16}\text{N}$ , the decay electron events can be detected throughout the

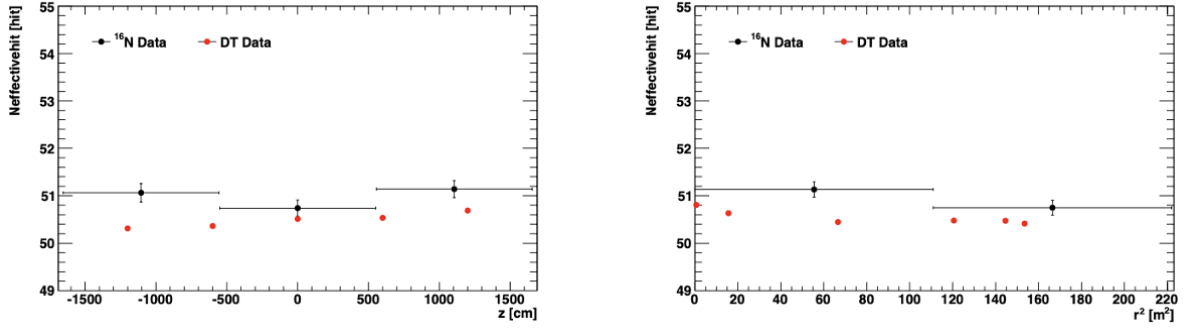


Figure 3.29: The position dependence of  $^{16}\text{N}$  and DT calibration [51]. The left one is the  $z$ -dependence and the right one is the  $r^2$ -dependence. The black dots represent the  $^{16}\text{N}$  data and the red dots represent the DT data.

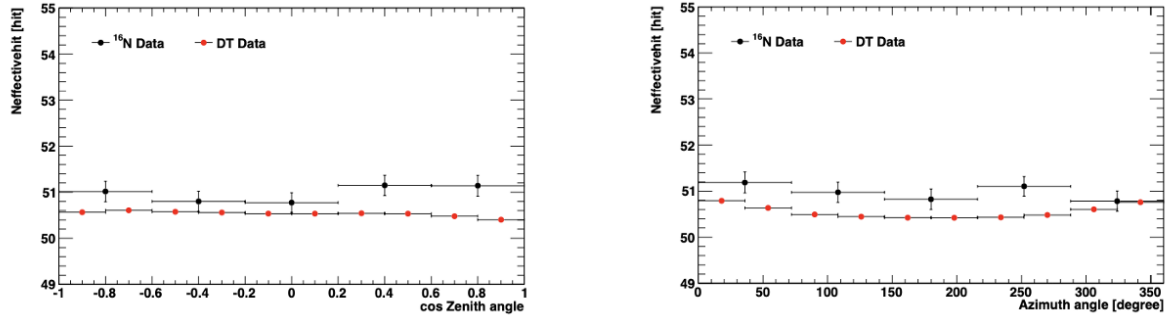


Figure 3.30: The directional dependence of  $^{16}\text{N}$  and DT calibration [51]. The left one is zenith angle  $\cos\theta$  dependence and the right one is azimuth  $\phi$  dependence. The black dots represent the  $^{16}\text{N}$  data and the red dots represent the DT data.

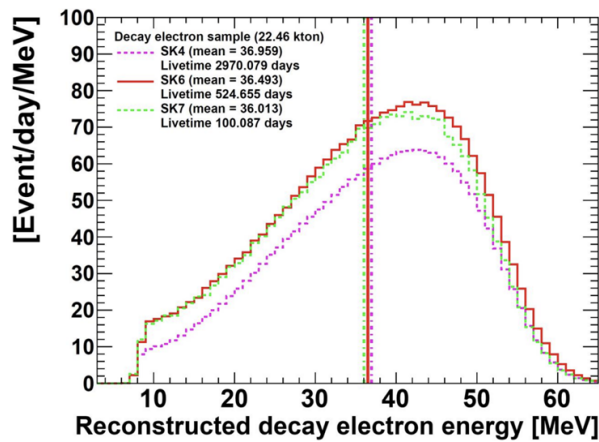


Figure 3.31: The energy spectrum of the reconstructed decay electrons [52].

entire SK tank and the entire SK period. On the other hand, because the decay electrons are also produced at a low rate, it takes a long time to get enough statistics.

# Chapter 4

## Spallation neutron capture on gadolinium

In the low-energy region of Super-Kamiokande, the physics targets are the observation of solar neutrinos and the search for DSNB. For solar neutrino observations, the systematic uncertainty of the energy scale is 0.48 % and 0.40 % is due to position dependence now [33] (Section 3.4.1). To reduce this systematic uncertainty, a calibration method to evaluate position dependence more precisely is necessary. It is also important to evaluate the time stability of the detector's energy scale. Spallation neutron capture on gadolinium is one of the calibration sources that can evaluate the energy scale of the overall detector and time stability.

In this chapter, spallation neutrons and their characteristics are explained first. Then, spallation neutron captures on gadolinium and how to select those events are discussed.

### 4.1 Spallation neutron by cosmic ray muon

#### 4.1.1 Muon generation by cosmic ray

Cosmic rays, mainly protons, that fall on Earth from outer space interact with atomic nuclei in the atmosphere to produce hadrons. Those hadrons are mainly  $\pi$  mesons and  $K$  mesons and they decay into muons as follows.

$$\pi^+ \rightarrow \mu^+ + \nu_\mu \quad (4.1)$$

$$\pi^- \rightarrow \mu^- + \bar{\nu}_\mu \quad (4.2)$$

$$K^+ \rightarrow \mu^+ + \nu_\mu \quad (4.3)$$

$$K^- \rightarrow \mu^- + \bar{\nu}_\mu \quad (4.4)$$

Those muons are called cosmic ray muons. Figure 4.1 shows the production of cosmic ray muons above the Super-Kamiokande detector. The cosmic ray muons enter the SK detector at the rate of about 2 Hz. The lifetime of muons is about 2.2  $\mu$ s and they decay as follows via weak interaction.

$$\mu^+ \rightarrow e^+ + \nu_e + \bar{\nu}_\mu \quad (4.5)$$

$$\mu^- \rightarrow e^- + \bar{\nu}_e + \nu_\mu \quad (4.6)$$

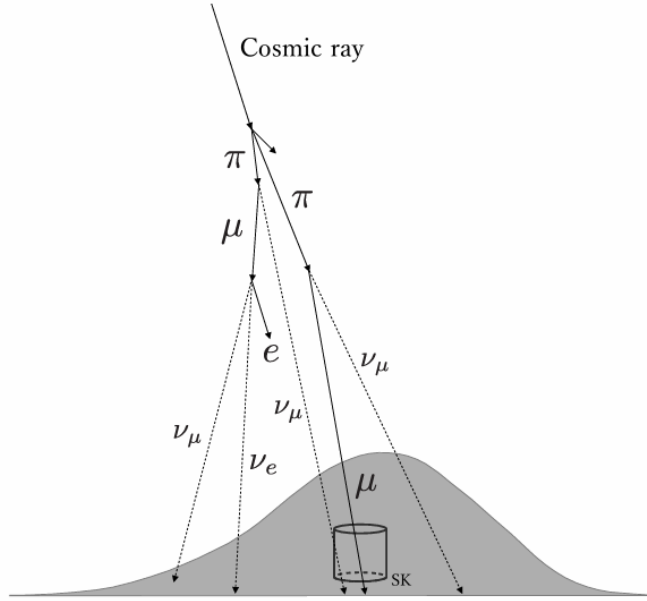


Figure 4.1: Production of cosmic ray muon above the SK detector.

#### 4.1.2 Spallation neutron by cosmic ray muons

When cosmic ray muons pass through a material, they sometimes crush atomic nuclei in the material. This interaction is called spallation and Figure 4.2 shows the overview of spallation. In Super-Kamiokande, cosmic ray muons mainly make spallation reactions

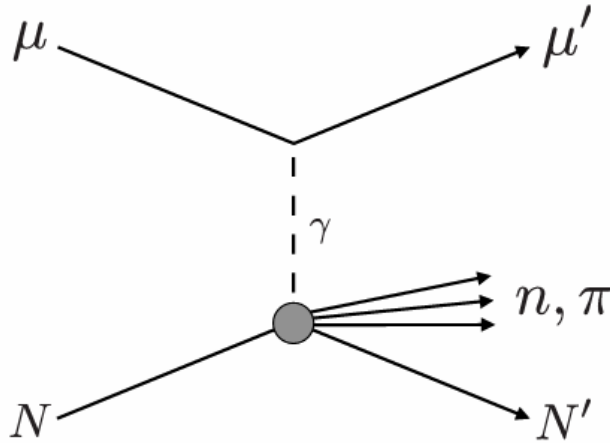


Figure 4.2: Spallation by a muon.

with oxygen nuclei and produce neutrons and many kinds of radioisotopes. Table 4.1 shows expected radioisotopes due to oxygen nucleus spallation [53, 54]. The neutrons generated by spallation are called spallation neutrons. They are thermalized within about  $5 \mu\text{s}$  and captured on hydrogen or gadolinium. From this table, the neutron yield is expected to be  $2.030 \times 10^{-4} \mu^{-1} \text{g}^{-1} \text{cm}^2$ , so about 0.65 neutrons are generated per cosmic ray muon in the SK detector. Because cosmic ray muons enter the detector at the rate of about 2 Hz, we expect about 113,000 spallation neutron events per day.

Isotope	Life time (s)	Decay mode	$E_{\text{kin}}$ (MeV)	yield ( $\times 10^{-7} \mu^{-1} \text{g}^{-1} \text{cm}^2$ )
Neutron				2030
$^{11}\text{Be}$	19.9	$\beta^-$ (55 %)	11.51	0.81
		$\beta^- \gamma$ (31 %)	9.41+2.10( $\gamma$ )	
$^{16}\text{N}$	10.3	$\beta^-$ (66 %)	10.44	18
		$\beta^- \gamma$ (28 %)	4.27+6.13 ( $\gamma$ )	
$^{15}\text{C}$	3.53	$\beta^-$ (63 %)	9.77	0.82
		$\beta^- \gamma$ (37 %)	4.51+5.30 ( $\gamma$ )	
$^8\text{Li}$	1.21	$\beta^-$	$\sim 13.0$	13
$^8\text{B}$	1.11	$\beta^+$	$\sim 13.9$	5.8
$^{16}\text{C}$	1.08	$\beta^- + \text{n}$	$\sim 4$	0.02
$^9\text{Li}$	0.26	$\beta^-$ (49 %)	13.6	1.9
		$\beta^- + \text{n}$ (51 %)	$\sim 10$	
$^9\text{C}$	0.18	$\beta^- + \text{p}$	3 $\sim$ 5	0.89
$^8\text{He}$	0.17	$\beta^- \gamma$ (84 %)	9.67+0.98 ( $\gamma$ )	0.23
		$\beta^- + \text{n}$ (16 %)		
$^{12}\text{Be}$	0.034	$\beta^-$	11.71	0.10
$^{12}\text{B}$	0.029	$\beta^-$	13.37	12
$^{13}\text{B}$	0.025	$\beta^-$	13.44	1.9
$^{14}\text{B}$	0.020	$\beta^- \gamma$	14.55+6.09 ( $\gamma$ )	0.02
$^{12}\text{N}$	0.016	$\beta^+$	16.38	1.3
$^{13}\text{O}$	0.013	$\beta^+ + \text{p}$	8 $\sim$ 14	0.26
$^{11}\text{Li}$	0.012	$\beta^- + \text{n}$	20.62	0.01

Table 4.1: Predicted radioisotopes by oxygen nucleus spallation with cosmic ray muons in the SK detector. The fourth column shows the maximum kinetic energy of the emitted electron or positron. The fifth column shows an expected yield of the radioisotope [53, 54].

## 4.2 Spallation neutron captures on gadolinium

### 4.2.1 Feature of spallation neutron capture events

When a spallation neutron is captured by hydrogen, one gamma ray of 2.2 MeV is emitted. When it is captured by gadolinium, several gamma rays of about 8 MeV in total are emitted. As described in Section 2.4.1, the fraction of neutron captures on Gd is about 50 % at 0.01 % Gd mass concentration, and that is about 75 % at 0.03 % Gd mass concentration. The relationship between the Gd concentration and the time constant of neutron captures on Gd is empirically expressed as follows [55].

$$c_{\text{Gd}} \simeq \left( \frac{8.19}{\tau} - 0.0371 \right) \times \frac{1}{310} \times 100 \quad (4.7)$$

Where  $c_{\text{Gd}}$  is the Gd mass concentration [%] and  $\tau$  [ $\mu\text{s}$ ] is the time constant. From this equation, the time constant is about 120  $\mu\text{s}$  for 0.01 % concentration (SK-VI) and about 63  $\mu\text{s}$  for 0.03 % concentration (SK-VII).

### 4.2.2 Advantages and disadvantages of calibration using spallation neutron capture events

There are two major advantages to the calibration using spallation neutron captures on gadolinium. Those advantages are that these events occur at a high rate and throughout the entire detector volume. Because cosmic ray muons arrive at the SK detector at the rate of about 2 Hz, it is expected that about 100,000 spallation neutrons are produced each day in the detector. Thanks to this high rate, sufficient statistics are obtained in a short time to monitor the detector performance. Because spallation neutrons are caused by natural sources, the signals of spallation neutron captures on Gd can be obtained constantly unlike LINAC and DT. The decay electrons and spallation  $^{16}\text{N}$  are also detected throughout the entire detector, but these events occur infrequently (about 20 events per day) compared to the spallation neutron captures. So they take a long time to obtain the sufficient statistics.

In addition, since cosmic ray muons enter the detector almost uniformly, spallation neutrons can also be detected almost uniformly in the detector. Therefore, the position dependence of the detector can be monitored in more detail than LINAC and DT.

On the other hand, there are some disadvantages. One is that because the detected energy of spallation neutron capture on gadolinium is low and it is close to the trigger threshold, special treatment to remove background signals is required. Another one is that it is necessary to consider the effect of pile-up. Also, since gamma rays, not electrons, are initially produced in a spallation neutron capture reaction, it is harder to reconstruct than the calibrations with electrons. The comparison of advantages and disadvantages with other energy calibrations are summarized in Figure 4.3. We develop the energy calibration method using spallation neutron captures on gadolinium. The aim is to develop a calibration with an accuracy of 0.5 %, which is the same level of position dependence in SK-IV solar neutrino observation [33]. In the following section, the method of this calibration is discussed.

	Calibration	advantage	disadvantage
With instruments	<b>LINAC</b>	<ul style="list-style-type: none"> <li>• Injection of single energy electron</li> <li>• The energy of electron is fixed</li> </ul>	<ul style="list-style-type: none"> <li>• Number of people is needed</li> <li>• Injected once or twice a year</li> <li>• The position is fixed</li> </ul>
	<b>DT calibration</b>	<ul style="list-style-type: none"> <li>• More positional flexibility than LINAC</li> <li>• Directional dependence of energy scale can be measured</li> <li>• Possible to work with a relatively small number of people</li> </ul>	<ul style="list-style-type: none"> <li>• DTG itself interferes with the progress of Cherenkov light</li> <li>• The energy of electron is not fixed</li> </ul>
	<b>Ni</b>	<ul style="list-style-type: none"> <li>• Possible to work with a relatively small number of people</li> </ul>	<ul style="list-style-type: none"> <li>• The position is fixed</li> </ul>
Cosmic ray induced	<b>Decay e</b>	<ul style="list-style-type: none"> <li>• Throughout the entire SK tank events</li> <li>• Analysis over the entire period is possible</li> </ul>	<ul style="list-style-type: none"> <li>• Few numbers of events</li> <li>• Long observation time is required</li> </ul>
	<b><math>^{16}\text{N}</math></b>	<ul style="list-style-type: none"> <li>• Throughout the entire SK tank</li> <li>• Analysis over the entire period is possible</li> <li>• Directional dependence of energy scale can be measured</li> </ul>	<ul style="list-style-type: none"> <li>• Few numbers of events (about 20 events per day)</li> <li>• Long observation time is required</li> </ul>
	<b>Spallation neutron</b>	<ul style="list-style-type: none"> <li>• Throughout the entire SK tank events</li> <li>• Analysis over the entire period is possible</li> <li>• A lot of events (about 100,000 events per day)</li> </ul>	<ul style="list-style-type: none"> <li>• Need to detect photon energy</li> <li>• Relatively low energy and close to the trigger threshold</li> </ul>

Figure 4.3: Comparison of the calibration with spallation neutron captures on gadolinium with other energy calibration methods.

### 4.3 Event selection of spallation neutron capture events

For the energy calibration method using spallation neutron captures on gadolinium, it is necessary to select those events appropriately. The overview of this selection is below.

1. Select cosmic ray muon events.
2. Sub-trigger is issued and sub-events are detected.
3. Spallation neutron captures on gadolinium are selected by a certain selection.

The detailed event selections are explained in the following sections. These selections are based on the previous research [48].

#### 4.3.1 Cosmic ray muon selection

The conditions for the event selection of cosmic ray muon are the following two points.

- Both the OD and SHE triggers are issued.
- The total integrated charge of the signal in the ID ( $Q_\mu$ ) is larger than 10,000 p.e.

Because a cosmic ray muon has a charge, the OD PMTs detect the light, and the OD trigger is issued when it enters the SK detector. After that, the muon loses several GeV of energy in the ID and emits Cherenkov light. Then, the ID PMTs detect the light and the SHE trigger is issued for the events that the PMT hits within 200 ns ( $N_{200}$ ) is larger than 60. Then, the PMT hits within  $[-5, 35] \mu\text{s}$  time window are saved. The condition of the total integrated charge in the ID ( $Q_\mu$ ) is that  $Q_\mu > 10,000$  p.e. Figure 4.4 shows the

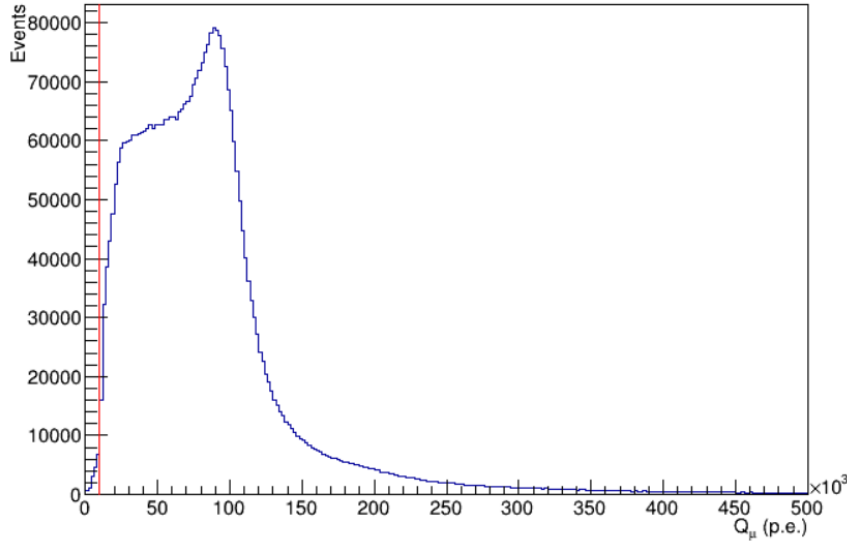


Figure 4.4: The  $Q_\mu$  distribution.  $Q_\mu$  is the total integrated charge detected by the ID PMTs in the SHE trigger. The red line indicates the position of  $Q_\mu \lesssim 10,000$  p.e. The events to the right of the red line are selected.

$Q_\mu$  distribution in the SHE trigger. The AFT trigger is also issued right after the SHE trigger. The time window of the AFT trigger is  $[35, 535] \mu\text{s}$  and all PMT hits within this time window are saved. Then, we search for sub-events from the hits recorded by the SHE and AFT triggers. The sub-trigger is issued when there are above 20 PMT hits within 200 ns ( $N_{200} > 20$ ). When the sub-trigger is issued,  $1.3 \mu\text{s}$  time window around the event is saved as the sub-event. This sub-event is the candidate of the spallation neutron captures on gadolinium. Figure 4.5 shows the diagram of SHE and AFT triggers and sub-events.

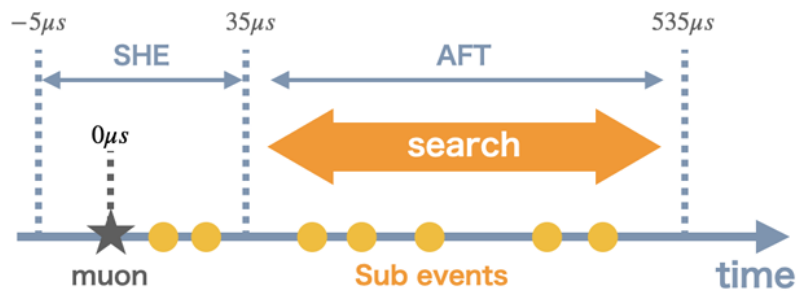


Figure 4.5: The diagram of SHE and AFT triggers and sub-events. When cosmic ray muon enters the SK detector, that time is set to 0 and SHE and AFT triggers are issued. Signals that exceed the sub-trigger ( $N_{200} = 20$ ) are stored as sub-events with  $1.3 \mu\text{s}$  time window.

### 4.3.2 Spallation neutron capture events selection

As mentioned in the last section, the spallation neutron captures on gadolinium are selected from the sub-events found in the SHE and AFT triggered events. The conditions of the selection are below.

#### Signal and background time window

Because a muon decays after the lifetime of about  $2.2 \mu\text{s}$  (in Section 4.1.1), the produced electron or positron can be detected light after muon signals. It has been found that the PMTs attached to the SK tank generate afterpulses about  $10\text{-}20 \mu\text{s}$  after receiving the main pulse [56]. The spallation neutron captures on gadolinium are searched for in the AFT trigger to reduce these events.

Figure 4.6 shows the schematic diagram of the  $dt$  distribution of the spallation neutron captures on gadolinium. The  $dt$  is the time difference between the arrival of the cosmic ray muon and the spallation neutron capture on gadolinium. The spallation neutron captures on gadolinium decreases exponentially with  $dt$  while the backgrounds are constant. These background signals include the beta decay of  $^{214}\text{Bi}$  nuclide. The time constant of spallation neutron captures depends on the Gd concentration. The time constant is  $\sim 120 \mu\text{s}$  at  $0.01 \%$  Gd concentration (SK-VI) and  $\sim 60 \mu\text{s}$  at  $0.03 \%$  Gd concentration (SK-VII) [55]. Figure 4.7 shows the  $dt$  distribution of the spallation neutron captures on gadolinium in the SK-VI and SK-VII periods. To statistically remove these background

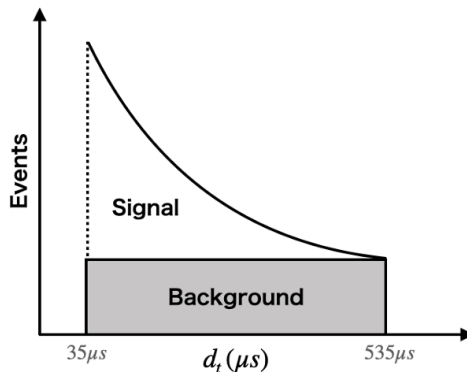


Figure 4.6: The schematic diagram of the  $dt$  distribution of the spallation neutron capture on gadolinium.

signals, two time windows are set in the AFT trigger. One is a signal region and the other is a background region. Since the time constants are  $\sim 120 \mu\text{s}$  at  $0.01 \%$  Gd and  $\sim 60 \mu\text{s}$  at  $0.03 \%$  Gd, the time window of the signal region is set to  $[35, 235] \mu\text{s}$  so that most capture events are included in this time window. The last  $200 \mu\text{s}$  of the AFT trigger ( $[335, 535] \mu\text{s}$ ), which is the same time width of the signal region, is used as the background region. Finally, the events in the background region are subtracted from that in the signal region.

#### Fiducial volume

The rock around the SK detector contains some radioisotopes, and these radioisotopes emit gamma rays or beta rays. These events are the background signals for spallation neutron captures. To remove these backgrounds, the area more than  $2 \text{ m}$  away from the walls of the ID is taken as the fiducial volume. The size of the fiducial volume is a cylinder

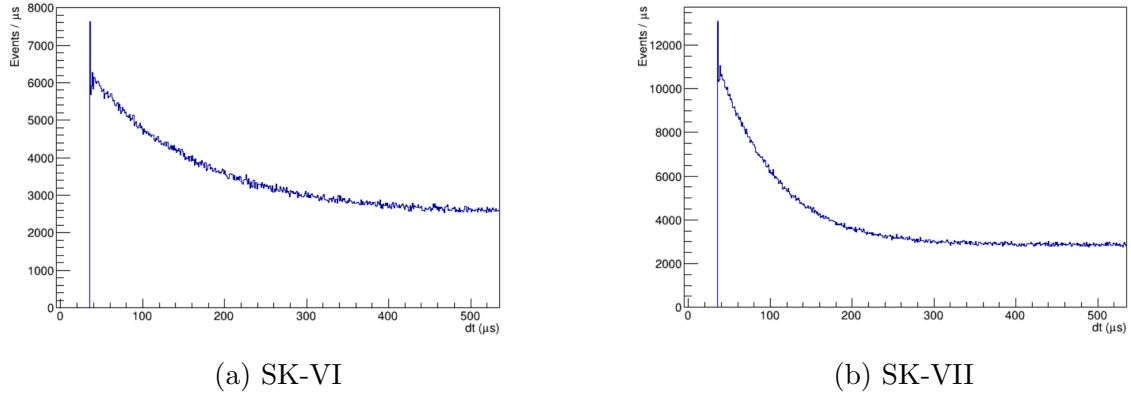


Figure 4.7: The  $dt$  distribution of the spallation neutron captures on gadolinium in SK-VI and SK-VII period.

with a radius of 14.9 m and a height of 32.2 m, and a capacity of 22.5 kilotons. The events that occurred in the fiducial volume are selected.

## Reconstruction quality

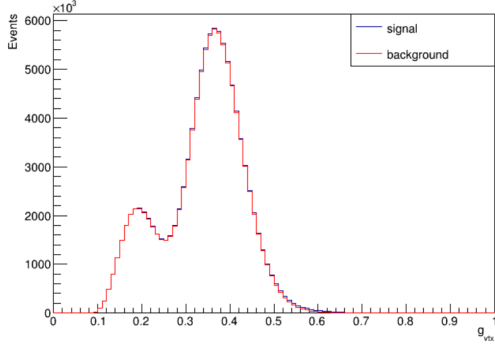
The main background of the spallation neutron captures on gadolinium are radioactive impurities in the SK tank. These backgrounds are constantly occurring near the wall of the tank. To remove these backgrounds that are reconstructed in the fiducial volume accidentally, quantities related to reconstruction quality are used. These reconstruction qualities are evaluated using parameters  $g_{vtx}$  and  $g_{dir}$  (in Section 3.3.1 and Section 3.3.2). The distributions of  $g_{vtx}$  and  $g_{dir}$  are shown in Figure 4.8b and Figure 4.9b respectively. For these figures, only the fiducial volume cut is applied to the data. The closer the value of  $g_{vtx}$  is to 1, the better the event position reconstruction is. The closer the value of  $g_{dir}$  is to 0, the better the direction reconstruction is. These distributions are obtained by subtracting the background region signals ( $[335, 535] \mu\text{s}$ ) from the signal region signals ( $[35, 235] \mu\text{s}$ ). Figure 4.8a and Figure 4.9a show the  $g_{vtx}$  and  $g_{dir}$  distributions in the signal region and background region.

The events forming two peaks in the small  $g_{vtx}$  region shown in Figure 4.8b. These signals are considered to be background events which are mistaken for spallation neutron captures. (This is checked in Section 5 by comparing with Monte Carlo simulation.) Therefore the events with the  $g_{vtx} < 0.4$  are excluded. Regarding the  $g_{dir}$ , it is set to a condition of  $g_{dir} < 0.4$  to select events with high reconstruction accuracy. In summary, the condition of the  $g_{vtx}$  and  $g_{dir}$  is set to the following.

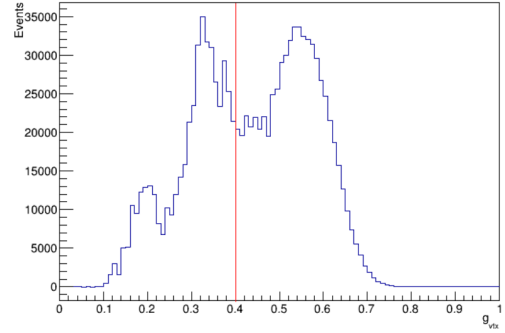
$$(g_{vtx} > 0.4) \wedge (g_{dir} < 0.4) \quad (4.8)$$

## Distance between muon track and neutron capture vertex $L_t$

A spallation neutron produced by a cosmic ray muon is thermalized within about  $5 \mu\text{s}$  and this thermal neutron is captured by gadolinium (or hydrogen). This capture event is not likely to be far from the muon track. Figure 4.10 shows the distance between the muon track and reconstruction point of neutron captures  $L_t$ . Figure 4.11b shows the  $L_t$  distribution. For this figure, the fiducial volume cut and reconstruction quality cut are

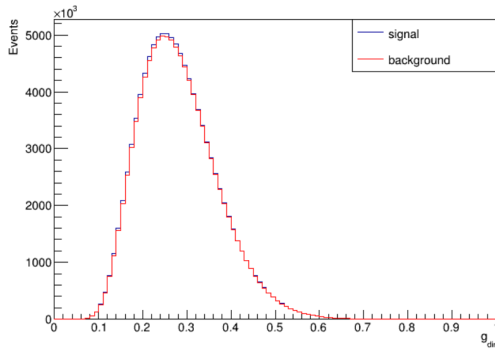


(a)

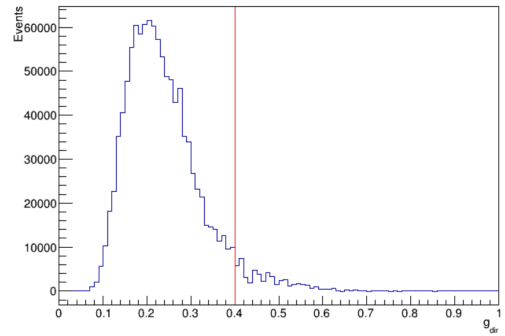


(b)

Figure 4.8: (a) The  $g_{vtx}$  distribution in the signal region and background region. The blue line represents the signal region ( $[35, 235] \mu s$ ) and the red line represents the background region ( $[335, 535] \mu s$ ). (b) The  $g_{vtx}$  distribution of subtracting the background region from the signal region. The right side of the red line ( $g_{vtx} > 0.4$ ) is selected.



(a)



(b)

Figure 4.9: (a) The  $g_{dir}$  distribution in the signal region and background region. The blue line represents the signal region ( $[35, 235] \mu s$ ) and the red line represents the background region ( $[335, 535] \mu s$ ). (b) The  $g_{dir}$  distribution of subtracting the background region from the signal region. The left side of the red line ( $g_{dir} < 0.4$ ) is selected.

applied to the data. This distribution is obtained by subtracting the background region signals ( $[335, 535] \mu\text{s}$ ) from the signal region signals ( $[35, 235] \mu\text{s}$ ). Figure 4.11a shows the  $L_t$  distribution in the signal region and background region. The condition of  $L_t$  is set to:

$$L_t < 300\text{cm}, \quad (4.9)$$

as shown in Figure 4.11b. About 90 % of the signal events passes this cut.

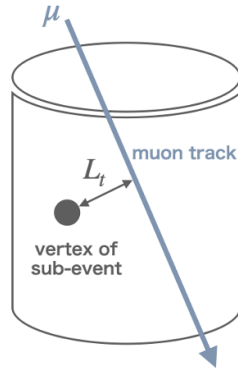


Figure 4.10: Distance between muon track and reconstructed point of neutron capture event.

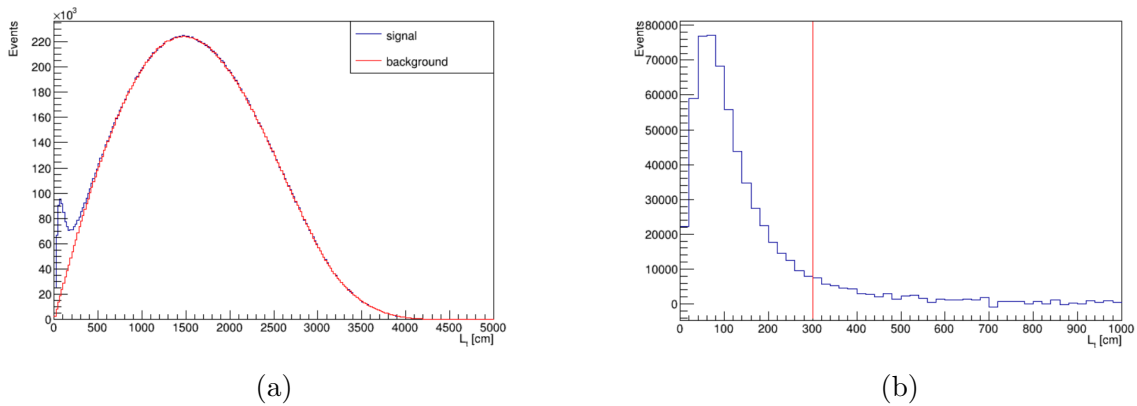


Figure 4.11: (a) The  $L_t$  distribution in the signal region and background region. The blue line represents the signal region ( $[35, 235] \mu\text{s}$ ) and the red line represents the background region ( $[335, 535] \mu\text{s}$ ). (b) The  $L_t$  distribution of subtracting the background region from the signal region. The left side of the red line ( $L_t < 300 \text{ cm}$ ) is selected.

## Reconstructed event time

When the time of the event is reconstructed successfully, the reconstruction time value of the event is expected to be around  $0.9 \mu\text{s}$ . However, if there are multiple events in a trigger, the events cannot be reconstructed well, and the reconstructed time is also shifted. Figure 4.12b shows the distribution of the reconstructed time. For this figure, the fiducial volume cut, reconstruction quality cut, and  $L_t$  cut are applied to the data. This histogram is obtained by subtracting the background region signals ( $[335, 535] \mu\text{s}$ ) from the signal

region signals ( $[35, 235] \mu s$ ). Figure 4.12a shows the reconstructed time distribution in the signal region and background region.

From Figure 4.12b, the condition of the reconstructed time  $t_0$  is set to:

$$t_0 = [0.7, 1.0] \mu s, \quad (4.10)$$

as shown in Figure 4.12b

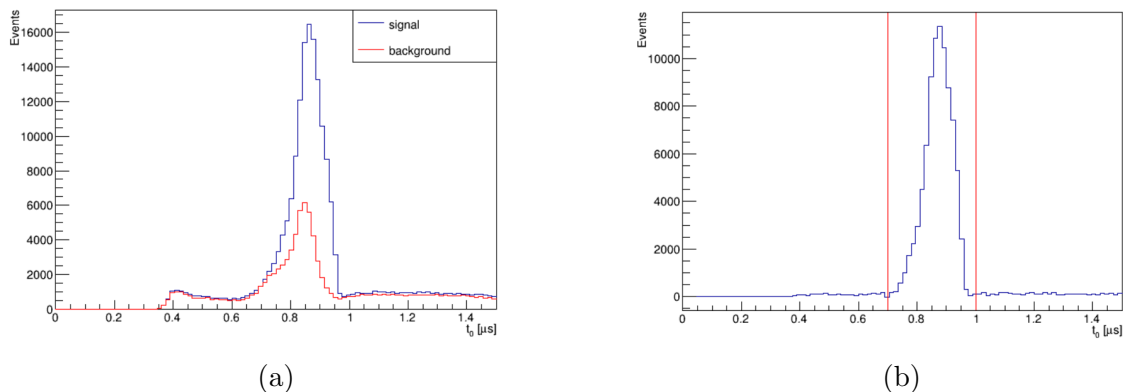


Figure 4.12: (a) The reconstructed time  $t_0$  distribution in the signal region and background region. The blue line represents the signal region ( $[35, 235] \mu s$ ) and the red line represents the background region ( $[335, 535] \mu s$ ). (b) The  $t_0$  distribution of subtracting the background region from the signal region. The region between the red lines ( $[0.7, 1.0] \mu s$ ) is selected.

## Pile-up effect

Pile-up occurs due to the multiple spallation neutrons generated from one cosmic ray muon. When one cosmic ray muon passes through the SK tank, 1 to about 60 neutrons are produced. The pile-up effect overestimates the reconstructed energy, so this effect must be considered when evaluating the energy of spallation neutron captures on gadolinium.

To evaluate the pile-up effect, the neutron multiplicity by one muon event is counted first. The distribution of  $N_{50}$  after the above event selection cuts is shown in Figure 4.13. Excluding obvious background events under condition  $18 < N_{50} < 70$  [57], sub-events (spallation neutron candidates) due to one muon event are counted. The distribution of the number of neutron events per one muon event is shown in Figure 4.14. Then, the mean  $N_{50}$  for each neutron multiplicity is checked. The mean  $N_{50}$  is determined by the following steps.

1. Fit the  $N_{50}$  distribution with the Gaussian function three times.
2. The mean value of the final fit is used as the mean  $N_{50}$ .

The Gaussian function used for the fitting is

$$f(x) = a \exp\left(-\frac{(x - \mu)^2}{2\sigma^2}\right), \quad (4.11)$$

where  $a$  is constant,  $\mu$  is the mean and  $\sigma$  is the standard deviation. The fitting ranges for each fitting are shown in Table 4.2. The reason why the  $N_{50}$  histogram is fitted three

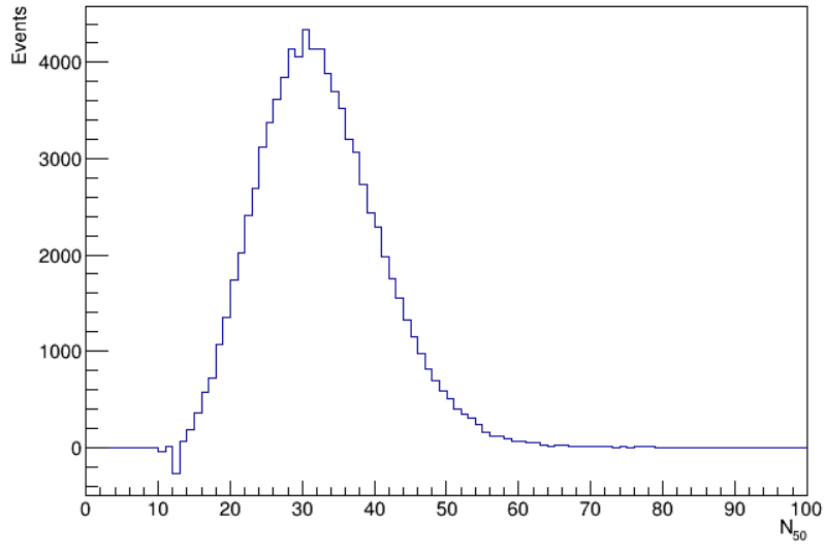


Figure 4.13: The  $N_{50}$  distribution using the fiducial volume cut, reconstruction quality cut,  $L_t$  cut, reconstructed time cut, and background signal reduction.

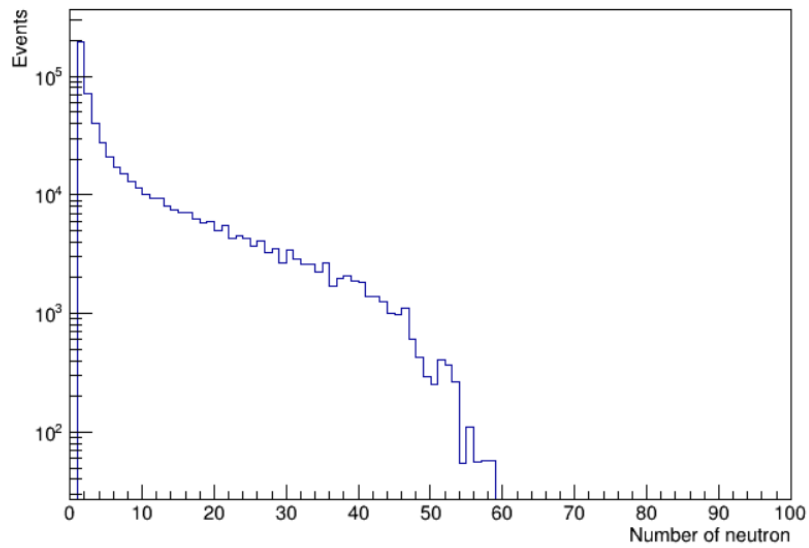


Figure 4.14: The distribution of the number of spallation neutrons produced by one cosmic ray muon.

times is to remove the effect of the trigger threshold and to fit more accurately. The distribution of  $N_{50}$  and the result of fitting when the neutron multiplicity is 1 is shown in Figure 4.15.

Number of times	Range of fit
1st	$20 < N_{50} < 50$
2nd	$[\mu - 0.4 \times \sigma, \mu + 1.5 \times \sigma]$
3rd	$[\mu - 0.7 \times \sigma, \mu + 1.5 \times \sigma]$

Table 4.2: Number of fit and fit range.

The relationship between mean  $N_{50}$  and the number of neutrons produced is shown in Figure 4.16. The larger the neutron multiplicity is, the larger the mean  $N_{50}$  is due to the pile-up effect. When multiple events occur in a single trigger time window, the one with the greater number of hits is more likely to be selected as the signal (Figure 4.17). Therefore, the greater the neutron multiplicity is, the more likely it is that signals with greater energy will be selected, and the mean  $N_{50}$  value will also increase.

To reduce the pile-up effect, the neutron multiplicity selection is set by considering

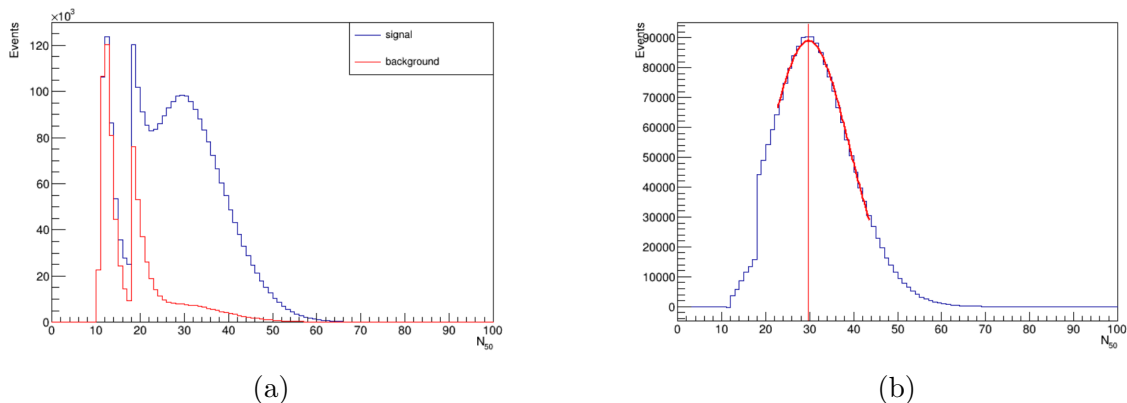


Figure 4.15: (a) The  $N_{50}$  distribution for 1 neutron multiplicity in the signal region ( $[35, 235] \mu s$ ) and the background region ( $[335, 535] \mu s$ ). The blue line represents the signal region and the red line represents the background region. (b) The  $N_{50}$  distribution for 1 neutron multiplicity. This distribution is obtained by subtracting the background region from the signal region. The red curve represents the result of the third fitting and the red line represents the mean  $N_{50}$ . The mean  $N_{50}$  for 1 neutron is  $29.74 \pm 0.02$ .

relative difference of  $N_{50}$  from the  $n = 1$  case (Figure 4.18). 1 to 3 of neutron multiplicity is used so that the deviation is within 0.5 %. Therefore the multiplicity selection is the following.

$$n = [1, 3] \quad (4.12)$$

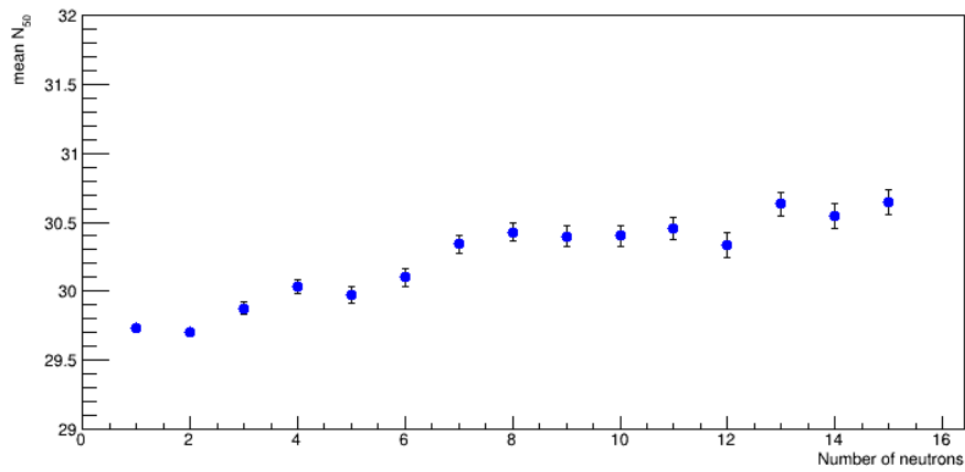


Figure 4.16: The pile-up effect of the neutron multiplicity. The horizontal axis represents the neutron multiplicity. The vertical axis represents the mean  $N_{50}$  for each neutron multiplicity.

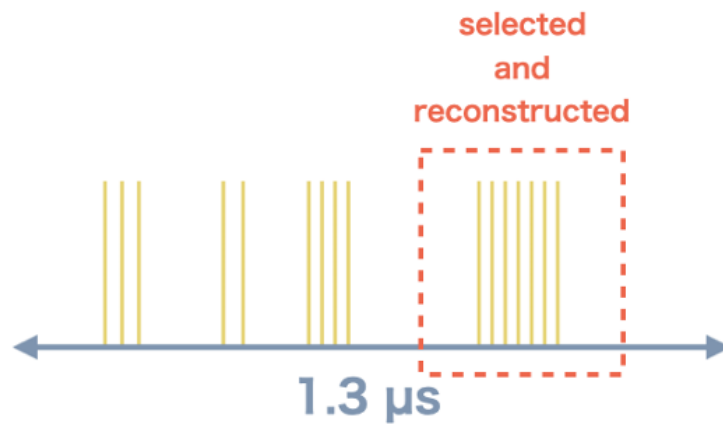


Figure 4.17: The illustration of the selection of the sub-events. In the sub-trigger time window ( $1.3 \mu s$ ), the largest signal is selected as the sub-event. The yellow lines represent the PMT hits.

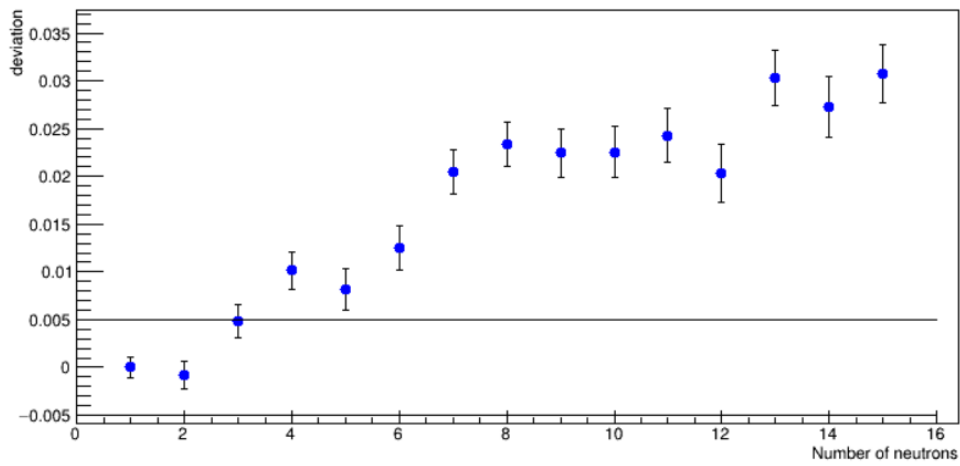


Figure 4.18: The deviation of the pile-up effect. The black line represents  $\pm 0.5 \%$ .

### 4.3.3 Summary of event selection

The event selections for spallation neutron captures on gadolinium are summarized in Table 4.3.

Time window	AFT trigger ( $[35, 535] \mu\text{s}$ )
Fiducial volume cut	Events in the fiducial volume are used.
Reconstruction quality cut	$(g_{vtx} > 0.4) \wedge (g_{dir} < 0.4)$
$L_t$ cut	$L_t < 300 \text{ cm}$
Reconstructed time cut	$t_0 = [0.7, 1.0] \mu\text{s}$
multiplicity cut	$n = [1, 3]$
Signal region	$[35, 235] \mu\text{s}$
Background region	$[335, 535] \mu\text{s}$

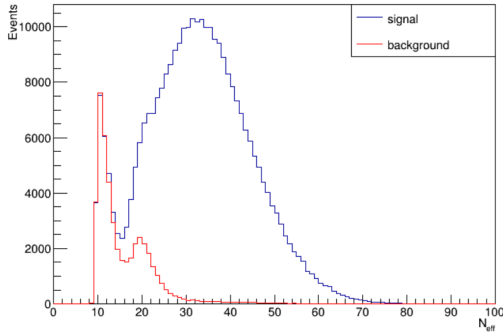
Table 4.3: The summary of the event selections for spallation neutron captures on gadolinium.  $L_t$  is the distance between a muon track and a reconstructed event point.  $t_0$  is the reconstructed time.  $n$  is the neutron multiplicity.

## 4.4 Evaluation of mean $N_{\text{eff}}$ and energy

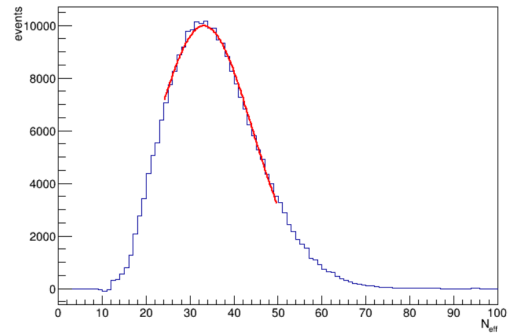
As described in Section 3.3.3, in the low energy region, effective PMT hits  $N_{\text{eff}}$  is calculated from  $N_{50}$  using some parameters. Then the energy of the event is reconstructed using the function of  $N_{\text{eff}}$ . To evaluate these quantities, mean  $N_{\text{eff}}$  and mean energy is defined in our study. These values are similar to mean  $N_{50}$  in Section 4.3.2. The steps to obtain these values are the same as Table 4.2 and Eq. (4.11). Figure 4.19 and Figure 4.20 show the  $N_{\text{eff}}$  and energy distribution of spallation neutron captures on gadolinium for real data of SK-VII. These distributions are obtained using the event selections described in the above sections. The fitting ranges for each fitting are shown in Table 4.4. In the following chapter, these mean  $N_{50}$ ,  $N_{\text{eff}}$ , and energy are used to evaluate the SK detector performance.

Number of times	Range of fit	
	$N_{\text{eff}}$	Energy [MeV]
1st	$[20, 50]$	$[4, 6]$
2nd	$[\mu - 0.4 \times \sigma, \mu + 1.5 \times \sigma]$	$[\mu - 0.4 \times \sigma, \mu + 1.5 \times \sigma]$
3rd	$[\mu - 0.7 \times \sigma, \mu + 1.5 \times \sigma]$	$[\mu - 0.7 \times \sigma, \mu + 1.5 \times \sigma]$

Table 4.4: Number of fit and fit range.

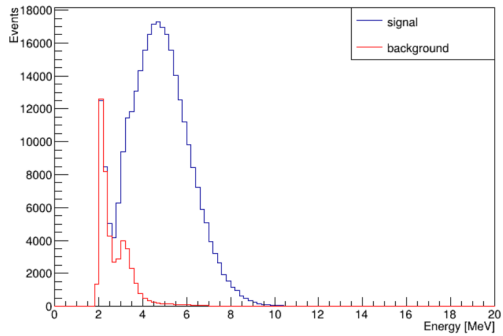


(a)

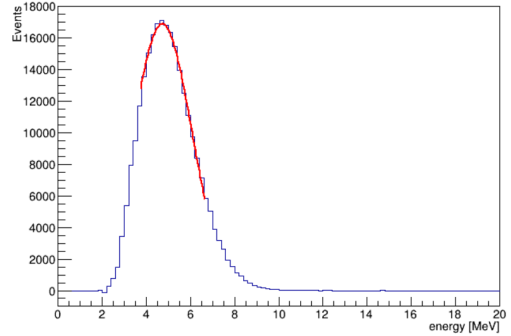


(b)

Figure 4.19: (a) The  $N_{\text{eff}}$  distribution of spallation neutron captures on Gd in the signal region ( $[35, 235] \mu\text{s}$ ) and the background region ( $[335, 535] \mu\text{s}$ ). The blue line represents the signal region and the red line represents the background region. The event selections are applied to the data. (b) The  $N_{\text{eff}}$  distribution of spallation neutron captures on Gd. This distribution is obtained by subtracting the background region from the signal region. The red curve represents the final Gaussian fit and the mean value of this fit is used as the mean  $N_{\text{eff}}$ .



(a)



(b)

Figure 4.20: (a) The energy distribution of spallation neutron captures on Gd in the signal region ( $[35, 235] \mu\text{s}$ ) and the background region ( $[335, 535] \mu\text{s}$ ). The blue line represents the signal region and the red line represents the background region. The event selections are applied to the data. (b) The energy distribution of spallation neutron captures on Gd. This distribution is obtained by subtracting the background region from the signal region. The red curve represents the final Gaussian fit and the mean value of this fit is used as the mean energy.

# Chapter 5

## Monte Carlo simulation

To evaluate the position dependence of the detector using spallation neutron captures on gadolinium, the data is compared with the Monte Carlo simulation. Also, the simulation of the spallation neutron captures on Gd is compared with the simulation of the low-energy electrons to check the nature of the neutron captures. In this section, the MC generation and event selection for MC are explained.

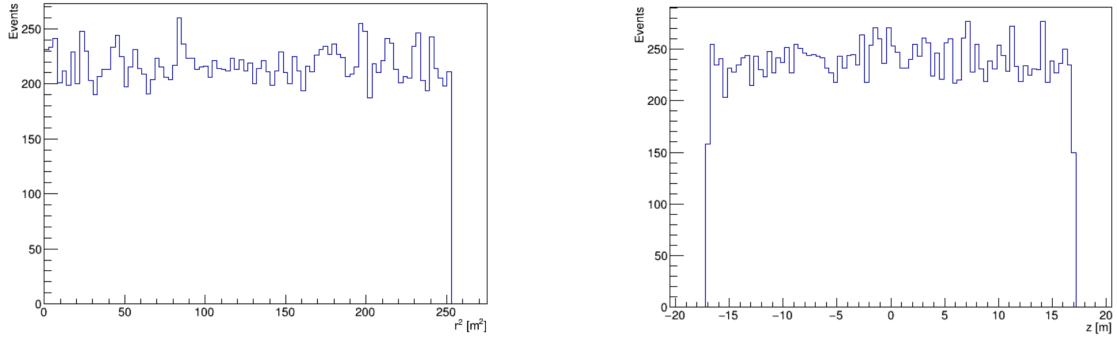
### 5.1 Software for Monte Carlo simulation

The Geant4-based Monte Carlo simulation package called SKG4 [58] is used. It can simulate particle interactions and responses of the SK detector. The output of SKG4 contains the same format as real data, so it can be analyzed in the same way as the real data. In our study, neutrons and electrons are generated using SKG4 and neutron captures on Gd and Cherenkov lights from electrons are simulated. The ANNRI-Gd model [59] is adopted as the model for  $\text{Gd}(n, \gamma)$ . Also, a C++ library is used to add some noises to the MC simulation. These noises are extracted from the data files. The software trigger is applied to the MC file. The thresholds of the SLE, LE, and HE trigger are set to 20, 30, and 40 for the neutron MC. For the electron MC, they are set to 34, 49, and 52, respectively. Then, the triggered events are reconstructed the same as the real data.

### 5.2 Production of the simulated events

The process of MC generation is below.

1. Generate neutrons (electrons) 1 m inside the wall of the ID uniformly. The energy of a neutron (electron) is set to 200 keV (4~7 MeV). One neutron (electron) is generated per event. The distribution of neutrons is shown in Figure 5.1. After neutron thermalization is simulated, the neutron is captured by gadolinium and gamma rays are emitted.
2. Add noise hits on PMTs to the resulting output. This noise is based on the noise data, such as PMT dark rate.
3. Apply the sub-trigger to the noise-added output and save the sub-events.



(a)  $r^2$  distribution of produced neutrons.

(b)  $z$  distribution of produced neutrons.

Figure 5.1: The distribution of produced neutrons.

#### 4. Perform the event reconstruction.

The water parameters, which reproduce the water quality and are used for the calculation of  $N_{\text{eff}}$ , are the values given in from Section 3.2.1 to Section 3.2.3. In this simulation, since neutrons are captured after the thermalization, it is valid to generate neutrons with a single energy.

## 5.3 Event selection for MC

### 5.3.1 Event selection conditions

The event selection for the neutron MC is almost the same as the real data. However, because muon events are not simulated in MC, the event selection of distance between the muon track and reconstructed event point ( $L_t$  cut) is not applied for MC. The distribution of each selection for MC is below.

#### dt distribution and time window

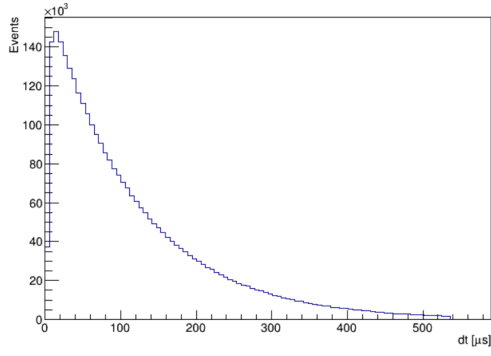
The dt is the time between when a neutron is produced and when it is captured by gadolinium. The dt distribution for SK-VI and SK-VII period is shown in Figure 5.2. The time constant is  $116.42 \mu\text{s}$  for SK-VI and  $59.71 \mu\text{s}$  for SK-VII. These values match the expected values. To keep consistent with the time window of data,  $[35, 535] \mu\text{s}$  time window is used in MC as well. The signal region is set to  $[35, 235] \mu\text{s}$ , and the background region is set to  $[335, 535] \mu\text{s}$ .

#### Reconstruction quality

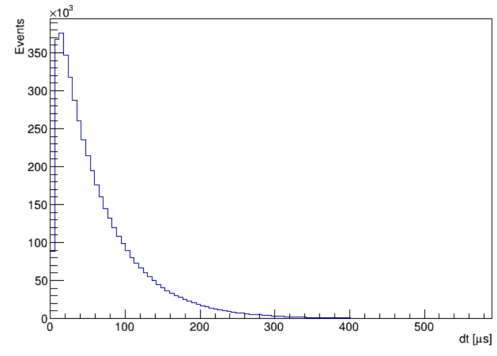
The distributions of the reconstruction qualities  $g_{vtx}$  and  $g_{dir}$  are shown in Figure 5.3 and Figure 5.4 respectively. Only the fiducial volume cut is applied to the generated MC data. Same as data, the selection conditions of  $g_{vtx}$  and  $g_{dir}$  are set as follows.

$$(g_{vtx} > 0.4) \wedge (g_{dir} < 0.4) \quad (5.1)$$

From Figure 5.3a and Figure 5.4a, because only neutron events are simulated, there are few events in the background region. For  $g_{vtx}$  distribution (Figure 5.3b), only one peak above 0.4 exists in MC, while there are two other peaks below 0.4 in data (Figure 4.8b).

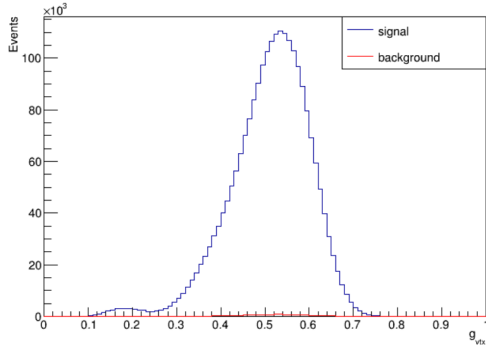


(a) SK-VI

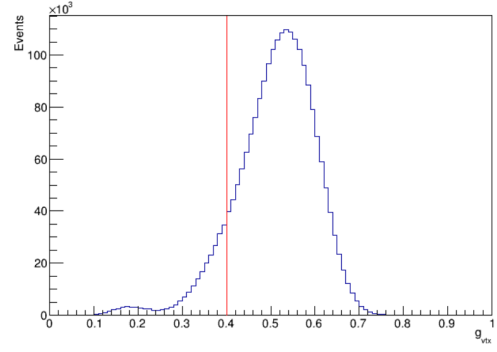


(b) SK-VII

Figure 5.2: The  $dt$  distribution of neutron capture events in SK-VI and SK-VII period.

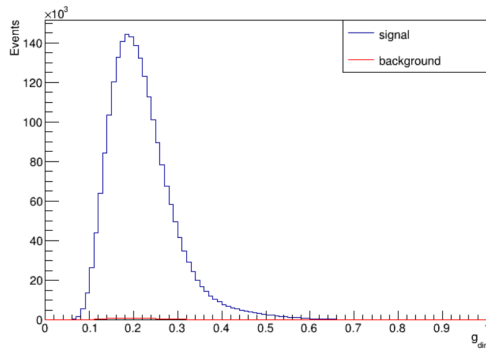


(a)

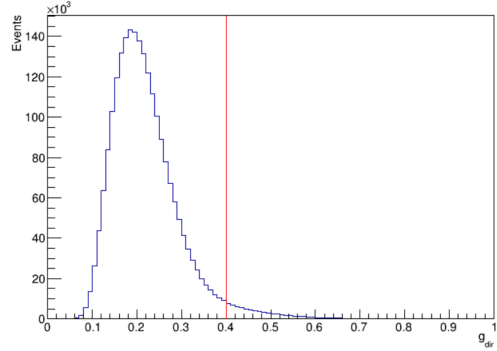


(b)

Figure 5.3: (a) The  $g_{vtx}$  distribution in the signal region ( $[35, 235] \mu s$ ) and the background region ( $[335, 535] \mu s$ ). The blue line represents the signal region ( $[35, 235] \mu s$ ) and the red line represents the background region ( $[335, 535] \mu s$ ). (b) The  $g_{vtx}$  distribution of subtracting the background region from the signal region. The right side of the red line ( $g_{vtx} > 0.4$ ) is selected.



(a)



(b)

Figure 5.4: (a) The  $g_{dir}$  distribution in the signal region ( $[35, 235] \mu s$ ) and the background region ( $[335, 535] \mu s$ ). The blue line represents the signal region ( $[35, 235] \mu s$ ) and the red line represents the background region ( $[335, 535] \mu s$ ). (b) The  $g_{dir}$  distribution of subtracting the background region from the signal region. The left side of the red line ( $g_{dir} < 0.4$ ) is selected.

Therefore, those two peaks below 0.4 are figured out to be background signals.

## Reconstructed event time

The reconstructed event time  $t_0$  distribution is shown in Figure 5.5. The fiducial volume cut and reconstruction quality cut are applied to the MC data. Same as real data, the selection condition is set as follows.

$$t_0 = [0.7, 1.0]\mu s \quad (5.2)$$

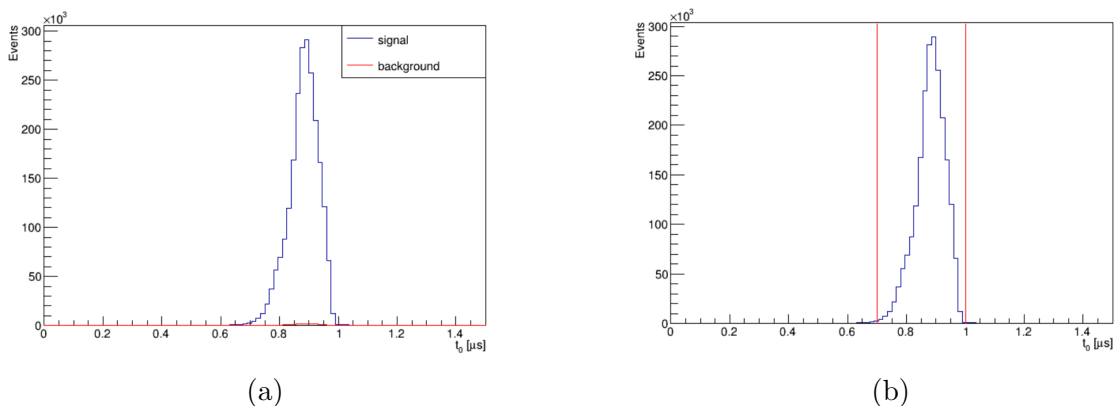


Figure 5.5: (a) The  $t_0$  distribution in the signal region and background region. The blue line represents the signal region ( $[35, 235] \mu s$ ) and the red line represents the background region ( $[335, 535] \mu s$ ). (b) The  $t_0$  distribution of subtracting the background region from the signal region. The area between the red lines ( $0.7 < t_0 < 1.0$ ) is selected.

### 5.3.2 Summary of event selection

The event selections for the neutron MC are summarized in Table 5.1. For the electron MC, the fiducial volume cut, the reconstruction quality cut, and the reconstructed time cut are applied.

Time window	AFT trigger ( $[35, 535] \mu s$ )
Fiducial volume cut	Events in the fiducial volume are used.
Reconstruction quality cut	$(g_{vtx} > 0.4) \wedge (g_{dir} < 0.4)$
Reconstructed time cut	$t_0 = [0.7, 1.0]\mu s$
multiplicity cut	$n = [1, 3]$
Signal region	$[35, 235] \mu s$
Background region	$[335, 535] \mu s$

Table 5.1: The summary of the event selections for MC.  $t_0$  is the reconstructed time.  $n$  is the neutron multiplicity.

# Chapter 6

## Energy scale calibration with spallation neutron capture signal

In this chapter, the energy calibration using spallation neutrons is discussed. Firstly, the position dependence in the SK-VI and SK-VII period is assessed by comparing the  $\text{Gd}(n, \gamma)$  signals of data and MC. Then, the time variation through the SK-VI and SK-VII periods is evaluated.

### 6.1 Evaluation of position dependence of the SK detector

Solar neutrinos and DSNB are the main targets for low-energy region measurement at Super-Kamiokande. The primary signals for these events are electrons and positrons. In SK, some calibrations, such as LINAC and DT calibration, use electrons. However, these calibrations can measure the limited area, and it is difficult to evaluate the position dependence in detail. On the other hand, the spallation neutron captures on gadolinium can be observed throughout the entire detector. Therefore, this method has the advantage of evaluating the detailed position dependence. However, this method also has the disadvantage that  $\gamma$  rays are difficult to detect because the detected energy is low and close to the trigger threshold (Section 4.2.2).

In this section, the position dependence of the energy scale is discussed by comparing the data and MC of spallation neutron captures on gadolinium signals. The data from February 15, 2022, to March 15, 2022 is used to represent the SK-VI period. The data from January 15, 2023, to February 13, 2023 is used to represent the SK-VII period. The SK-VI and SK-VII MC were created using the water quality information in the same period. The simulations were generated as described in Chapter 5. Also, the position dependence of the electron MC energy scale is compared with the spallation neutron MC to check the cause of the position dependence.

### 6.1.1 Position dependence of energy in SK-VI and SK-VII periods

To evaluate the position dependence of the spallation neutron captures on Gd, the detector is divided into five regions for each  $r^2$ - and  $z$ -direction shown in Figure 6.1. The position dependence of the detector's energy scale is evaluated using the mean energy (Section 4.4) of the data and the MC. The energy distribution and the fitting result in each area is shown in Figure 6.2. The mean energy in each area for the data and MC is shown in Figure 6.3. Figure 6.3a shows the mean energies in the  $r^2$ -direction division areas and Figure 6.3b shows the those in the  $z$ -direction division areas.

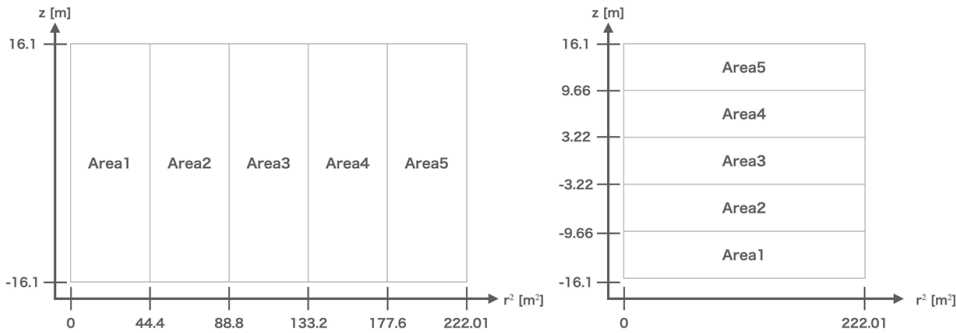


Figure 6.1: The detector is divided into five regions in the  $r^2$ -direction (left) and in the  $z$ -direction (right).

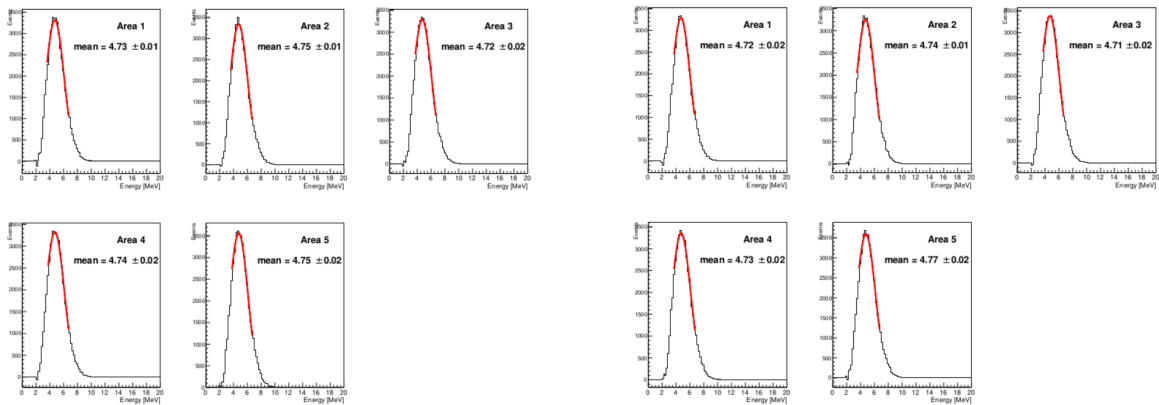
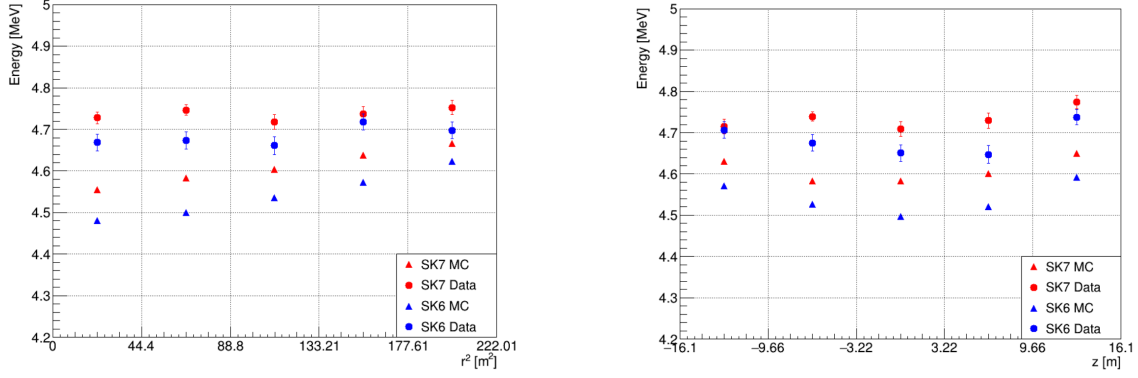


Figure 6.2: The energy distributions and the Gaussian fitting results for SK-VII. The left figure represents the  $r^2$ -direction division areas. The right one represents the  $z$ -direction division areas. The red curves represent the fitting results.

The average values of the mean energy for each analysis are summarized in Table 6.1. For the data analysis, the difference between SK-VI and SK-VII average mean energy is about 1.2 %. For MC analysis, the difference between SK-VI and SK-VII average mean energy is about 1.5 %. These results indicate that there may be some differences in SK-VI and SK-VII analysis, such as the measurements of the water quality parameters. This is discussed in Section 6.2. Also, there is about 3 % difference in the MC and data



(a) The mean energies in the  $r^2$ -direction.

(b) The mean energies in the  $z$ -direction.

Figure 6.3: The mean energies of the data and MC for SK-VI and SK-VII. The blue dots represent SK-VI and the red dots represent SK-VII. The circle dots represent the real data and the triangle dots represent the MC.

analysis for both SK-VI and SK-VII. This may be due to the uncertainty of the  $Gd(n,\gamma)$  model implemented in the simulation, so it is not discussed in this study. Then, a relative difference of the energy scale,  $\text{diff}_{\text{pos}}$ , is used to evaluate the size of position dependence of the mean energy.  $\text{diff}_{\text{pos}}$  is expressed as follows.

$$(\text{diff}_{\text{pos}})_i = \frac{(\text{energy})_i}{(\text{energy})_{\text{ave}}} \quad (6.1)$$

Where  $(\text{energy})_i$  is the mean energy in each area and  $(\text{energy})_{\text{ave}}$  is the average mean energy. Figure 6.4 and Figure 6.5 show the  $\text{diff}_{\text{pos}}$  in the  $r^2$ -direction and the  $z$ -direction for SK-VI and SK-VII, respectively.

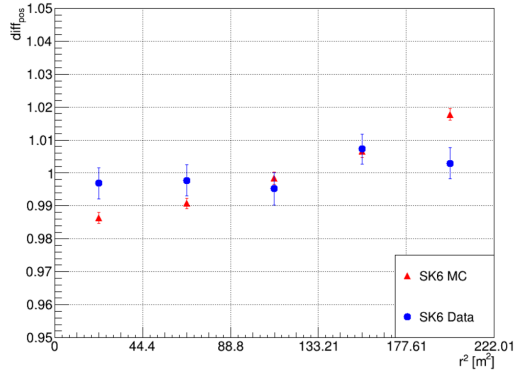
	$r^2$ -direction	$z$ -direction
SK-VI MC	$4.542 \pm 0.051$ (1.12 %)	$4.541 \pm 0.035$ (0.77 %)
SK-VI data	$4.683 \pm 0.021$ (0.45 %)	$4.683 \pm 0.034$ (0.73 %)
SK-VII MC	$4.609 \pm 0.040$ (0.86 %)	$4.609 \pm 0.026$ (0.58 %)
SK-VII data	$4.737 \pm 0.013$ (0.26 %)	$4.734 \pm 0.023$ (0.49 %)

Table 6.1: The average values of the mean energy for each analysis. The numbers in brackets are the coefficients of variation (CV).

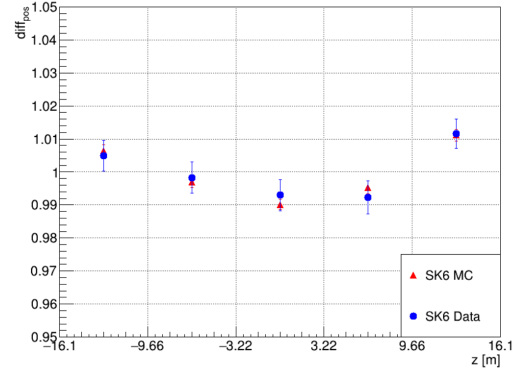
From Table 6.1, the  $\text{diff}_{\text{pos}}$  of the data is smaller than that of the MC for both SK-VI and SK-VII. Then, a relative difference of position dependence is evaluated by taking a double ratio of relative position dependence for MC and data.

$$\text{DR}_{\text{MC,data}} = \frac{(\text{MC})_i / (\text{MC})_{\text{ave}}}{(\text{data})_i / (\text{data})_{\text{ave}}} \quad (6.2)$$

where  $(\text{MC})_i$  and  $(\text{data})_i$  are the mean energy in each area for the MC and the data, respectively.  $(\text{MC})_{\text{ave}}$  and  $(\text{data})_{\text{ave}}$  are the average mean energy for the MC and the

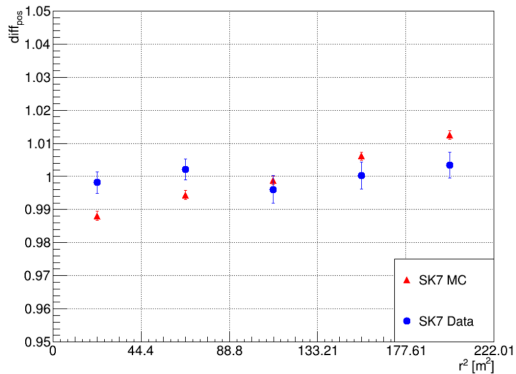


(a) The  $\text{diff}_{\text{pos}}$  of the mean energy in the  $r^2$ -direction.

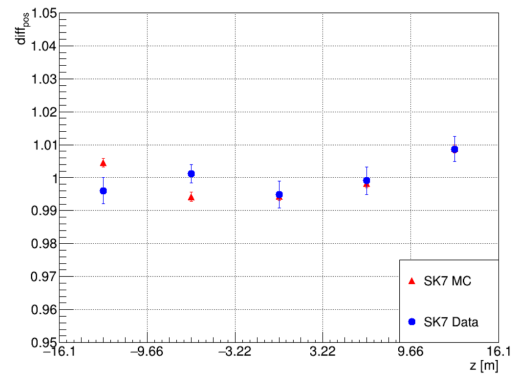


(b) The  $\text{diff}_{\text{pos}}$  of the mean energy in the  $z$ -direction.

Figure 6.4: The  $\text{diff}_{\text{pos}}$  of the data and MC for SK-VI. The blue dots represent the data and the red dots represent the MC.

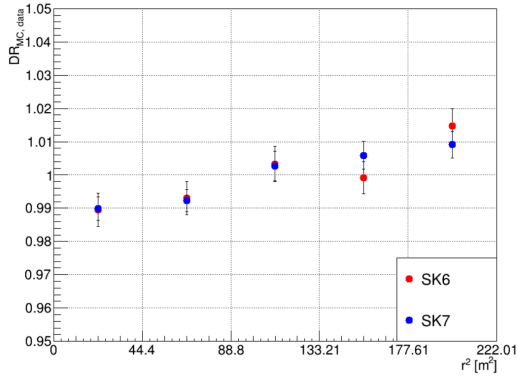


(a) The  $\text{diff}_{\text{pos}}$  of the mean energy in the  $r^2$ -direction.

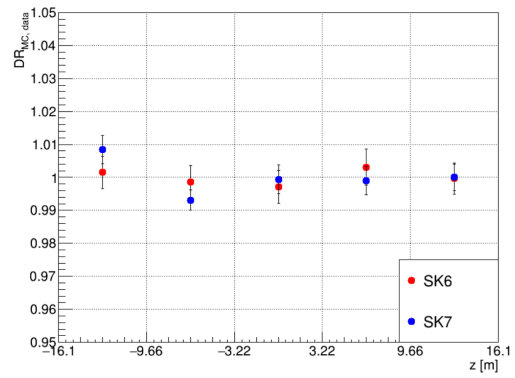


(b) The  $\text{diff}_{\text{pos}}$  of the mean energy in the  $z$ -direction.

Figure 6.5: The  $\text{diff}_{\text{pos}}$  of the data and MC for SK-VII. The blue dots represent the data and the red dots represent the MC.



(a) The  $r^2$  position dependence.



(b) The  $z$  position dependence.

Figure 6.6: The position dependence in the  $r^2$ -direction and the  $z$ -direction for SK-VI and SK-VII. The red dots represent the SK-VI result and the blue dots represent the SK-VII result.

data. Figure 6.6a shows the  $r^2$ -position dependence of the mean energy for SK-VI and SK-VII. Figure 6.6b shows the  $z$ -position dependence for SK-VI and SK-VII.

We found that the relative difference of the position dependences in the  $r^2$ -direction for SK-VI and SK-VII are 0.88 % and 0.76 %, respectively. Those in the  $z$ -direction for SK-VI and SK-VII are 0.21 % and 0.49 %. The  $z$ -direction position dependences for both SK-VI and SK-VII are good enough compared to the goal of the correction within 0.5 %. On the other hand, the  $r^2$ -direction position dependences are larger than the goal. We found that the CV of the MC for the  $r^2$  division is much larger than the data (Table 6.1). To check the  $\text{diff}_{\text{pos}}$  of the MC more precisely, this neutron capture MC is compared with the electron MC in the next section.

### 6.1.2 Comparison of the neutron and electron simulation

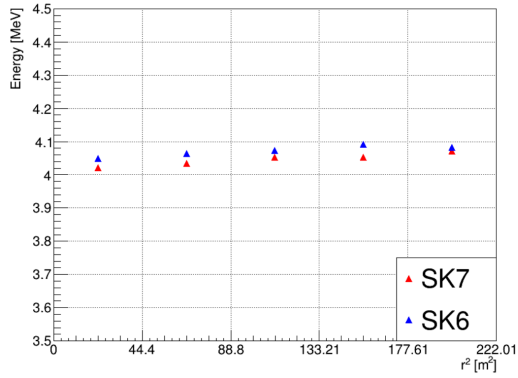
To check the cause of the neutron captures on Gd MC's large position dependence, the electron MC is compared with the neutron MC. Firstly, the kinetic energy of the electron is set to 4 MeV, which is the similar energy of the neutron captures on Gd. The position dependences of both MC are evaluated in the same way as the last section. The mean energy of the electron MC in each area is shown in Figure 6.7. That of the neutron MC is shown in Figure 6.3.

The average mean energies of the electron MC are summarized in Table 6.2.

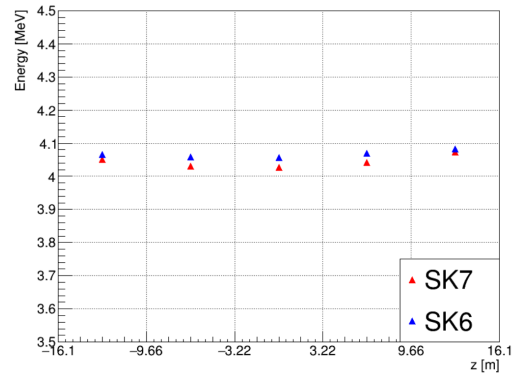
	$r^2$ -direction	$z$ -direction
SK-VI	$4.073 \pm 0.015$ (0.37 %)	$4.067 \pm 0.009$ (0.22 %)
SK-VII	$4.047 \pm 0.017$ (0.42 %)	$4.045 \pm 0.016$ (0.40 %)

Table 6.2: The average values of the mean energy for the electron MC in SK-VI and SK-VII. The numbers in brackets are the coefficients of variation (CV).

The difference of the average mean reconstructed energy of the electron MC between SK-VI and SK-VII is about 0.6 %, while that for the neutron MC is about 1.5 % (Ta-



(a) The mean energy in the  $r^2$ -direction for the SK-VI and SK-VII electron MC.

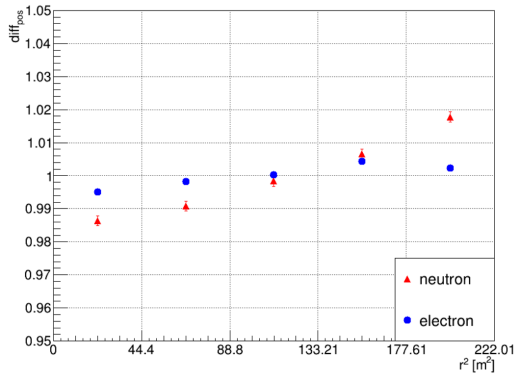


(b) The mean energy in the  $z$ -direction for the SK-VI and SK-VII electron MC.

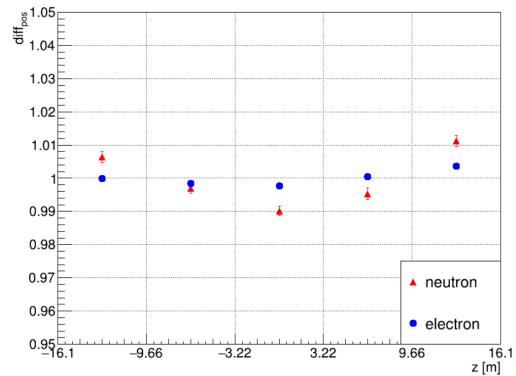
Figure 6.7: The mean energy in each area for the SK-VI and SK-VII electron MC. The blue dots represent SK-VI and the red dots represent SK-VII.

ble 6.1 and Table 6.2). From this result, there may be some problems with the energy reconstruction of the neutron captures MC. The energy of SK-VI MC may be underestimated or that of SK-VII MC may be overestimated.

Figure 6.8 shows the  $\text{diff}_{\text{pos}}$  (Eq. (6.1)) for the SK-VI neutron and electron MC and Figure 6.9 shows that for the SK-VII neutron and electron MC. The standard deviations of the  $\text{diff}_{\text{pos}}$  for each analysis are summarized in Table 6.3.



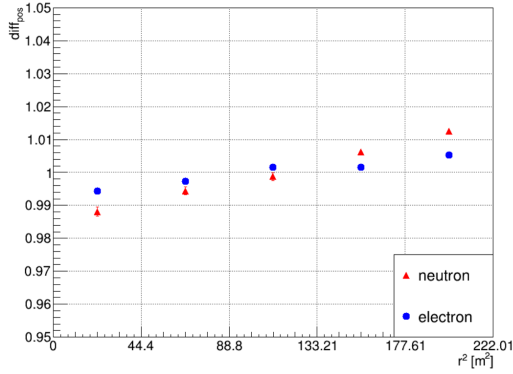
(a) The  $\text{diff}_{\text{pos}}$  of the mean energy in the  $r^2$ -direction for the SK-VI MC.



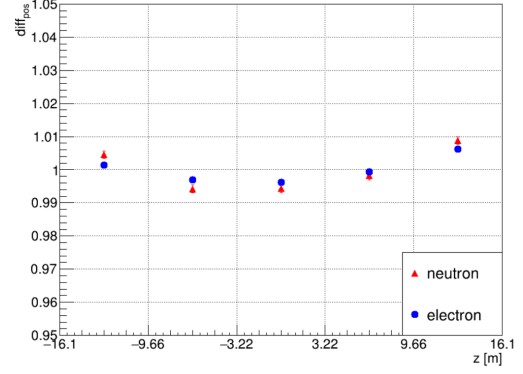
(b) The  $\text{diff}_{\text{pos}}$  of the mean energy in the  $z$ -direction for the SK-VI MC.

Figure 6.8: The  $\text{diff}_{\text{pos}}$  of the mean energy for the SK-VI electron and neutron MC. The blue dots represent the electron MC and the red dots represent the neutron MC.

The  $\text{diff}_{\text{pos}}$  of the electron MC is within about  $\pm 0.5\%$  in both  $r^2$ - and  $z$ -direction. For the  $r^2$ -direction, the  $\text{diff}_{\text{pos}}$  of the SK-VII neutron MC is about within  $\pm 1.5\%$  (Figure 6.9), while that of the SK-VI neutron MC is within  $\pm 2\%$  (Figure 6.8). From Table 6.3, the standard deviation of the neutron MC is larger than the electron MC, especially for the  $r^2$  division analysis. The difference in the  $\text{diff}_{\text{pos}}$  between the electron and neutron MC is shown in Figure 6.10.



(a) The  $\text{diff}_{\text{pos}}$  of the mean energy in the  $r^2$ -direction for the SK-VII MC.

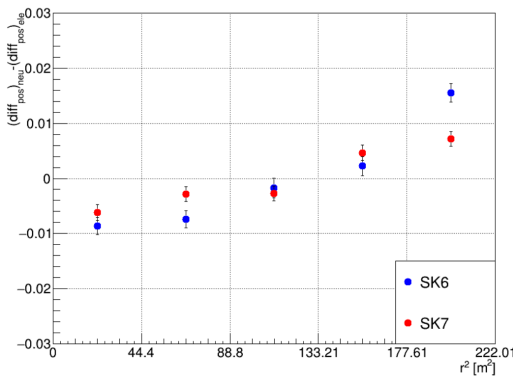


(b) The  $\text{diff}_{\text{pos}}$  of the mean energy in the  $z$ -direction for the SK-VII MC.

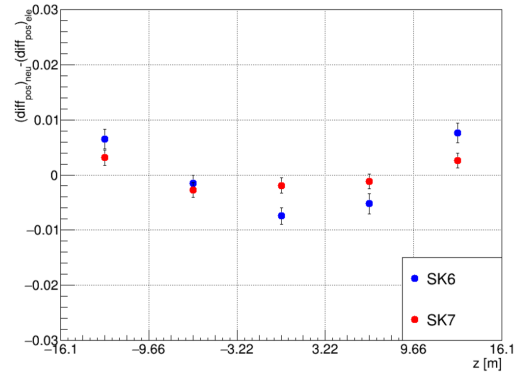
Figure 6.9: The  $\text{diff}_{\text{pos}}$  of the mean energy for the SK-VII electron and neutron MC. The blue dots represent the electron MC and the red dots represent the neutron MC.

	electron MC		neutron MC	
	SK-VI	SK-VII	SK-VI	SK-VII
$r^2$ -direction	0.32 %	0.38 %	1.12 %	0.86 %
$z$ -direction	0.21 %	0.36 %	0.77 %	0.58 %

Table 6.3: The standard deviation of the  $\text{diff}_{\text{pos}}$  for the electron and neutron MC.



(a) The subtraction of the  $\text{diff}_{\text{pos}}$  of the neutron MC from that of the electron MC in the  $r^2$ -direction.



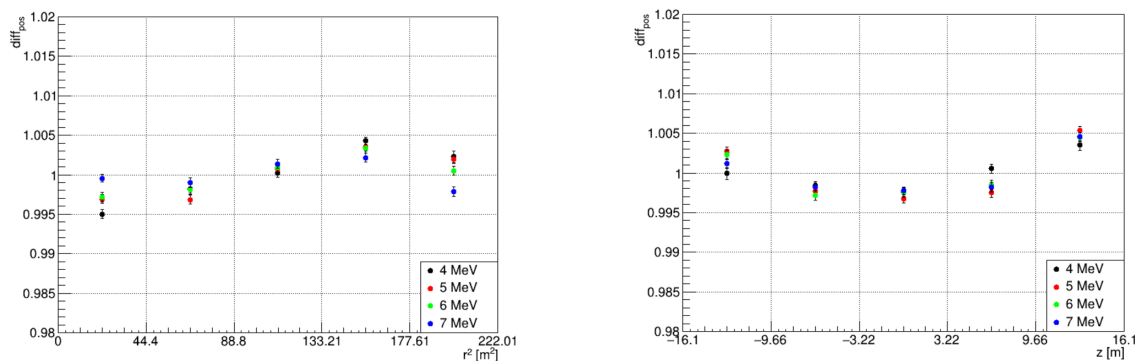
(b) The subtraction of the  $\text{diff}_{\text{pos}}$  of the neutron MC from that of the electron MC in the  $z$ -direction.

Figure 6.10: The subtraction from the  $\text{diff}_{\text{pos}}$  of the neutron MC from that of the electron MC. The blue dots represent the SK-VI MC, and the red dots represent the SK-VII MC.

The SK-VII neutron and electron MC are consistent within about  $\pm 1\%$ , while the SK-VI MC are consistent within about  $\pm 2\%$  for the  $r^2$ -direction. For the z-direction, the SK-VII MC are consistent within about  $\pm 0.5\%$ , while the SK-VI MC are consistent within about  $\pm 1\%$ . These differences may be caused by the problems unique to the neutron MC, and it is necessary to understand this cause.

We found the  $\text{diff}_{\text{pos}}$  of the electron MC changes when the energy of the generated electron changes from 4 MeV to 7 MeV. The  $\text{diff}_{\text{pos}}$  for each energy electron is shown in Figure 6.11 and 6.12. Especially for the  $r^2$ -direction analysis, we found that the energies in the inner region get smaller. Also, for the  $r^2$  division, the  $\text{diff}_{\text{pos}}$  in the outermost area is smaller than that in the second outermost area for the higher electron energy events. This is due to a multiple-pe effect. In the low-energy region, it is assumed that one photon hits one PMT and the energy of an event is reconstructed by the number of hit PMTs. However, one PMT detects the multiple photons from the event in the outermost area, and the number of PMT hits decreases (the multiple-pe effect).

The relationship between the relative difference of the  $\text{diff}_{\text{pos}}$  and the electron energy is shown in Figure 6.13. Here, the relative difference of the  $\text{diff}_{\text{pos}}$  is estimated as the standard deviation of the  $\text{diff}_{\text{pos}}$ .

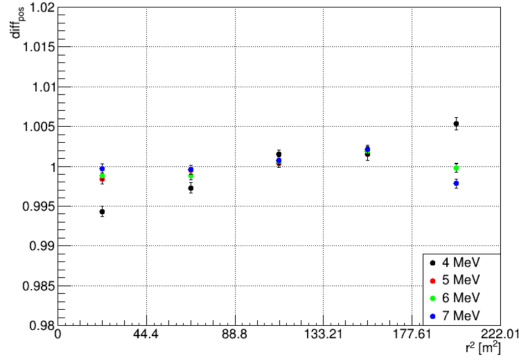


(a) The  $\text{diff}_{\text{pos}}$  in the  $r^2$ -direction of each electron energy for SK-VI.

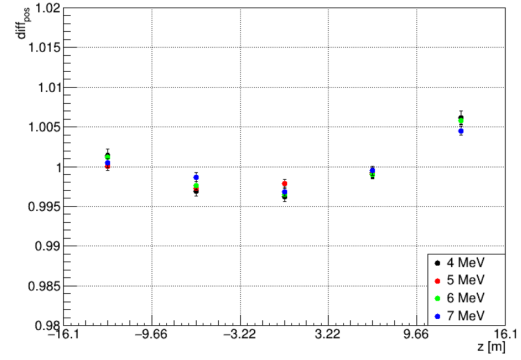
(b) The  $\text{diff}_{\text{pos}}$  in the z-direction of each electron energy for SK-VI.

Figure 6.11: The  $\text{diff}_{\text{pos}}$  of each electron energy for the SK-VI electron MC.

The standard deviation of the  $\text{diff}_{\text{pos}}$  increases as the energy of the generated electron gets small for both the  $r^2$ -direction and the z-direction and both SK-VI and SK-VII. Therefore, we found that the position dependence of the energy scale depends on the energy of an event in MC. Because the energy of the scattered electron from the gamma ray generated by the spallation neutron captures on Gd is smaller than 4 MeV (Figure 6.14), the energy dependence of the position dependence may have larger effects on the neutron MC and may explain the difference between electrons and neutrons. It needs further investigation to understand the cause of this energy dependence.

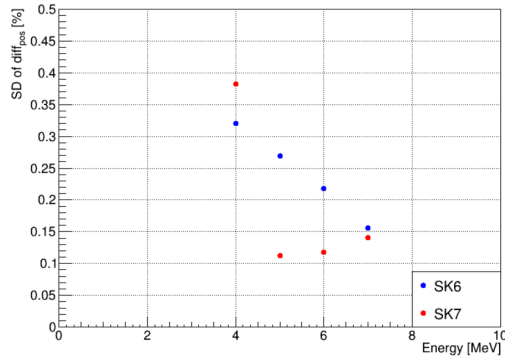


(a) The  $\text{diff}_{\text{pos}}$  in the  $r^2$ -direction of each electron energy for SK-VII.

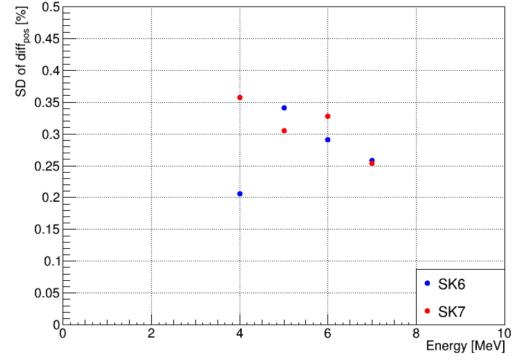


(b) The  $\text{diff}_{\text{pos}}$  in the  $z$ -direction of each electron energy for SK-VII.

Figure 6.12: The  $\text{diff}_{\text{pos}}$  of each electron energy for the SK-VII electron MC.



(a) The relationship between the standard deviation of the  $\text{diff}_{\text{pos}}$  in the  $r^2$ -direction and the electron energy.



(b) The relationship between the standard deviation of the  $\text{diff}_{\text{pos}}$  in the  $z$ -direction and the electron energy.

Figure 6.13: The relationship between the deviation and the electron energy for the SK-VI and SK-VII MC. The blue dots represent the SK-VI MC and the red dots represent the SK-VII MC.

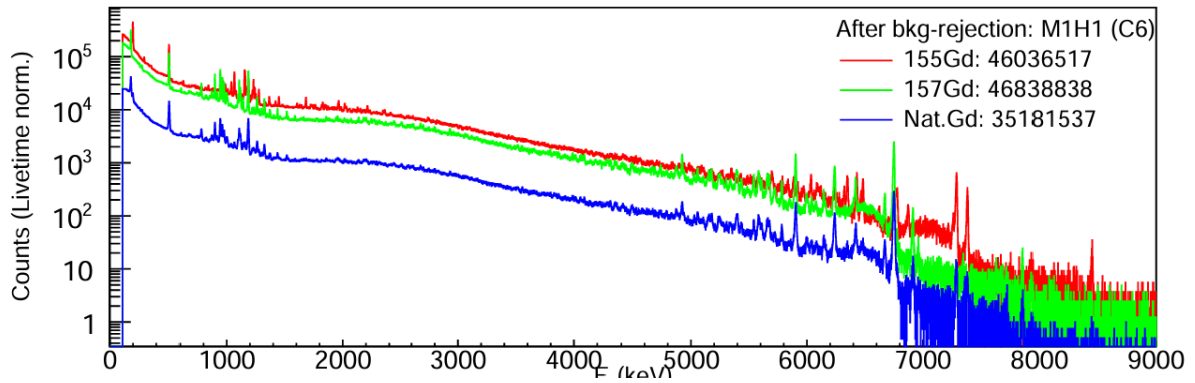


Figure 6.14: The energy spectrum of the gamma ray from neutron captures on gadolinium [59].

## 6.2 Difference of tuning sources in the Monte Carlo simulation

Tuning of one of the water quality parameters,  $C_{\text{abs}}$  (Eq. (3.16)), was done in two ways for SK-VI. One is generating 50 MeV electrons to check the water transparency in MC. The other is using decay electrons simulation. In the above discussion, the tuning source is 50 MeV electrons. As described in Section 3.2.2, the time variation of the water transparency is evaluated using decay electrons of real data. Hence, using decay electron simulation is consistent with the data analysis. Due to the change of  $C_{\text{abs}}$ , the rest of the parameters,  $\beta$  (Section 3.2.3),  $C_{\text{sca}}$  (Section 3.3.3), and COREPMT (Section 3.4.1) also change and the values of these parameters for each tuning way is summarized in Table 6.4.

	50 MeV electrons	decay electrons
$C_{\text{abs}} p_0$	-1.187	-0.730231
$p_1$	27840	25257.2
$\beta p_0$	-0.006322	-0.005847
$p_1$	-0.00413	-0.005357
$C_{\text{scat}}$	0.4998	0.54774
COREPMT	0.8877	0.9008

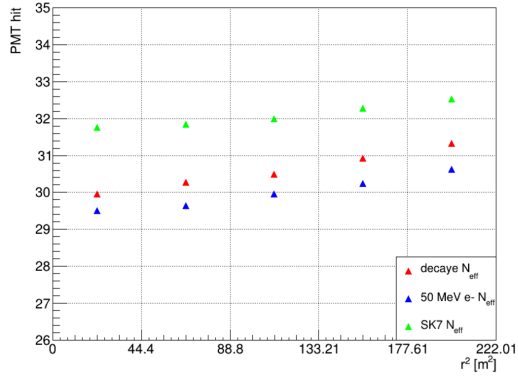
Table 6.4: The parameters determined by different methods.

The mean  $N_{\text{eff}}$  for each tuning source is shown in Figure 6.15. The mean  $N_{\text{eff}}$  using the decay electrons tuning source parameters is about 2.0 % larger than that using the 50 MeV electrons tuning source parameters. Then, the difference between the mean  $N_{\text{eff}}$  of SK-VI and SK-VII improves from 7.0 % to 4.9 % by changing the tuning source from 50 MeV electrons to decay electrons. Tuning  $C_{\text{abs}}$  with the same source as the data, decay electrons, results in the difference between  $N_{\text{eff}}$  of SK-VI and SK-VII getting small.

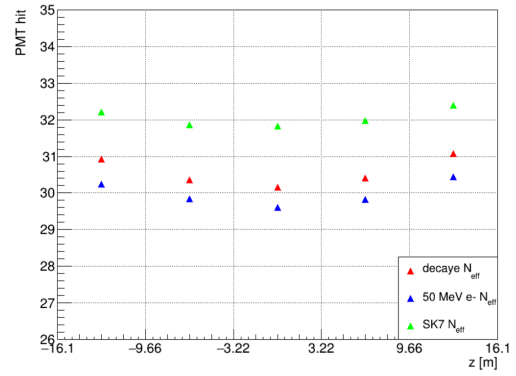
## 6.3 Evaluation of time dependence of the SK detector

The stability of the detectors through the SK-VI and SK-VII periods is monitored using the mean energy. For SK-VI, data from September 10, 2020, when SK-VI started, to June 1, 2022, before additional Gd-loading starts, are used. For SK-VII, data from July 5, 2022, when SK-VII started, to October 12, 2023, before SK-VIII started, are used. Those periods are divided into 30-day intervals. Also, the sample is divided into nine areas using the reconstructed vertex positions for each period as shown in Figure 6.16a. Then the fitting is performed to evaluate the mean energy in each area. Figure 6.16b shows the fitting of reconstructed energy distribution in each area.

The time dependence of the mean energy in each area and the overall area is checked and the stability of the detector through the SK-VI and SK-VII period is discussed in the following sections.

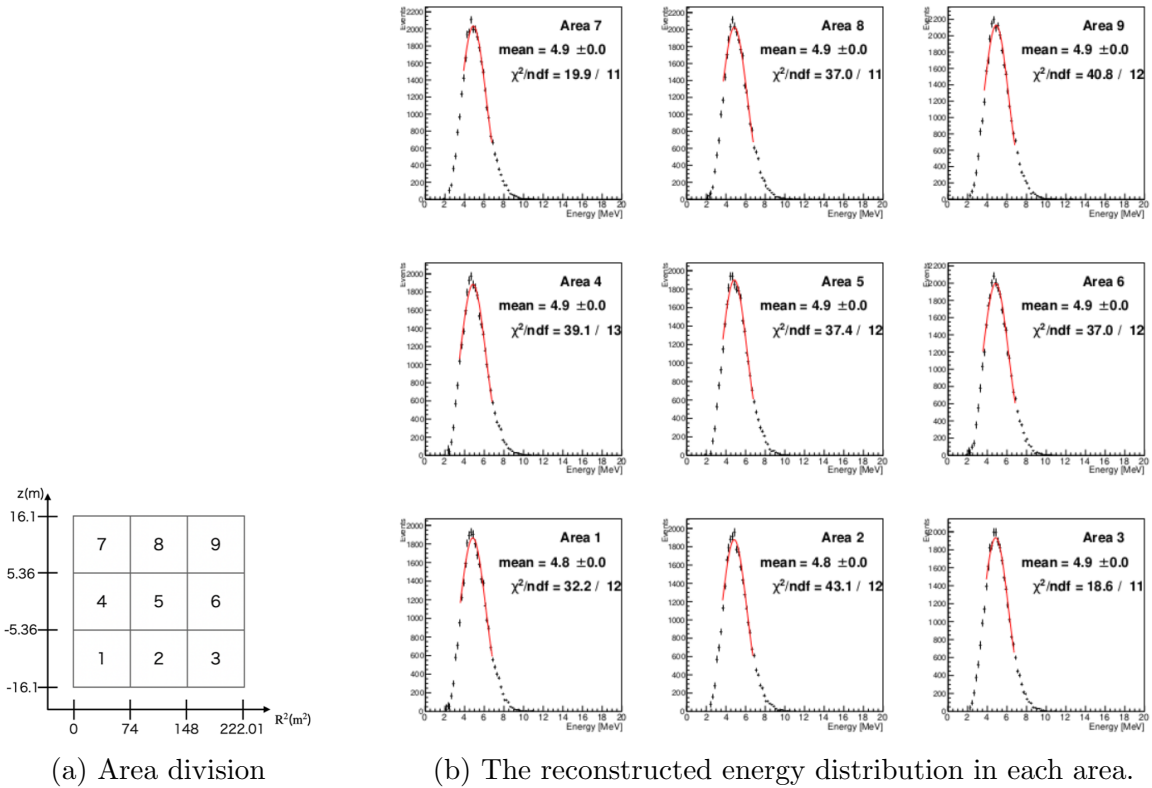


(a) The mean  $N_{\text{eff}}$  using the different tuning source parameters in the  $r^2$ -direction.



(b) The mean  $N_{\text{eff}}$  using the different tuning source parameters in the  $z$ -direction.

Figure 6.15: The mean  $N_{\text{eff}}$  using the different tuning source parameters. The red dots represent the mean  $N_{\text{eff}}$  using the decay electrons tuning parameters, and the blue dots represent that using the 50 MeV electrons tuning parameters. The green dots represent the mean  $N_{\text{eff}}$  of the SK-VII MC.



(a) Area division

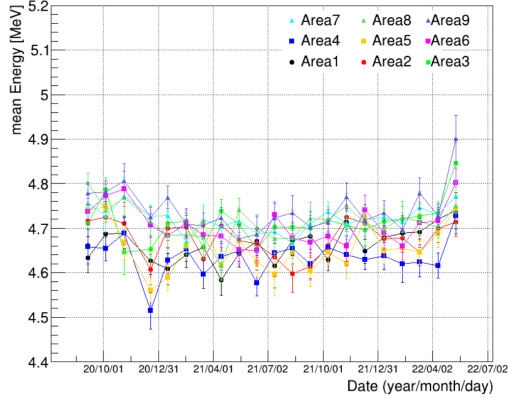
(b) The reconstructed energy distribution in each area.

Figure 6.16: (a) Area division. (b) The reconstructed energy distribution in each area.

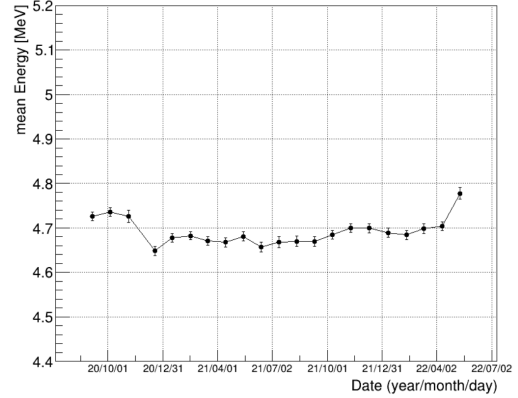
### 6.3.1 Time variation of energy in SK-VI and SK-VII periods

Figure 6.17 and Figure 6.18 show the mean energy and a  $\text{diff}_{\text{period}}$  for SK-VI data. Figure 6.19 and Figure 6.20 show those for SK-VII data. The  $\text{diff}_{\text{period}}$  is defined as follows.

$$\text{diff}_{\text{period}} = \frac{(\text{mean energy})_{\text{one period}} - (\text{mean energy})_{\text{all period}}^{\text{ave}}}{(\text{mean energy})_{\text{all period}}^{\text{ave}}} \quad (6.3)$$

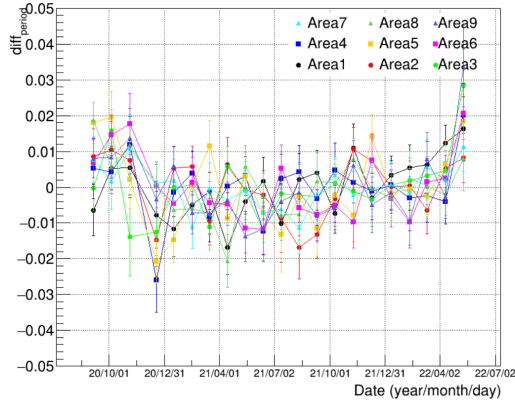


(a) The time distribution of the mean energy in each area.

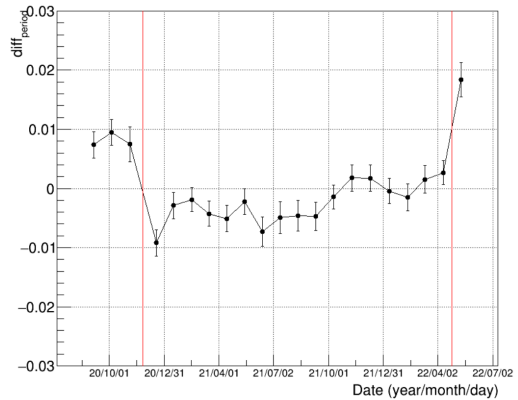


(b) The time distribution of the average mean energy in all areas.

Figure 6.17: The time distribution of the mean energy for SK-VI data.



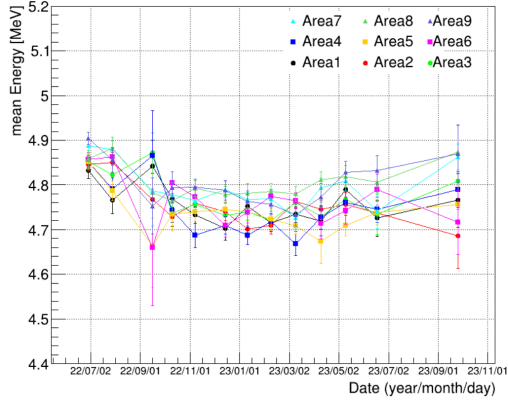
(a) The  $\text{diff}_{\text{period}}$  of the mean energy in each area.



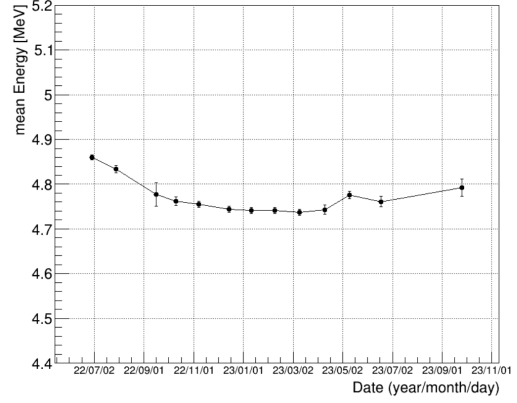
(b) The  $\text{diff}_{\text{period}}$  of the averaged mean energy.

Figure 6.18: The  $\text{diff}_{\text{period}}$  of the mean energy for SK-VI data.

We found that the first three points and the last point of the SK-VI result (the periods outside the two red lines in Figure 6.18b), and the first two points of the SK-VII result (the left periods of the red line in Figure 6.20b) are thought to be affected by Gd-loading. Therefore, these periods are not appropriate for solar neutrino analysis that requires better than 0.5 % energy scale uncertainty. The periods other than these periods are defined

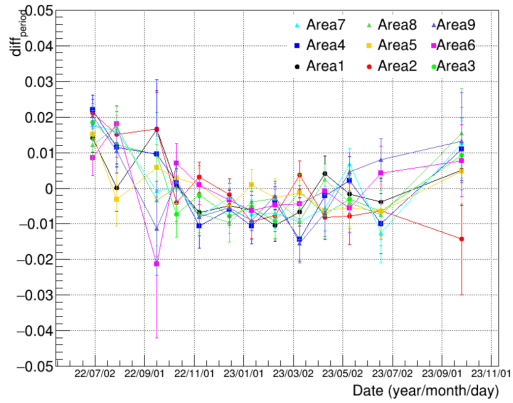


(a) The time distribution of the mean energy in each area.

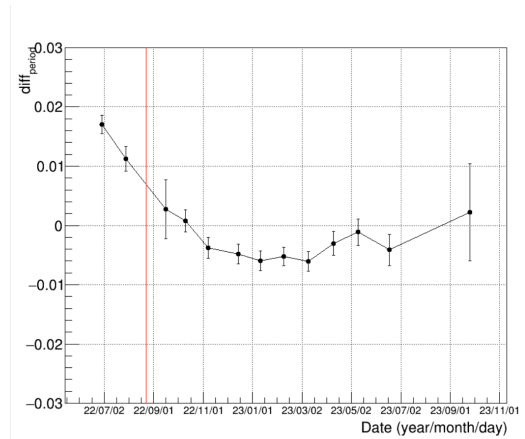


(b) The time distribution of the average mean energy in all areas.

Figure 6.19: The time distribution of the mean energy for SK-VII data.



(a) The  $\text{diff}_{\text{period}}$  of the mean energy in each area.



(b) The  $\text{diff}_{\text{period}}$  of the averaged mean energy.

Figure 6.20: The  $\text{diff}_{\text{period}}$  of the mean energy for SK-VII data.

as the stable phase. The standard deviation of  $\text{diff}_{\text{period}}$  in the stable phase is about 0.35 % and 0.38 % for SK-VI and SK-VII, respectively. This result is good enough compared with the goal of 0.5 % stability.

In the stable phases of SK-VI and SK-VII, the average mean energy for SK-VI is  $4.681 \pm 0.016$  MeV, and that for SK-VII is  $4.768 \pm 0.019$  MeV. The difference is about 1.9 %. This is the same trend of the result of the position dependence analysis (Section 6.1.1). To reduce this difference, further investigation is needed into the measurement of the water transparency in the two phases.

# Chapter 7

## Discussion

In this study, we developed a new energy scale calibration method using spallation neutron captures on gadolinium. This method enables more detailed verification of the position dependence and time stability of the energy scale in Super-Kamiokande. Consequently, once the absolute energy scale is determined using existing methods such as LINAC, our method allows for monitoring the time stability without requiring frequent LINAC measurements. This provides significant advantages, such as ensuring stability during periods when LINAC measurements are unavailable, including periods without LINAC operations or coil failure, and evaluating the energy scale stability during such periods.

Using this method, we evaluated the current position dependence and time stability of the energy scale of the SK detector in the SK-Gd phase, as discussed in the previous chapter. The position dependences in the  $r^2$ -direction are 0.88 % and 0.76 % for SK-VI and SK-VII, respectively. The position dependences in the  $z$ -direction are 0.21 % and 0.49 % for SK-VI and SK-VII. Since our goal is set to 0.5 % position dependence, the  $r^2$ -dependence should be improved. One of the causes of the large  $r^2$ -dependence is that the variation of the energy scale of the Monte Carlo simulation is about 1 % and this variation is larger than that of the data. In the MC, we also found that there might be an energy dependence of the position dependence. For the  $r^2$ -direction dependence of the energy scale, the variation of the energy scale is about 0.35 % for the 4 MeV electron MC, while it is about 0.15 % for the 7 MeV electron MC. Therefore, it might be that the lower the energy of events, the larger the variation. As a result,  $\text{Gd}(n, \gamma)$  events, where individual gamma rays have lower energies, may be more affected by this energy dependence. The energy dependence of the position dependence in the MC may arise from the modeling of Cherenkov light emission from electrons, which could depend on the energy of the electrons. Various factors could contribute to this effect, and it is necessary to investigate the behavior of the MC and identify the cause. Additionally, differences in the neutron captures on Gd analysis between SK-VI and SK-VII were identified in both MC and data. For the MC, the average energy scale for SK-VI is about 1.5 % smaller than that for SK-VII. Similarly, for the data, the average energy scale for SK-VI is about 1.9 % smaller than that for SK-VII. These differences might result from variations in the measurement methods for the water transparency in each phase. It will be necessary to unify the measurement methods and reanalyze the spallation neutron captures on Gd.

In summary, this study plays a significant role in the energy calibration of the SK

detector, and further detailed investigations are required to achieve more precise calibration.

# Chapter 8

## Conclusion

To improve the neutron capture efficiency, gadolinium was introduced to the Super-Kamiokande detector in 2020, and the Gd mass concentration was about 0.01 % in the SK-VI phase. The additional Gd loading was conducted in 2022, and the Gd mass concentration was about 0.03 % in the SK-VII phase. We are developing a new method to monitor the time stability and the position dependence of the detector's energy scale using spallation neutron captures on Gd. The goal of our study is to achieve 0.5 % systematic uncertainty, for precise solar neutrino measurement.

The advantages of calibration using spallation neutron captures on Gd are that they can be detected throughout the entire detector and these events occur at high rates, about 100,000 events per day. So the position dependence of the detector can be monitored in more detail. On the other hand, the energies of these events are low and close to the trigger threshold. Therefore, special treatment is needed for this analysis and the event selections for the spallation neutron captures on Gd were developed. Using this method, the position dependence of the reconstructed energy in SK-VI and SK-VII was evaluated by comparing the data and the MC simulation. Also, the time variation of the energy scale in SK-VI and SK-VII was evaluated.

The position dependence of the energy scale was monitored in the  $r^2$ -direction and the z-direction of the detector. We found that the  $r^2$ -dependence was about 0.88 % for SK-VI and about 0.76 % for SK-VII. The z-dependence was about 0.21 % for SK-VI and about 0.49 % for SK-VII. For the z-dependence, this result met the goal of 0.5 % uncertainty, while the  $r^2$ -dependence was larger than the goal. Also, the differences in the energy scale for SK-VI and SK-VII are about 1.5 % for the MC analysis and about 1.2 % for the data analysis. The causes are thought to be the tuning method of the water quality and the systematic errors unique to the spallation neutron captures on Gd analysis. To check these causes, the neutron captures on Gd MC simulation was compared with the electron MC simulation and there was about 0.5 % to 2 % difference between these two MC simulations. This difference is thought to be the systematic error unique to the neutron captures on Gd simulation. Also, in the electron MC, we found that the position dependence of the energy scale got worse as the energy of the generated electron got small in the region below 7 MeV. Therefore, one of the causes of the position dependence of the neutron MC's energy scale can be explained by this effect. It is necessary to reveal the cause of this energy dependence of the energy scale's position dependence.

For the time stability of the energy scale in SK-VI and SK-VII, other than the Gd-

loading period, we found the stability was within  $\pm 0.4\%$  for both SK-VI and SK-VII (0.35% for SK-VI and 0.38% for SK-VII). This result was good enough compared with the goal of 0.5% stability. On the other hand, the energy scales for SK-VI and SK-VII were different by about 1.9%. To reduce this difference, it needs to understand the time variation of the water transparency more precisely and to investigate whether there are other causes.

These results revealed the current accuracy of the energy scale reconstruction in the Gd-loaded Super-Kamokande and provided some hints on improving the systematic uncertainty of the detector.

# Acknowledgment

I would like to express my heartfelt gratitude to everyone who has supported me throughout this study.

First and foremost, I am deeply thankful to my supervisor, Prof. Y. Nakajima, for providing me with the opportunity to undertake this study and for his continuous and meticulous guidance. I am also profoundly grateful for his valuable advice on the direction of my study.

I extend my sincere thanks to Harada-san of the Kamioka Observatory for dedicating his valuable time to teach me the fundamentals of analysis at Super-Kamiokande with great detail and patience, despite his busy schedule. His thorough responses whenever I had questions were invaluable, and I truly appreciate his support.

I am also deeply grateful to Asst. Prof. Y. Nakano of Toyama University, Fujita-san of IPMU, Tada-san of Okayama University, and Shimamura-san of Yokohama National University for their insightful advice on my analysis and for addressing my questions during regular meetings and email correspondences.

Additionally, I would like to thank Prof. H. Sekiya, Asst. Prof. T. Yano of the Kamioka Observatory, Asst. Prof. Y. Hino of the neutrino group, and Asaka-kun of Tokyo University of Science for their valuable discussions during the NTag meetings, particularly regarding the differences in analysis with Am/Be sources.

Furthermore, I am immensely thankful to Prof. M. Yokoyama, Asst. Prof. K. Nakagiri, and Daniel of the Yokoyama-Nakajima Laboratory for their constructive feedback during laboratory meetings and conference presentations. Their insights were crucial to the development of my study.

I would also like to extend my gratitude to my laboratory members—Yoshimi, Kodama-san, Okinaga-san, Kobayashi-san, Arai-kun, Goto-kun, Mizuno-kun, Hayasaki-kun, and Masaki-kun—for their camaraderie, inviting me to meals, and creating a friendly atmosphere.

Finally, I am deeply grateful to everyone who has supported me throughout my study life. I would like to take this opportunity to express my profound appreciation to all who have helped my study thus far.

# Appendix A

## Ratio of the neutron captures on Hydrogen

In the neutron capture event analysis, neutrons are also captured by hydrogen nuclei as well as gadolinium. The ratio of the neutron captures on hydrogen and gadolinium was checked in the Monte Carlo simulation. The conditions for generating MC and event selections are the same as in Chapter 5. The time information is the same as in Section 6.1. Figure A.1 and Figure A.2 show the  $N_{\text{eff}}$  distributions for the SK-VI and SK-VII MC, respectively. The black lines represent the signals from neutron captures on hydrogen and the red lines represent those from neutron captures on gadolinium. The ratio of each signal is summarized in Table A.1.

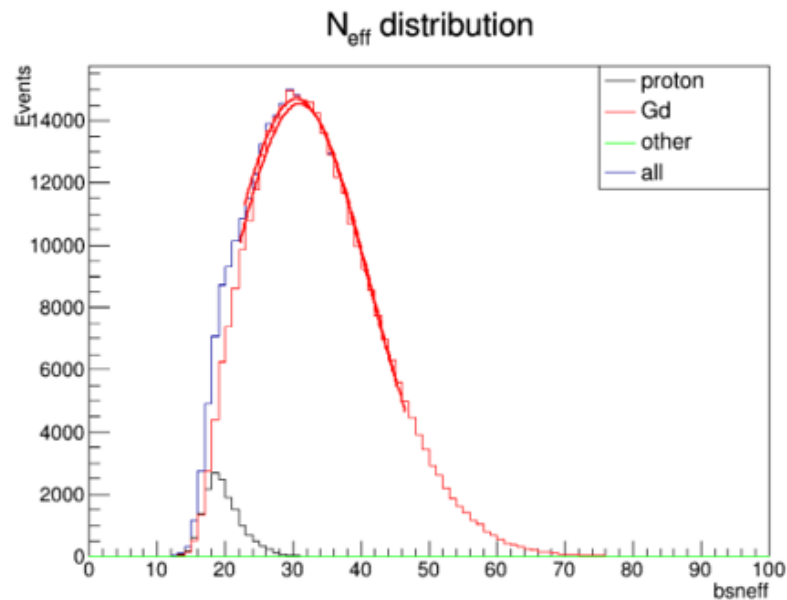


Figure A.1: The  $N_{\text{eff}}$  distribution for the SK-VI MC. The black line represents the signals from neutron captures on hydrogen. The red line represents those from neutron captures on gadolinium. The green line represents other signals. The blue line represents the sum of all signals.

From Table A.1, above 95 % of signals are from neutron captures on Gd for both SK-VI and SK-VII MC. The ratio of neutron captures on hydrogen for the SK-VII MC is smaller

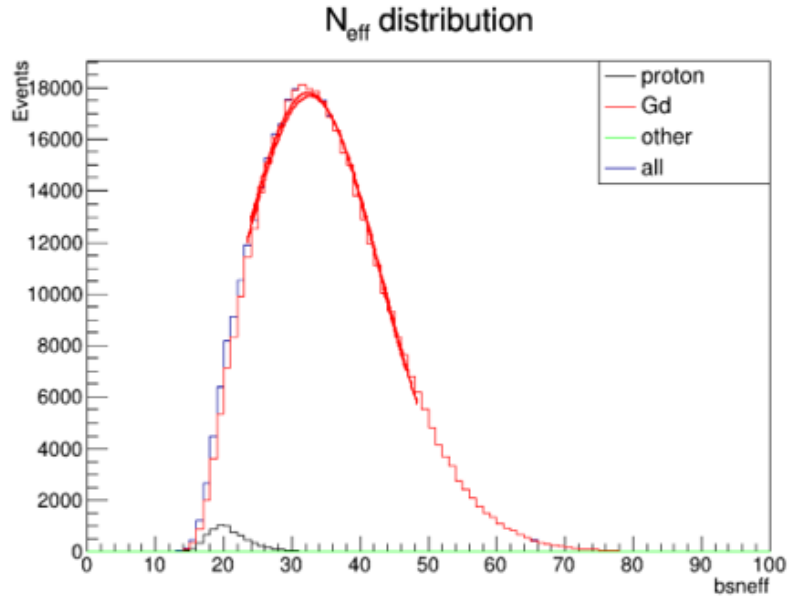


Figure A.2: The  $N_{\text{eff}}$  distribution for the SK-VII MC. The black line represents the signals from neutron captures on hydrogen. The red line represents those from neutron captures on gadolinium. The green line represents other signals. The blue line represents the sum of all signals.

	gadolinium	hydrogen	all
SK-VI	343545 (95.50 %)	16110 (4.49 %)	359745
SK-VII	431612 (98.40 %)	6945 (1.58 %)	438644

Table A.1: The ratio of each signal. Gadolinium means the signals from neutron captures on gadolinium, hydrogen means those from neutron captures on hydrogen, and all means all signals.

than for the SK-VI MC. This is due to the difference in the Gd concentration. Also the mean  $N_{\text{eff}}$  for all signals and signals only from neutron captures on Gd are summarized in Table A.2.

	gadolinium	all
SK-VI	$30.95 \pm 0.04$	$30.46 \pm 0.05$
SK-VII	$32.63 \pm 0.03$	$32.39 \pm 0.04$

Table A.2: The mean  $N_{\text{eff}}$  for all signals (all) and signals only from neutron captures on Gd (gadolinium).

From this table, about 1.6 % is affected by neutron captures on hydrogen for the SK-VI MC, and about 0.7 % is affected for the SK-VII MC. However, these differences are much smaller than the difference of the mean  $N_{\text{eff}}$  between SK-VI and SK-VII (about 6.3 %), so the difference between SK-VI and SK-VII is not due to the effect of neutron captures on hydrogen.

# Bibliography

- [1] W. Pauli. Letter to l. meitner and her colleagues dated 4 december 1930 (letter open to the participants of the conference in t" ubingen), recorded in w. pauli. Phys. Today 31N9, Vol. 27, 1978
- [2] C. L. Cowan *et al.* " Detection of the free neutrino: A Confirmation, " Science 124 (1956), pp. 103–104.
- [3] G. Danby, J. M. Gaillard, K. Goulianos, L. M Lederman, N. Mistry, M. Schwartz, and J. Steinberger. "Observation of high-energy neutrino reactions and the existence of two kinds of neutrinos," Physical Review Letters, Vol. 9, No. 1, p. 36, 1962.
- [4] K. Kodama, *et al.* "Observation of tau neutrino interactions," Physics Letters B, Vol. 504, No. 3, pp. 218–224, 2001.
- [5] M. Goldhaber, L. Grodzins, and A. W. Sunyar. "Helicity of neutrinos," Physical review, Vol. 109, No. 3, p. 1015, 1958.
- [6] Raymond Davis. " A review of the Homestake solar neutrino experiment, " Progress in Particle and Nuclear Physics 32 (1994), pp. 13–32. issn: 0146-6410.
- [7] K. S. Hirata *et al.* " Observation of B-8 Solar Neutrinos in the Kamiokande-II Detector, " Phys. Rev. Lett. 63 (1989), p. 16.
- [8] M. G. Aartsen *et al.* " Multi-messenger observations of a flaring blazar coincident with high-energy neutrino IceCube-170922A, " Science 361, eaat1378 (2018).
- [9] Z. Maki, M. Nakagawa, and S. Sakata. "Remarks on the unified model of elementary particles," Progress of Theoretical Physics, Vol. 28, No. 5, pp. 870–880, 1962.
- [10] R. Davis, D. S. Harmer, and K. C. Hoffman. "Search for neutrinos from the sun," Phys. Rev. Lett., Vol. 20, pp. 1205–1209, May 1968.
- [11] K. S. Hirata, *et al.* "Observation of 8B solar neutrinos in the kamiokande-ii detector," Phys. Rev. Lett., Vol. 63, pp. 16–19, Jul 1989.
- [12] K. S. Hirata, *et al.* "Experimental Study of the Atmospheric Neutrino Flux," Phys. Lett. B, Vol. 205, p. 416, 1988.
- [13] R. Becker Szendy, *et al.* "Electron- and muon-neutrino content of the atmospheric flux," Phys. Rev. D, Vol. 46, pp. 3720–3724, Nov 1992.

- [14] Y. Fukuda, *et al.* "Evidence for oscillation of atmospheric neutrinos," *Physical review letters*, Vol. 81, No. 8, p. 1562, 1998.
- [15] S. Fukuda, *et al.* "Solar  $^8\text{B}$  and hep neutrino measurements from 1258 days of Super-Kamiokande data," *Physical Review Letters*, Vol. 86, No. 25, p. 5651, 2001.
- [16] Q. Ahmad, *et al.* "Direct evidence for neutrino flavor transformation from neutral-current interactions in the sudbury neutrino observatory," *Physical review letters*, Vol. 89, No. 1, p. 011301, 2002.
- [17] S. Navas *et al.* (Particle Data Group), "Review of Particle Physics," *Phys. Rev. D* 110, 030001 (2024).
- [18] D. Gabriel *et al.* "The future of solar neutrino," *Annu. Rev. Nucl. Part. Sci* 2021. 71: 1-39.
- [19] J. N. Abdurashitov *et al.* "Results from sage (the russian-american gallium solar neutrino experiment)," *Phys. Rev. Lett B.* 328, (1994)234-248.
- [20] F. Kaether *et al.* "Reanalysis of the gallex solar neutrino flux and source experiments," *Phys. Rev. Lett B.* 685 (2010) 47-54.
- [21] G. Bellini *et al.* "First evidence of pep solar neutrinos by direct detection in Borexino," *Physical Review Letters* 108, 051302 (2012).
- [22] K. Lande *et al.* "Results from the Homestake solar neutrino observatory," *Conf. Proc. C* 900802 (1990) 867-675, *Conf. Proc. C* 900802V1 C900802V1:667-675.
- [23] C. Arpesella *et al.* "First real time detection of  $\text{Be}^7$  solar neutrinos by Borexino," *Phys. Lett. B* 658: 101-108, (2008).
- [24] A. Gando *et al.* " $^7\text{Be}$  solar neutrino measurement with KamLAND," *Phys. Rev. C* 92, 055808 (2015).
- [25] K. Abe *et al.* "Solar neutrino measurements in Super-Kamiokande-IV," *Phys. Rev. D* 94, 052010(2016).
- [26] K. Hirata *et al.* "Observation of a neutrino burst from the supernova SN1987A," *Phys. Rev. Lett.* 58, 1490(1987).
- [27] B. Aharmim *et al.* "Combined analysis of all three phases of solar neutrino data from the sudbury neutrino observatory," *Phys. Rev. C* 88 025501 (2013)
- [28] S. Abe *et al.* "Measurement of the  $^8\text{B}$  solar neutrino flux with the KamLAND liquid scintillator detector," *Phys. Rev. C* 84, 035804 (2011).
- [29] B. Aharmim *et al.* "Search for hep solar neutrinos and the diffuse supernova neutrino background using all three phases of the sudbury neutrino observatory," *Phys. Rev. D* 102, 062006(2020).

- [30] Q. R. Ahmad *et al.* (SNO Collaboration), "Direct Evidence for Neutrino Flavor Transformation from Neutral-Current Interactions in the Sudbury Neutrino Observatory," *Physical Review Letters* 89, 011301 (2002)
- [31] P. Langacker *et al.* "Implications of the Mikheev-Smirnov-Wolfenstein (MSW) Mechanism of Amplification of Neutrino Oscillations in Matter," In: *Nucl. Phys. B* 282 (1987), pp. 589–609.
- [32] J. Farine. "Measurement of the rate of  $\nu_e + d \rightarrow p + p + e^-$  interactions produced by 8B solar neutrinos at the Sudbury Neutrino Observatory," *Phys. Atom. Nucl.* 65 (2002). Ed. by V. A. Bednyakov and V. B. Brudanin, pp. 2147–2155.
- [33] K. Abe *et al.* "Solar neutrino measurements using the full data period of Super-Kamiokande-IV," *Phys. Rev. D* 109, 092001 (2024).
- [34] Ken'ichiro Nakazato *et al.* "Supernova Neutrino Light Curves and Spectra for Various Progenitor Stars: From Core Collapse to Proto-neutron Star Cooling," *Astrophys. J. Suppl.* 205 (2013), p. 2.
- [35] K. Abe *et al.* "Diffuse supernova neutrino background search at Super-Kamiokande," *Phys. Rev. D* 104.12 (2021), p. 122002.
- [36] Y. Fukuda, *et al.* "The Super-Kamiokande detector," *Nucl. Instrum. Meth. A*, Vol. 501, pp. 418–462, 2003.
- [37] Y. Suzuki. "The Super-Kamiokande experiment," *The European Physical Journal C*, Vol. 79, pp. 1–18, 2019.
- [38] Z. Conner. "A study of solar neutrinos using the Super-Kamiokande detector," PhD thesis, University of Maryland, 1997.
- [39] K. Abe *et al.*, "Calibration of the Super-Kamiokande Detector," *Nucl. Instrum. Meth. A* 737 (2014) 253-272.
- [40] T. Yamaguchi. "Observation of 8B Solar Neutrinos from 300-day data at Super-Kamiokande," PhD thesis, University of Osaka, 1998.
- [41] Y. Nakano, T. Hokama, M. Matsubara, M. Miwa, M. Nakahata, T. Nakamura, H. Sekiya, Y. Takeuchi, S. Tasaka, and R. A. Wendell. "Measurement of the radon concentration in purified water in the Super-Kamiokande IV detector," *Nucl. Instrum. Meth. A*, Vol. 977, p. 164297, 2020.
- [42] H. Nishino, K. Awai, Y. Hayato, S. Nakayama, K. Okumura, M. Shiozawa, A. Takeda, K. Ishikawa, A. Minegishi, and Y. Arai. "High-speed charge-to-time converter ASIC for the Super-Kamiokande detector," *Nucl. Instrum. Meth. A*, Vol. 610, pp. 710–717, 2009.
- [43] S. Yamada, *et al.* "Commissioning of the new electronics and online system for the Super-Kamiokande experiment," *IEEE Trans. Nucl. Sci.* Vol. 57, pp. 428–432, 2010.

- [44] R. Brun and F. Rademakers, “Root— an object oriented data analysis framework,” Nucl. Instrum. Meth. A, 389(1997), 81-86.
- [45] K. Abe, *et al.* ” First gadolinium loading to Super-Kamiokande,” Nucl. Instrum. Meth. A, Vol. 1027, p. 166248, 2022.
- [46] S. Sakai, スーパーカミオカンデにおける検出器校正の研究, 2020.
- [47] K. Hamaguchi, ”Nickel analysis for QE(CE) table in coil off period,” Super-Kamiokande Collaboration Meeting (2024)
- [48] Shizuka Shima, ”Study of Super-Kamiokande detector calibration using cosmogenic neutron capture on Gadolinium,” Department of Physics, Graduate School of Science The University of Tokyo, Master Thesis, 2023.
- [49] M. Nakahata, *et al.* ”Calibration of Super-Kamiokande using an electron linac. Nucl,” Instrum. Meth. A, Vol. 421, pp. 113–129, 1999.
- [50] E. Blaufuss, *et al.* ”N-16 as a calibration source for Super-Kamiokande,” Nucl. Instrum. Meth. A, Vol. 458, pp. 638–649, 2001.
- [51] 兼村 侑希, スーパーカミオカンデガドリニウム実験のためのエネルギースケール評価と Rn 濃度解析, 2021.
- [52] Y.Nakano. “Data quality in SK7,” Super-Kamiokande Collaboration Meeting (2022)
- [53] S. W. Li and J. Beacom, ”First calculation of cosmic-ray muon spallation backgrounds for MeV astrophysical neutrino signals in Super-Kamiokande,” Physical Review C 89, 045801 (2014).
- [54] Y. Zhang *et al.* ”First measurement of radioactive isotope production through cosmic-ray muon spallation in Super-Kamiokande IV,” Physical Review D, 93, 012004 (2016).
- [55] K. Abe *et al.* ”Second gadolinium loading to Super-Kamiokande,” Nuclear Inst. and Methods in Physics Research, A 1065 (2024) 169480.
- [56] 前川 雄音, 光電子増倍管ノイズ低減によるスーパーカミオカンデの中性子識別向上, 2021.
- [57] 篠木 正隆, スーパーカミオカンデ-ガドリニウム実験による宇宙線ミューオン核破碎反応に由来する中性子生成率の測定, 東京理科大学大学院 理工学研究科物理学専攻, 修士論文, 2021.
- [58] Masayuki Harada, Yusuke Koshio, and Kaito Hagiwara. “Development of Geant4 based simulation for Super-Kamiokande,” PoS KMI2019 (2019).
- [59] Tomoyuki Tanaka *et al.* ”Gamma-ray spectra from thermal neutron capture on gadolinium-155 and natural gadolinium,” Progress of Theoretical and Experimental Physics, Volume 2020, Issue 4, April 2020, 04D02.